TU Delft

Delft University of Technology

Manipulation of supercurrent by the magnetic field

Irfan, Muhammad

DOI
10.4233/uuid:345937cb-fd16-46b3-9c01-c098e06f0743

Publication date
2020

Document Version
Final published version

Citation (APA)
Irfan, M. (2020). *Manipulation of supercurrent by the magnetic field*. [Dissertation (TU Delft), Delft University of Technology]. https://doi.org/10.4233/uuid:345937cb-fd16-46b3-9c01-c098e06f0743

Important note
To cite this publication, please use the final published version (if applicable).
Please check the document version above.

Copyright
Other than for strictly personal use, it is not permitted to download, forward or distribute the text or part of it, without the consent of the author(s) and/or copyright holder(s), unless the work is under an open content license such as Creative Commons.

Takedown policy
Please contact us and provide details if you believe this document breaches copyrights.
We will remove access to the work immediately and investigate your claim.

This work is downloaded from Delft University of Technology.
For technical reasons the number of authors shown on this cover page is limited to a maximum of 10.

MANIPULATION OF SUPERCURRENT BY THE MAGNETIC FIELD

MANIPULATION OF SUPERCURRENT BY THE MAGNETIC FIELD

Proefschrift

ter verkrijging van de graad van doctor
aan de Technische Universiteit Delft,
op gezag van de Rector Magnificus prof. dr. ir. T.H.J.J. van der Hagen,
voorzitter van het College voor Promoties,
in het openbaar te verdedigen op woensdag 8 januari 2020 om 15:00 uur

door

Muhammad IRFAN

Master of Philosophy in Physics,
Pakistan Institute of Engineering and Applied Sciences, Islamabad, Pakistan,
geboren te Rawalpindi, Pakistan.

Dit proefschrift is goedgekeurd door de

promotor: Dr. A. R. Akhmerov
copromotor: Dr. M. T. Wimmer

Samenstelling promotiecommissie:

Rector Magnificus,	voorzitter
Dr. A. R. Akhmerov	Technische Universiteit Delft, promotor
Dr. M. T. Wimmer	Technische Universiteit Delft, copromotor

Onafhankelijke leden:

Prof. dr. ir. B. J. van Wees	De Rijksuniversiteit Groningen
Prof. dr. G. A. Steele	Technische Universiteit Delft
Prof. dr. I. V. Gornyi	Karlsruher Institut für Technologie, Germany
Prof. dr. Y. M. Blanter	Technische Universiteit Delft
Prof. dr. X. Waintal	Université Grenoble Alpes, CEA INAC PHELIQS, France

This research was supported by the Netherlands Organisation for Scientific Research (NWO/OCW), as part of the Frontiers of Nanoscience program.

Printed by: Gildeprint

Front & Back: Supercurrent density

Copyright © 2020 by M. Irfan

Casimir PhD Series, Delft-Leiden 2020-02

ISBN 978-90-8593-429-5

An electronic version of this dissertation is available at
http://repository.tudelft.nl/.

To my Parents.

CONTENTS

SUMMARY

Superconductor–semiconductor hybrid devices are interesting not only for their known and potential applications but also for the associated novel physical processes. One such example is the proposal for the realization of Majorana zero-modes, which are robust against noise and have applications in quantum information processing. Although the Josephson effect is known for decades, the recent advances in the experimental technologies made it possible only recently to make highly tunable hybrid devices.

In this thesis, we study the superconductor–normal-metal–superconductor Josephson junctions and propose new effects or analyze experimental findings. In a Josephson junction, it is difficult to determine whether the flow of supercurrent is ballistic or diffusive. We propose an hourglass-shaped Josephson junction geometry to probe the nature of transport. In this device, the measurement of a critical current as a function of an external magnetic field produces a clear signature of the ballistic supercurrent.

In metal-based Josephson junctions, the supercurrent flows uniformly through the scattering region. In contrast, semiconductor-based Josephson junctions allow tunable supercurrent due to the tunable carrier density of the semiconductors. We model a bilayer graphene Josephson junction with a split-top and back gate in the presence of an applied magnetic field to analyze the experimental measurements. The opening of bandgap in bilayer graphene in the gated area by applying tunable electrostatic potential allows spatial manipulation of supercurrent. The magnetic field is then used to probe the supercurrent flow in the device.

In general, an applied magnetic field strongly suppresses supercurrent in Josephson junctions because it randomizes the contribution of the individual states. However, we show that graphene Josephson junctions are special and avoid the suppression of critical current under an applied in-plane magnetic field. The critical current as a function of the Zeeman field has a plateau whose size depends on the junction detail.

Finally, we study a Josephson junction coupled with a microwave transmission line resonator in collaboration with an experimental group. We model this system to analyze and explain an unexpected experimental result of the system. We show that the unexpected outcome of the experiment is due to the coupling of the higher modes of the transmission line resonator.

SAMENVATTING

Hybride supergeleider–halfgeleider apparaten zijn interessant, niet alleen vanwege hun bekende en potentiële toepassingen, maar door de bijkomende nieuwe fysische processen. Een voorbeeld hiervan is het voorstel van de realisatie van Majorana zero-modes, die robuust zijn tegen ruis en kwantuminformatie kunnen verwerken. Alhoewel het Josephson-effect al decennia bekend is, hebben recentelijke ontwikkelingen in experimentele technologieën het mogelijk gemaakt om hybride apparaten te maken die zeer precies afstelbaar zijn.

In dit proefschrift bestuderen we de supergeleider–normaal-metaal–supergeleider Josephson-juncties, beschrijven we nieuwe effecten en analyseren experimentele bevindingen. In een Josephson-junctie is het moeilijk om te bepalen of de superstroom ballistisch of diffuus is. We stellen een zandlopervormige Josephson-junctie geometrie voor om de oorsprong van dit transport te onderzoeken. In dit apparaat produceert de meting van een kritische stroom als functie van een extern magnetisch veld, een duidelijke ballistische superstroom.

In Josephson-juncties stroomt de superstroom gelijkmatig door het verstrooiingsgebied. Josephson-juncties op basis van halfgeleiders laten daarentegen een instelbare superstroom toe vanwege de instelbare dragerdichtheid van de halfgeleiders. We modelleren een dubbellaagse grafeen Josephson-junctie met een gesplitte top gate en gate aan de onderzijde in de aanwezigheid van een toegepast magnetisch veld om de experimentele metingen te analyseren. Het instellen van een elektrostatisch potentiaal opent een energie gat in het dubbellaags grafeen in het gebied met een gate, dit maakt vervolgens een ruimtelijke manipulatie van de superstroom mogelijk. Het magnetische veld wordt vervolgens gebruikt om de verdeling van de superstroom in het apparaat te meten.

In het algemeen onderdrukt een aangelegd magnetisch veld de superstroom in Josephson-juncties sterk omdat het de bijdrage van de afzonderlijke toestanden willekeurig maakt. We laten echter zien, dat grafeen Josephson-juncties speciaal zijn en de onderdrukking van een kritische stroom onder een aangelegd magnetisch veld in het vlak vermijden. De kritische stroom als functie van het Zeeman-veld, heeft een plateau waarvan de grootte afhangt van junctie details.

Ten slotte bestuderen we een Josephson-junctie gekoppeld aan een microgolf transmissielijnresonator in samenwerking met een experimentele groep. We modelleren dit systeem om een onverwacht experimenteel resultaat van het systeem te analyseren en te verklaren. We laten zien dat de onverwachte uitkomst van het experiment komt door de koppeling van de hogere modi van de transmissielijnresonator.

1

INTRODUCTION

1.1. PREFACE

What happens if we combine a semiconductor with a superconductor to make a hybrid device? Due to the proximity effect, the hybrid device gets some properties from both materials, which leads to the emergence of new physical processes. Beside interesting physics, these devices also lead to new applications ranging from magnetic field sensing to recent proposals to realize Majorana zero modes, which are robust against noise and have potentially promising uses in quantum information processing.

In semiconductors, the ability to control the charge carrier density by using electrostatic gate potential allows the fine-tuning of quantum transport properties. On the other hand, in superconductors, the formation of Cooper pairs (paired electrons) leads to a ground state condensation and dissipationless supercurrent. In a hybrid device, the superconductivity leaks into the semiconductor at mesoscopic distances, resulting in the flow of supercurrent in the semiconductor. As a result, the tunable charge carrier density allows manipulation of the supercurrent in the device. By breaking time-reversal symmetry using an applied magnetic field, it is possible to manipulate the supercurrent further. Sandwiching a normal-metal or thin insulator between two superconductors results in a Josephson junction where supercurrent flows between two superconductors depending upon the relative value of the superconducting phase of each condensate. This phenomenon is called the Josephson effect.

In this thesis, we study the Josephson effect in different Josephson junctions made of two-dimensional electron gas or graphene in the presence of a magnetic field. First, we propose a Josephson junction device design to distinguish ballistic transport from diffusive transport. We then study the spatial manipulation of supercurrent in a bilayer-graphene Josephson junction in collaboration with an experimental group. Next, we study a graphene Josephson junction in the presence of an in-plane magnetic field. We show that the junction remains insensitive to a range of magnetic fields, which allows probing the effect of finite temperature or induced spin-orbit coupling in graphene. In the last part, we simulated and analyzed some unexpected experimental measurements in a Josephson junction coupled to a microwave resonator.

1

1.2. JOSEPHSON EFFECT

In 1962, Brian Josephson proposed that when a thin insulating material separates two superconducting metals, the paired electrons can tunnel from one metal to the other [1]. This Cooper pair tunneling leads to a dissipationless supercurrent flowing between the two superconducting electrodes [2]. He calculated the supercurrent through the tunneling barrier perturbatively using a tunneling term in the Hamiltonian. He showed that a varying superconducting phase difference χ gives a sinusoidal variation of supercurrent:

$$I = I_o \sin(\chi), \tag{1.1}$$

and an applied voltage between the superconducting electrodes makes χ time dependent:

$$V = \frac{\hbar}{e}\frac{d\chi}{dt}, \tag{1.2}$$

with $\hbar$ the reduced Planck's constant and e the charge of an electron.

The supercurrent persists even if a metallic or semiconducting weak link replaces the thin insulating barrier [3]. However, the current-phase relation in these superconducting–normal-metal–superconducting (SNS) Josephson junctions is, in general, more complicated than the sinusoidal form (1.1). To understand the subgap transport in SNS Josephson junction, Andreev proposed a Cooper pair transfer process based on a coherent superposition of electron and hole states [4]. An electron with energy below the superconducting gap moving in the normal scattering region reflects from the superconducting–normal-metal interface as a hole and contribute two electrons in that superconductor as a Cooper pair as depicted in Fig. 1.1. This reflected hole then travels back to the opposite interface and reflects as an electron thereby annihilating a Cooper pair in that superconductor, and the process continues. This coherent transfer of electron-hole process results in the formation of Andreev bound states in the scattering region between the superconductors. These bound states with energy E_A contribute to the subgap supercurrent [5]:

$$I = \frac{2e}{\hbar}\sum_A \frac{dE_A}{d\chi} f_0(E_A), \tag{1.3}$$

with f_0 the Fermi distribution function.

The semiconductor-based Josephson junctions are interesting because of the controllable density of states and easy electrostatic confinement of electrons. These properties allow studying interesting single Andreev level quantum effects, which are not possible in metal-based Josephson junctions due to their continuous density of states except in superconducting point contacts [6–10]. However, the experimental realization of clean semiconductor–superconductor Josephson devices remained a challenge for quite long [11, 12]. With the technological advancements, the fabrication of highly transparent interfaces between semiconducting quantum well and superconducting electrodes became possible, which led to the realization of tunable supercurrent in semiconductor nanowires [13]. The study of supercurrent in a quantum dot made in a semiconductor nanowire by using local electrostatic gating is another such example [14]. The pioneering work of producing graphene made it possible to realize the Josephson effect at relativistic energies in graphene-based devices [15–17].

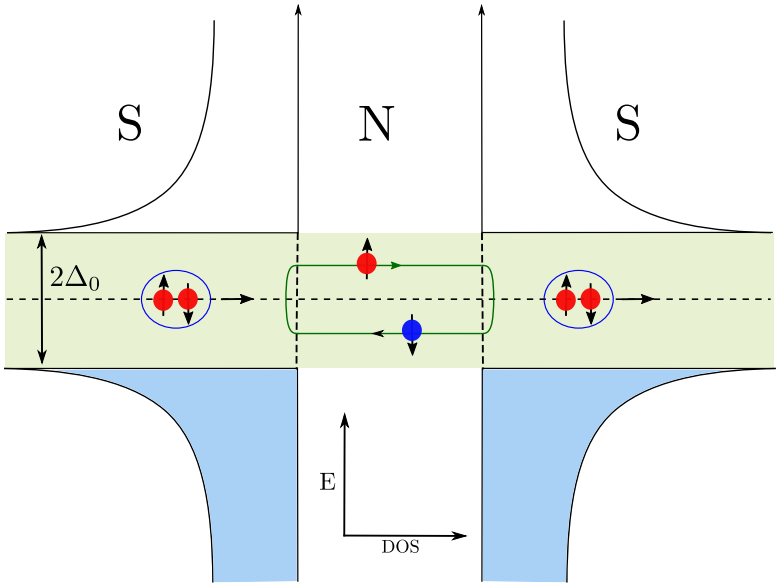

Figure 1.1: Illustration of Andreev bound state formation in an SNS Josephson junction.

1.2.1. BOGOLIUBOV-DE GENNES FORMALISM

In this section, we illustrate how to calculate the Andreev spectrum and supercurrent in a simple one-dimensional SNS Josephson junction by using Bogoliubov-de Gennes equation [3]. Consider a Josephson junction of normal metal length L and superconducting order parameters Δ. For simplification purpose, we assume a step-like potential which is zero in the normal region and have a magnitude Δ_0 in the superconducting electrodes:

$$\Delta = \begin{cases} \Delta_0 e^{i\chi_L} & x < 0, \\ \Delta_0 e^{i\chi_R} & x > L, \\ 0 & 0 \le x \le L, \end{cases} \tag{1.4}$$

with χ_L (χ_R) the superconducting phase in left (right) lead. The Bogoliubov-de Gennes (BdG) Hamiltonian in electron-hole basis is given by:

$$H_{BdG} = \begin{pmatrix} H(x) & \Delta(x) \\ \Delta^*(x) & -H(x) \end{pmatrix}, \tag{1.5}$$

where $H(x)$ is the single-particle Hamiltonian:

$$H = -\frac{\hbar^2}{2m^*}\partial_x^2 - \mu, \tag{1.6}$$

with μ the chemical potential and m^* the reduced electron mass. To get the Andreev spectrum, we solve the following Bogoliubov-de Gennes equation:

$$\begin{pmatrix} H(x) & \Delta(x) \\ \Delta^*(x) & -H(x) \end{pmatrix} \begin{pmatrix} u \\ v \end{pmatrix} = E \begin{pmatrix} u \\ v \end{pmatrix}, \tag{1.7}$$

with (u, v) the electron-like and hole-like quasiparticle wave functions and E the corresponding energy of the quasiparticles. The off-diagonal superconducting pairing potential term couples the electron-like and hole-like solutions. In a homogeneous superconductor considered here, the wave functions (u, v) have plane wave solutions [3]:

$$\begin{pmatrix} u \\ v \end{pmatrix} = e^{ikx} \begin{pmatrix} u_0 \\ v_0 \end{pmatrix}, \tag{1.8}$$

with

$$u_0^2 = \frac{E + \sqrt{E^2 - \Delta_0^2}}{2E}, \tag{1.9}$$

$$v_0^2 = \frac{E - \sqrt{E^2 - \Delta_0^2}}{2E}, \tag{1.10}$$

and

$$E^2 = \left(\hbar^2 k^2 / 2m^* - \mu\right)^2 + \Delta_0^2. \tag{1.11}$$

We first discuss the Andreev reflection at a normal-metal–superconductor (NS) boundary such that the pairing potential is zero in the normal metal ($x < 0$) and has value Δ_0 in the superconducting region ($x > 0$). An incident electron in the normal metal undergoes either an Andreev reflection or a normal reflection and reflects as a hole or electron, respectively, as shown in Fig. 1.2. The incident and reflected wave functions in the particle-hole basis are given by [5, 18, 19]:

$$\Psi_{in} = e^{ik_e x} \begin{pmatrix} 1 \\ 0 \end{pmatrix}, \tag{1.12}$$

$$\psi_r = A e^{-ik_e x} \begin{pmatrix} 1 \\ 0 \end{pmatrix} + B e^{ik_h x} \begin{pmatrix} 0 \\ 1 \end{pmatrix}, \tag{1.13}$$

with $k_e = \sqrt{(\mu + E)/t_0}$, $k_h = \sqrt{((\mu - E)/t_0}$, and $t_0 = \hbar^2/2m^*$. Note that for a hole, the direction of the group velocity is opposite to its wave-vector (phase-velocity). In the superconducting region ($x > 0$), we have the following solution for $E < \Delta_0$:

$$\Psi_t = C e^{i\kappa_e x} \begin{pmatrix} u_0 \\ v_0 \end{pmatrix} + D e^{-i\kappa_h x} \begin{pmatrix} v_0 \\ u_0 \end{pmatrix}, \tag{1.14}$$

with $\kappa_e = \sqrt{\mu + \sqrt{E^2 - \Delta_0^2}}$ and $\kappa_h = \sqrt{\mu - \sqrt{E^2 - \Delta_0^2}}$. In the absence of any potential barrier at the NS interface, we have only Andreev reflection, and no normal reflection, which means the coefficients A and D vanish. Assuming all wave vectors equal to the Fermi wave vector and using the continuity of the wave functions, we get $B = v_0/u_0$ and $C = 1/u_0$ [18]. We now use this analysis for an SNS Josephson junction by considering two NS interfaces and writing combined solutions. We assume smooth NS interfaces without any potential barriers. In the normal metal ($0 < x < L$), we have right-moving and left-moving electron-like and hole-like solutions:

$$\Psi_N^{\pm}(x) = A_{\pm} e^{\pm ik_e x} \begin{pmatrix} 1 \\ 0 \end{pmatrix} + B_{\pm} e^{\pm ik_h x} \begin{pmatrix} 0 \\ 1 \end{pmatrix}, \tag{1.15}$$

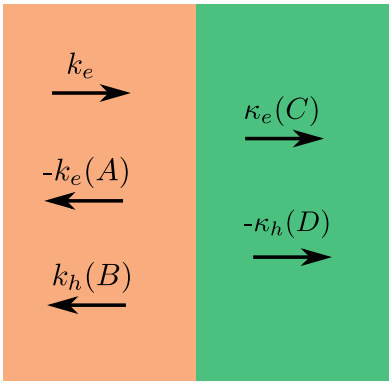

Figure 1.2: Andreev reflection at an NS-interface. The direction of arrows shows the direction of group velocity. The alphabetic coefficients represent reflection or transmission amplitudes (see Eqs. (1.13-1.14)).

In the left superconductor ($x < 0$), the wave functions are:

$$\Psi^{+}_{S_L}(x) = C_{+} e^{i\kappa_h x} \begin{pmatrix} v_0 e^{i\chi_L} \\ u_0 \end{pmatrix}, \tag{1.16}$$

$$\Psi^{-}_{S_L}(x) = C_{-} e^{-i\kappa_e x} \begin{pmatrix} u_0 e^{i\chi_L} \\ v_0 \end{pmatrix}, \tag{1.17}$$

and in the right superconductor ($x > L$):

$$\Psi^{+}_{S_R}(x) = D_{+} e^{i\kappa_e (x-L)} \begin{pmatrix} u_0 e^{i\chi_R} \\ v_0 \end{pmatrix}, \tag{1.18}$$

$$\Psi^{-}_{S_R}(x) = D_{-} e^{-i\kappa_h (x-L)} \begin{pmatrix} v_0 e^{i\chi_R} \\ u_0 \end{pmatrix}. \tag{1.19}$$

Continuity of the wave functions at both NS interfaces gives:

$$\frac{v_0^2}{u_0^2} e^{\pm i(\chi_L - \chi_R)} e^{i(k_e - k_h)L} = 1. \tag{1.20}$$

For $\mu \gg |E|$, we approximate the term $(k_e - k_h)L$ as $\sqrt{\frac{\mu}{t_0}} \frac{E}{\mu} L = \frac{EL}{\Delta_0 \xi_0}$ with $\xi_0 = \hbar v_F / 2\Delta_0$ the superconducting coherence length and v_F the Fermi velocity. Since $|E| < \Delta_0$, we can write:

$$v_0^2 / u_0^2 = \exp(-2i \cos^{-1}(E/\Delta_0)). \tag{1.21}$$

With these substitutes, Eq (1.20) becomes:

$$e^{-2i\cos^{-1}(E/\Delta_0)} e^{\pm i\chi} e^{i\frac{EL}{\Delta_0 \xi_0}} = e^{i2n\pi}, \tag{1.22}$$

with $\chi = \chi_L - \chi_R$ the superconducting phase difference. We write the right-hand side of Eq (1.20) as $e^{i2n\pi}$ for integer values of n. Comparing the exponents, we get [5, 19]:

$$-2\cos^{-1}(E/\Delta_0) \pm \chi + \frac{EL}{\Delta_0 \xi_0} = 2n\pi. \tag{1.23}$$

Depending upon the length of the Josephson junction as compared to the coherence length, the above equation leads to different solutions for Andreev bound state energy in short and long junction regimes.

1.2.2. SHORT JUNCTION REGIME

A Josephson junction lies in the short junction regime if the Thouless energy $E_{Th} = \hbar v_F / L$ of the junction is much larger than the superconducting gap, i.e., $E_{Th} \gg \Delta_0$. An equivalent condition is that the length of the normal region is much shorter than the superconducting coherence length, i.e., $L \ll \xi_0$ [20, 21]. In this limit, most of the Andreev wave function is in the superconducting region and the scattering region acts as a delta function scatterer. As a result, the supercurrent is carried only by the Andreev bound states as the states above the superconducting gap do not vary as a function of the superconducting phase difference. The solution of Eq. (1.23) in this regime gives a sinusoidal Andreev bound state spectrum (see the solid curve in Fig. 1.3) which is independent of the length of the junction:

$$E_{\pm} = \pm \Delta_0 \cos(\chi/2). \tag{1.24}$$

We derived the above result for a single-mode clean one-dimensional Josephson junction. The actual Josephson junction devices are not one-dimensional and do not necessarily have clean NS-interfaces but rather have some potential barrier at the interfaces. As a result, the normal reflection probability becomes finite, thereby limiting the Andreev reflection probability, which makes Eq. (1.24) inapplicable. However, Beenakker showed that for a multichannel short-junction with arbitrary transparency of the NS interfaces, the Andreev bound state energy and consequently the supercurrent depends solely on the transmission eigenvalues of the transmission scattering matrix of the normal scattering region [22]:

$$E_n = \Delta_0 \sqrt{1 - T_n \sin^2(\chi/2)}, \tag{1.25}$$

with T_n the transmission probability corresponding to the n-th eigenvalue. If there is no barrier at the NS interfaces, then the transmission probability is unity, and we get the same expression given in Eq. (1.24). The supercurrent Eq. (1.3) at a finite temperature T is given by [22]

$$I = \frac{e\Delta_0^2}{2\hbar} \sin(\chi) \sum_{n=1}^{N} \frac{T_n}{E_n} \tanh(E_n / 2k_B T). \tag{1.26}$$

In conclusion, we only need transmission eigenvalues of the scattering matrix to calculate the Andreev spectrum and supercurrent in the short junction regime.

1.2.3. LONG JUNCTION REGIME

The long junction regime is the opposite limit to the short junction regime, where most of the Andreev wave function is in the normal scattering region. In the limit that the length of the Josephson junction is much larger than the coherence length ($L \gg \xi_0$), the low energy ($E \ll \Delta_0$) Andreev spectrum is a linear function of χ (the dashed curve in Fig. 1.3) and depends on the length of the junction:

$$E_{n,\pm} = E_{Th}((n + \frac{1}{2})2\pi \mp \chi). \tag{1.27}$$

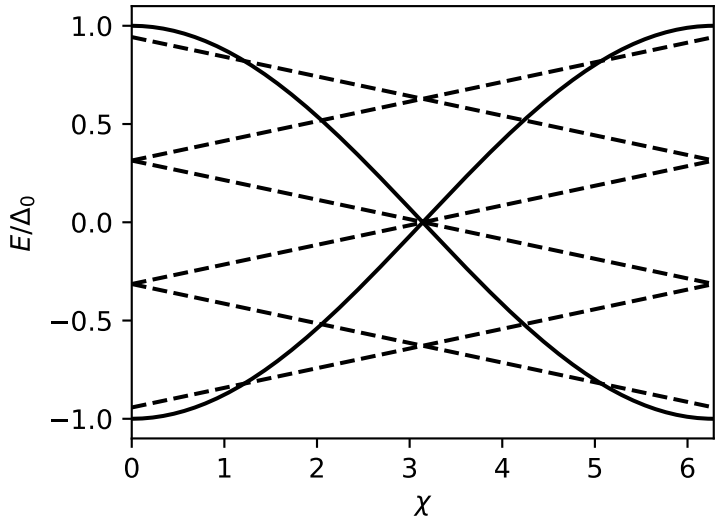

Figure 1.3: Andreev bound states for a short (solid lines) and long (broken lines) Josephson junction.

Because of the longer dwell time of quasiparticles in the normal scattering region, the continuum states above the superconducting gap also vary with respect to χ and contribute significantly to the total supercurrent [23, 24]. Consequently, the calculations in this regime are computationally expensive, making it hard to simulate realistic system sizes.

1.3. BROKEN TIME REVERSAL SYMMETRY

In the previous section, we present a simple calculation of Andreev bound-state energies in a single mode one-dimensional Josephson junction. In the short-junction limit, the Andreev spectrum and supercurrent depend only on the transmission eigenvalues of the transmission scattering matrix and therefore have a universal form. In contrast, the Andreev spectrum and supercurrent do not have a universal form in the long-junction regime. Moreover, in the presence of an applied magnetic field, the current-phase relation becomes non-sinusoidal along with a complicated supercurrent density across the scattering region. Without a magnetic field, electrons and holes retrace their paths and experience a uniform phase. When a perpendicular magnetic field is applied, the quasiparticles experience a space-dependent phase, and their paths change depending upon the magnetic field. As a result, the calculations become more difficult. We show one example of such a case in the short-junction regime, where we apply a perpendicular magnetic field in the normal scattering region. Fig. 1.4 shows the drastic change in the current-phase relation and the supercurrent density map with and without an applied magnetic field.

In this thesis, we use numerical simulations to study supercurrent in realistic short and

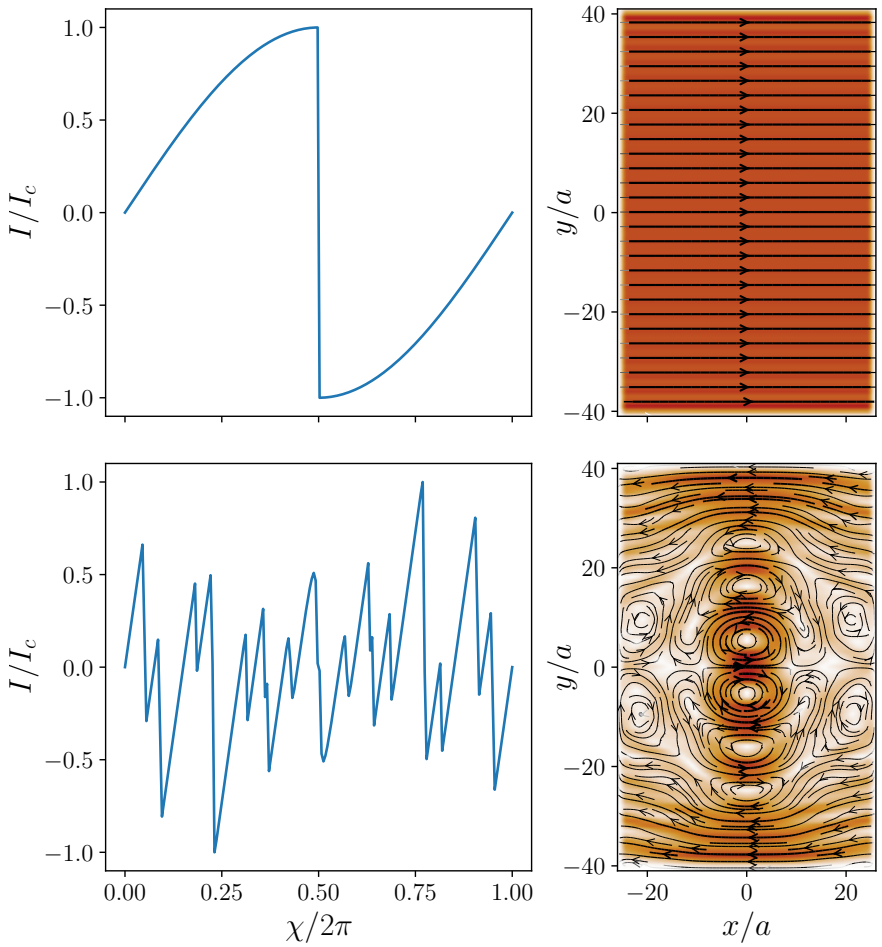

Figure 1.4: The top panel shows the current-phase relation on the left and the supercurrent density map at $\chi = \pi/2$ on the right in the absence of a magnetic field. The bottom panel shows similar plots as the top panel but at a finite magnetic field with flux through the device equal to one flux quantum.

long Josephson junctions in the presence of an applied magnetic field. In chapters 2 and 3, we consider the short-junction regime and use scattering matrix formalism to calculate the supercurrent. In chapter 4, we develop a method to calculate the thermodynamic properties of mesoscopic systems using the kernel polynomial method in combination with sparse diagonalization. We finally apply this method in chapter 5 to calculate the supercurrent in a graphene Josephson junction in the long-junction regime.

1.4. STRUCTURE OF THIS THESIS

Below, we give a brief overview of the topics covered in different chapters of this thesis.

1.4.1. CHAPTER 2: GEOMETRIC FOCUSING OF SUPERCURRENT IN HOURGLASS-SHAPED BALLISTIC JOSEPHSON JUNCTIONS

The response of superconductor–normal-metal–superconductor junctions to magnetic field is complicated and non-universal because all trajectories contributing to supercurrent have a different effective area, and therefore acquire arbitrary magnetic phases. We design an hourglass-shaped Josephson junction where due to the junction symmetry the magnetic phase of every trajectory is approximately equal. By doing so we are able to increase a critical field of the Josephson junction to many flux quanta per junction area. We then analyse how breaking the symmetry condition increases the sensitivity of the junction, and show that our device allows to detect supercurrent carried by ballistic trajectories of Andreev quasiparticles.

1.4.2. CHAPTER 3: TAILORING SUPERCURRENT CONFINEMENT IN GRAPHENE BILAYER WEAK LINKS

The Josephson effect is one of the most studied macroscopic quantum phenomena in condensed matter physics and has been an essential part of the quantum technologies development over the last decades. It is already used in many applications such as magnetometry, metrology, quantum computing, detectors or electronic refrigeration. However, developing devices in which the induced superconductivity can be monitored, both spatially and in its magnitude, remains a serious challenge. In this work, we have used local gates to control confinement, amplitude and density profile of the supercurrent induced in one-dimensional nanoscale constrictions, defined in bilayer graphene-hexagonal boron nitride van der Waals heterostructures. The combination of resistance gate maps, out-of-equilibrium transport, magnetic interferometry measurements, analytical and numerical modelling enables us to explore highly tunable superconducting weak links. Our study opens the path way to design more complex superconducting circuits based on this principle such as electronic interferometers or transition-edge sensors.

1.4.3. CHAPTER 4: HYBRID KERNEL POLYNOMIAL METHOD

The kernel polynomial method allows to sample overall spectral properties of a quantum system, while sparse diagonalization provides accurate information about a few important states. We present a method combining these two approaches without loss of performance or accuracy. We apply this hybrid kernel polynomial method to improve the computation of thermodynamic quantities and the construction of perturbative effective models, in a regime where neither of the methods is sufficient on its own. To achieve this we develop a perturbative kernel polynomial method to compute arbitrary order series expansions of expectation values. We demonstrate the efficiency of our approach on three examples: the calculation of supercurrent and inductance in a Josephson junction, the interaction of spin qubits defined in a two dimensional electron gas, and the calculation of the effective band structure in a realistic model of a semiconductor nanowire.

1.4.4. CHAPTER 5: CRITICAL CURRENT PLATEAU OF GRAPHENE JOSEPHSON JUNCTIONS IN AN IN-PLANE MAGNETIC FIELD

Magnetic field supresses supercurrent in Josephson junctions by making the sign of the contributions of different Andreev states arbitrary. We demonstrate that graphene Josephson junctions are protected from this suppression due to their flatness, which eliminates the orbital effect of an in-plane magnetic field. Further, the lack of spin-orbit interaction combined with the equal value of the Lande g-factor in graphene and thin-film superconducting contacts makes the dispersion of Andreev levels field-independent. As a result, the critical current at zero temperature remains constant up to a critical Zeeman value determined by the junction structure. We compute the universal form of the critical current versus magnetic field in diffusive short junctions, and demonstrate that the critical current remains proportional to the superconducting gap up to magnetic field equal to approximately $0.7B_c$, with B_c the critical field of the superconductor. In the long-junction regime, the critical current at zero temperature remains insensitive up to a Zeeman value of the order of the junction Thouless energy. Finite temperature or spin-orbit coupling destroy the plateau, and therefore we argue that magnetic field dependence of the critical current serves as a probe of these phenomena.

1.4.5. CHAPTER 6: THE AC JOSEPHSON LASER

Superconducting electronic devices have re-emerged as contenders for both classical and quantum computing due to their fast operation speeds, low dissipation and long coherence times. An ultimate demonstration of coherence is lasing. We use one of the fundamental aspects of superconductivity, the ac Josephson effect, to demonstrate a laser made from a Josephson junction strongly coupled to a multi-mode superconducting cavity. A dc voltage bias to the junction provides a source of microwave photons, while the circuit's nonlinearity allows for efficient down-conversion of higher order Josephson frequencies down to the cavity's fundamental mode. The simple fabrication and operation allows for easy integration with a range of quantum devices, allowing for efficient on-chip generation of coherent microwave photons at low temperatures.

REFERENCES

[1] B. D. Josephson, *Possible new effects in superconductive tunnelling,* Physics Letters **1**, 251 (1962).

[2] P. W. Anderson and J. M. Rowell, *Probable observation of the Josephson superconducting tunneling effect,* Phys. Rev. Lett. **10**, 230 (1963).

[3] P. G. de Gennes, *Superconductivity of Metals and Alloys* (Advanced Book Classics, Westview Press, 1966).

[4] A. F. Andreev, *The thermal conductivity of the intermediate state in superconductors,* Sov. Phys. JETP **19**, 1228 (1964).

[5] I. O. Kulik, *Macroscopic quantization and the proximity effect in S-N-S junctions,* Sov. Phys. JETP **30**, 944 (1970).

[6] C. W. J. Beenakker and H. van Houten, *Josephson current through a superconducting quantum point contact shorter than the coherence length,* Phys. Rev. Lett. **66**, 3056 (1991).

[7] B. Ludoph, N. van der Post, E. N. Bratus', E. V. Bezuglyi, V. S. Shumeiko, G. Wendin, and J. M. van Ruitenbeek, *Multiple Andreev reflection in single-atom niobium junctions,* Phys. Rev. B **61**, 8561 (2000).

[8] M. F. Goffman, R. Cron, A. Levy Yeyati, P. Joyez, M. H. Devoret, D. Esteve, and C. Urbina, *Supercurrent in atomic point contacts and Andreev states,* Phys. Rev. Lett. **85**, 170 (2000).

[9] N. Agrait, A. L. Yeyati, and J. M. van Ruitenbeek, *Quantum properties of atomic-sized conductors,* Physics Reports **377**, 81 (2003).

[10] M. L. Della Rocca, M. Chauvin, B. Huard, H. Pothier, D. Esteve, and C. Urbina, *Measurement of the current-phase relation of superconducting atomic contacts,* Phys. Rev. Lett. **99**, 127005 (2007).

[11] T. M. Klapwijk, W. M. v. Huffelen, and D. R. Heslinga, *Semiconductor-coupled Josephson junctions,* IEEE Transactions on Applied Superconductivity **3**, 2873 (1993).

[12] J. R. Gao, J. P. Heida, B. J. van Wees, T. M. Klapwijk, G. Borghs, and C. T. Foxon, *Superconductors coupled with a two-dimensional electron gas in GaAs/AlGaAs and InAs/AlGaSb heterostructures,* Surface Science **305**, 470 (1994).

[13] Y.-J. Doh, J. A. v. Dam, A. L. Roest, E. P. A. M. Bakkers, L. P. Kouwenhoven, and S. D. Franceschi, *Tunable supercurrent through semiconductor nanowires,* Science **309**, 272 (2005).

[14] J. A. v. Dam, Y. V. Nazarov, E. P. A. M. Bakkers, S. D. Franceschi, and L. P. Kouwenhoven, *Supercurrent reversal in quantum dots,* Nature **442**, 667 (2006).

[15] M. Titov and C. W. J. Beenakker, *Josephson effect in ballistic graphene,* Phys. Rev. B **74**, 041401 (2006).

[16] A. G. Moghaddam and M. Zareyan, *Josephson effect in mesoscopic graphene strips with finite width,* Phys. Rev. B **74**, 241403 (2006).

[17] H. B. Heersche, P. Jarillo-Herrero, J. B. Oostinga, L. M. K. Vandersypen, and A. F. Morpurgo, *Bipolar supercurrent in graphene,* Nature **446**, 56 (2007).

[18] G. E. Blonder, M. Tinkham, and T. M. Klapwijk, *Transition from metallic to tunneling regimes in superconducting microconstrictions: Excess current, charge imbalance, and supercurrent conversion,* Phys. Rev. B **25**, 4515 (1982).

[19] T. Schäpers, *Superconductor/Semiconductor Junctions* (Springer, 2003).

[20] K. K. Likharev, *Superconducting weak links,* Rev. Mod. Phys. **51**, 101 (1979).

[21] A. A. Golubov, M. Y. Kupriyanov, and E. Il'ichev, *The current-phase relation in Josephson junctions,* Rev. Mod. Phys. **76**, 411 (2004).

[22] C. W. J. Beenakker, *Universal limit of critical-current fluctuations in mesoscopic Josephson junctions,* Phys. Rev. Lett. **67**, 3836 (1991).

[23] C. Ishii, *Josephson currents through junctions with normal metal barrier,* Prog Theor Phys **44**, 1525 (1970).

[24] J. Bardeen and J. L. Johnson, *Josephson current flow in pure superconducting-normal-superconducting junctions,* Phys. Rev. B **5**, 72 (1972).

2

GEOMETRIC FOCUSING OF SUPERCURRENT IN HOURGLASS-SHAPED BALLISTIC JOSEPHSON JUNCTIONS

This chapter has been previously published as Muhammad Irfan, and Anton Akhmerov, *Geometric focusing of supercurrent in hourglass-shaped ballistic Josephson junctions*, arXiv:1810.04588 (2018).

2.1. INTRODUCTION

The Fraunhofer pattern [1] is a macroscopic quantum interference phenomenon in Josephson Junctions where critical current oscillates in response to an applied magnetic field in a fashion similar to the Fraunhofer diffraction of light passing through a single slit. The applied magnetic field spatially modulates the phase which a quasiparticle acquires while traversing from one superconductor to another [2–4]. Because the contribution of each trajectory to supercurrent is an oscillatory function of this phase, contributions of different trajectories interfere. Because of being able to distinguish different trajectories, Fraunhofer measurements are used to determine a spatial distribution of supercurrents [5–9]. Importantly, such measurements allow to distinguish current carried by the edge states from bulk conduction.

In a ballistic superconductor-normal-metal-superconductor (SNS) Josephson junction (JJ), different Andreev trajectories acquire different phases depending upon the path they follow. The acquired phase is proportional to the trajectory area, as illustrated in Fig. 2.1(a). The Fraunhofer pattern due to the interference of these trajectories depend on the geometry of the device [10–14]. Furthermore, Hendrik et. al., [15] show that the Fraunhofer pattern is sensitive to the reflection from the edges of the device. At low magnetic field, the edge effects make the critical current nonzero at all values of the magnetic field and on the other accelerate the overall suppression of the critical current. Both of these effects do not require ballistic trajectories. It is therefore hard to identify the ballistic nature of Andreev trajectories from a Fraunhofer measurement, and in particular Refs. [5, 6] present a universal algorithm for interpreting any dependence of critical current on magnetic field as an inhomogeneous tunnel junction.

Here, we design a device allowing to detect ballistic supercurrent based on a *qualitative* change in the Fraunhofer pattern. We show that in an hourglass-shaped JJ, shown in Fig. 2.1(b), the trajectories approximately accumulate the same phase, as shown in Fig. 2.1(c). This phase matching condition provides a constructive interference of supercurrent also at high magnetic fields and results in a slow decay of critical current with magnetic field. Breaking the spatial symmetry, by making the device geometrically asymmetric (Fig. 2.1(d)), by disorder (Fig. 2.1(e)), or by applying an asymmetric gate potential then restores the conventional Fraunhofer pattern.

The organization of this chapter is as follows. We first introduce the physical system in Sec. 2.2. In Sec. 2.3, we present the quasiclassical analysis of supercurrent in an hourglass device. In Sec. 2.4, we introduce the scattering matrix formalism and support our conclusions using numerical simulations based on a quantum-mechanical model. Finally, we summarize our analysis in Sec. 2.5.

2.2. SYSTEM

We consider an hourglass-shaped Josephson junction with the separation between the superconducting contacts L, contact width W, and the bottleneck width W_b as shown in Fig. 2.1(b). The magnetic field B in the scattering region is constant and perpendicular to the junction plane while being completely expelled from the superconductors. We choose the Landau gauge, resulting in the the vector potential $\boldsymbol{A} = (-By\hat{x}, 0)$. The Hamiltonian of

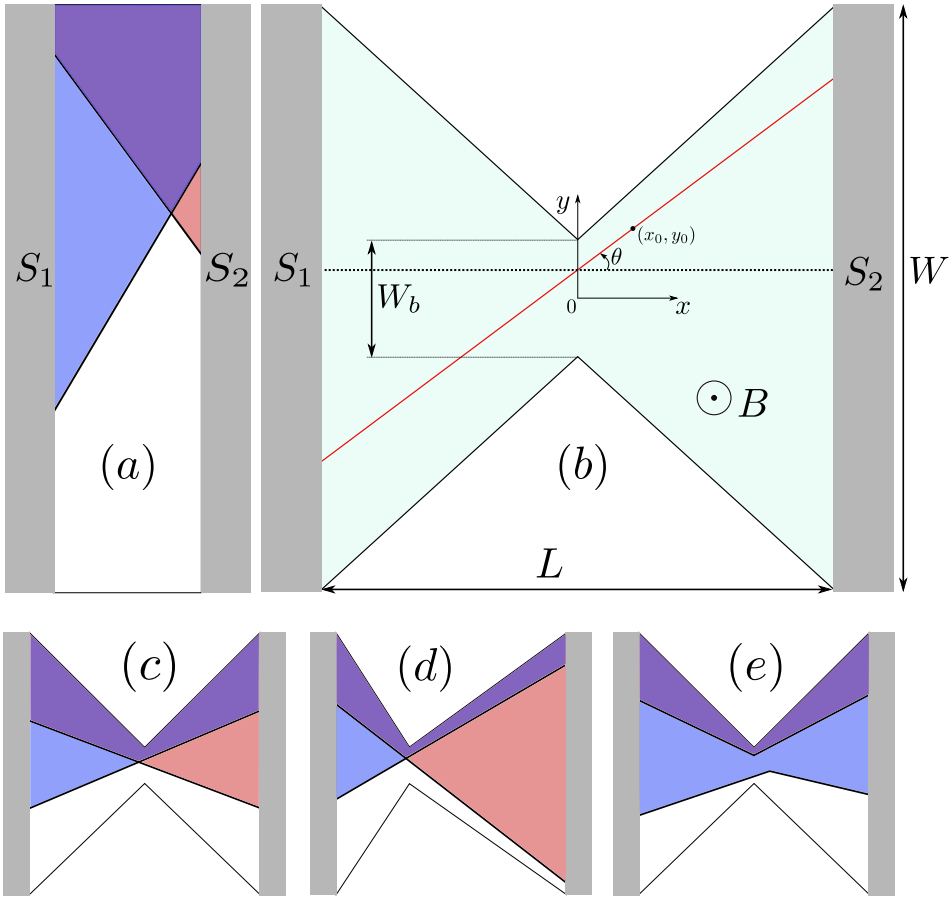

Figure 2.1: Panel (a): Two Andreev trajectories (black lines) in an SNS junction accumulate a magnetic phase proportional to the area enclosed by such a trajectory (shaded regions). Panel (b): In an hourglass-shaped SNS junction with a narrow opening W_b all current-carrying trajectories pass through the middle. Panel (c): The magnetic phases acquired by these trajectories in a symmetric device are approximately equal. Breaking the reflection symmetry [panel (d)] or introducing disorder scattering [panel (e)] makes the magnetic phases different.

the scattering region reads:

$$H = \frac{(\boldsymbol{p} - e\boldsymbol{A})^2}{2m} - \mu + V(\boldsymbol{r}), \tag{2.1}$$

with $\boldsymbol{p}$ the momentum operator, e the electron charge, μ the chemical potential, m the quasiparticle mass, and $V(\boldsymbol{r})$ the electrostatic potential in the scattering region. While modeling superconducting leads, we assume a step-like superconducting pairing poten-

tial

$$\Delta = \begin{cases} \Delta e^{i\phi_L} & x < -L/2, \\ \Delta e^{i\phi_R} & x > L/2, \\ 0 & -L/2 \le x \le L/2, \end{cases} \tag{2.2}$$

with ϕ_L (ϕ_R) the superconducting phase in left (right) lead.

2.3. QUASICLASSCIAL CALCULATION OF SUPERCURRENT

We start with a quasiclassical trajectory approach following Ref. [16] to calculate supercurrent through the JJ before turning to a quantum-mechanical treatment. The main underlying assumption for quasiclassics is that the Fermi wavelength is much smaller than any feature of the system geometry. Additionally, we consider the low field regime where the cyclotron radius is much larger than the system size, and trajectories are composed of segments of straight lines. Supercurrent is then carried by closed trajectories where an electron originates from one superconductor, reaches another one, transforms into a hole via Andreev reflection, retraces back its original path, and finally transforms back into an electron via another Andreev reflection. The supercurrent as a function of superconducting phase difference $\phi \equiv \phi_L - \phi_R$ due to all such trajectories is given by:

$$I(\phi) = \frac{k_F}{2\pi} \int_{-W/2}^{W/2} dy_0 \int_{\theta_{\min}}^{\theta_{\max}} \delta I\left(y_0, \theta, \phi\right) \cos\theta \, d\theta, \tag{2.3}$$

with k_F the Fermi wavevector and δI the supercurrent due to a single trajectory passing through a point (x_0, y_0) making an angle θ with the x-axis (Fig. 2.1(b)). In the presence of a perpendicular magnetic field, the superconducting phase experienced by a trajectory is modulated by a path dependent magnetic phase ξ:

$$\xi = \frac{2e}{\hbar} \int_{S_1}^{S_2} \boldsymbol{A} d\boldsymbol{l}, \tag{2.4}$$

with $\hbar$ the reduced Planck's constant. Here, we consider homogeneous normal-metal–superconductor interfaces and angle independent transmission with a universal form of supercurrent:

$$\delta I\left(y_0, \theta, \phi\right) = f\left(L, \phi - \xi\left(y_0, \theta\right)\right), \tag{2.5}$$

with following properties

$$f\left(L, \phi + 2\pi\right) = f\left(L, \phi\right) = -f\left(L, -\phi\right). \tag{2.6}$$

The specific form of $f\left(L, \phi\right)$ depends on the type of a Josephson junction [17–22], however because the field sensitivity is determined by the phase matching condition, we expect that our results hold for any form of the current-phase relation. To illustrate this we consider two limiting cases: the long Josephson junction at $T = 0$ and the high temperature

regime. In a long Josephson junction, the current-phase relation at zero temperature is sawtooth-shaped [18, 19]:

$$f\left(L,\phi\right) = I_c\left(\frac{\phi}{\pi} - 2\left\lfloor\frac{1}{2} + \frac{\phi}{2\pi}\right\rfloor\right) \tag{2.7}$$

with $I_c \approx eE_T/2\hbar$ the critical current value, E_T the Thouless energy, and $\lfloor\phi\rfloor$ the floor function. At a sufficiently high temperature, the current-phase relation is of the sinusoidal form [23]:

$$f\left(L,\phi\right) = I_c \sin\left(\phi\right), \tag{2.8}$$

with I_c the critical current which depends on a given Josephson junction.

Because of the device geometry, most supercurrent-carrying trajectories do not scatter of the sample boundaries. Therefore in our gauge choice, the path dependent magnetic phase ξ for a trajectory passing through a point (x_0, y_0) and making an angle θ with the x-axis is:

$$\xi = \frac{2eBL}{\hbar}\left(y_0 - x_0\tan\theta\right). \tag{2.9}$$

The requirement that a trajectory does not reflect at a boundary reads:

$$\theta_{\min} < |\theta| < \theta_{\max}, \tag{2.10a}$$

$$\theta_{\min} = \arctan\left[\max\left(\frac{-W_b - 2y_0}{L}, \frac{-W/2 - y_0}{L}\right)\right], \tag{2.10b}$$

$$\theta_{\max} = \arctan\left[\min\left(\frac{W_b - 2y_0}{L}, \frac{W/2 - y_0}{L}\right)\right]. \tag{2.10c}$$

In an asymmetric hourglass junction the bottleneck position is shifted by an offset δL towards one of the superconducting leads, such that position of the bottleneck is at a distance $L_1 = L/2 - \delta L$ from one lead and $L_2 = L/2 + \delta L$ from the other. If the offset $\delta L > W_b/2$ then straight trajectories starting from the top or bottom corners of the left superconducting lead do not reach the other lead. This results in the modification of the integration limits in Eq. (2.3) from W to the effective junction width

$$W_{eff} = \frac{L - 2\delta L}{L + 2\delta L}\left(W/2 + W_b/2\right) + W_b/2. \tag{2.11}$$

The limits of the integral over angle $\theta_{\min}$ and $\theta_{\max}$ change to

$$\theta_{\min} < |\theta| < \theta_{\max}, \tag{2.12a}$$

$$\theta_{\min} = \arctan\left[\max\left(\frac{-W_b/2 - y_0}{L_1}, \frac{-W/2 - y_0}{L}\right)\right], \tag{2.12b}$$

$$\theta_{\max} = \arctan\left[\min\left(\frac{W_b/2 - y_0}{L_1}, \frac{W/2 - y_0}{L}\right)\right]. \tag{2.12c}$$

In Fig. 2.2, we show the Fraunhofer patterns for a symmetric and three different asymmetric JJs as a function of magnetic flux $\Phi = B(W_b + W)L/2$ through the device using different current-phase relationships. We confirm our expectation that the critical current of the symmetric hourglass device is less sensitive to magnetic field and decays

slower than that in a regular Fraunhofer pattern. Specifically, the critical current vanishes at a magnetic field scale $B^* \sim \Phi_0/W_b L$. Making the device asymmetric increases the sensitivity of the supercurrent to magnetic field, making the characteristic field scale $B^* \sim \Phi_0/WL$, similar to that of a conventional SNS junction. We also observe that this behavior does not depend on the specific form of the current-phase relation. For the rest of the quasiclassical analysis, we use the sinusoidal current-phase relation.

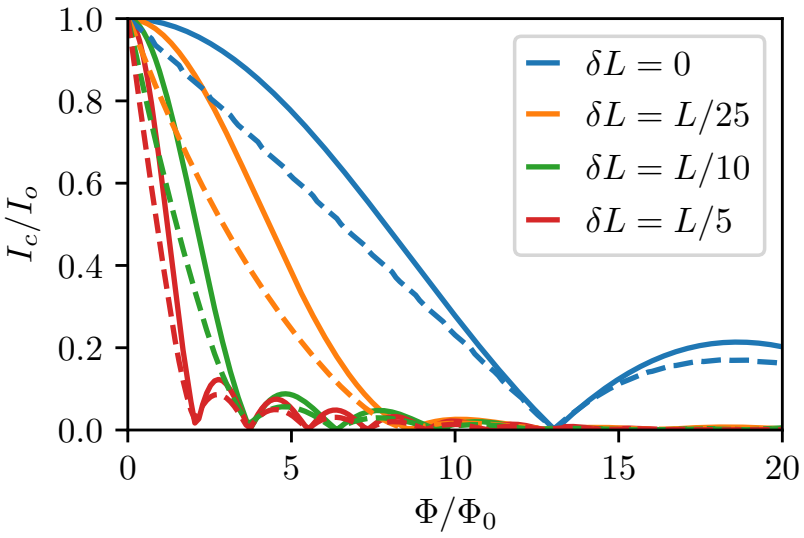

Figure 2.2: Critical current as a function of magnetic flux $\Phi = B(W_b + W)L/2$ through the normal scattering region, calculated quasiclassically for symmetric and asymmetric hourglass-shaped Josephson junctions of dimension $L = W$ and $W_b = L/25$. The asymmetry is controlled by δL, the displacement of the hourglass bottleneck from the middle of the device along x-axis. The solid lines are calculated using a sinusoidal current-phase relation while broken lines using a sawtooth current-phase relation.

A more practical way to break the phase matching condition of Fig. 2.1(c) is by tuning carrier densities across the bottleneck via a local gate potential. We incorporate this effect in the quasiclassical calculations by introducing two Fermi wavevectors k_{FL} and k_{FR} on the left and right side of the bottleneck respectively. Owing to this difference in carrier densities, a trajectory starting at $x = -L/2$ with angle θ enters the right side of the hourglass at a different angle θ' which depends on the ratio of Fermi wave vectors as

$$\theta' = \arcsin\left(\frac{k_{FL}}{k_{FR}}\sin\theta\right). \tag{2.13}$$

As a result, the corresponding Peierls phase factor (2.4) acquires the form

$$\xi = \frac{2eBL}{\hbar}\left[y_0 + \left(3\tan\theta + \tan\theta'\right)\frac{L}{8}\right]. \tag{2.14}$$

(Here and later we assume $k_{FL} < k_{FR}$.) The conditions on the angle θ of the incident trajectories for integration is given by:

$$\arctan\left(\frac{-W_b - 2y_0}{L}\right) < \theta < \arctan\left(\frac{W_b - 2y_0}{L}\right), \tag{2.15a}$$

$$|y_0 + L\left(\tan\theta + \tan\theta'\right)/2| < W/2. \tag{2.15b}$$

Depending upon the Fermi wavevector mismatch, more trajectories can now reach the other interface without edge scattering as compared to the case of a symmetric hourglass device with equal carrier concentrations. We show the results for different Fermi wavevector mismatch in Fig. 2.3. Similar to making the junction itself asymmetric, introducing a carrier density mismatch restores the sensitivity of the supercurrent to the magnetic field.

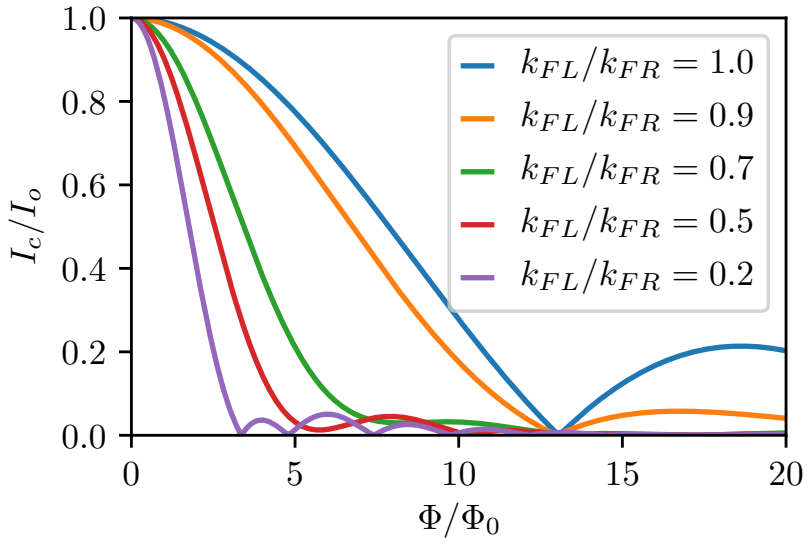

Figure 2.3: Critical current as a function of flux $\Phi = B(W_b + W)L/2$ through the normal scattering region, calculated quasiclassically for the symmetric hourglass geometry of dimensions $L = W$ and $W_b = L/25$. The Fermi wave vector mismatch quantifies the difference of carrier densities on both sides of the hourglass bottleneck.

2.4. TIGHT-BINDING NUMERICAL CALCULATION OF SUPERCURRENT

To compare the results of the quasiclassical analysis with a quantum mechanical model, we numerically calculate the supercurrent based on a tight-binding model using the scattering matrix approach [24]. The numerical calculations take into account effects

that we neglected in quasiclassics: reflections from sample boundaries, finite Fermi wavelength, finite cyclotron radius, and potentially disorder scattering.

We consider short junction limit due to the simplicity of its numerical implementation, however we expect that relaxing this approximation will not alter our conclusions. In the short junction limit, the scattering matrix condition for Andreev bound state reads [25]:

$$\begin{bmatrix} 0 & -iA^\dagger \\ iA & 0 \end{bmatrix} \Psi_{\text{in}} = E/\Delta \Psi_{\text{in}}, \tag{2.16}$$

$$A \equiv \frac{1}{2}\left(r_A s - s^T r_A\right) \tag{2.17}$$

with $\Psi_{\text{in}} = (\Psi^e_{\text{in}}, \Psi^h_{\text{in}})$ a vector of complex coefficients describing a wave incident on the junction in the basis of modes incoming from the superconducting leads into the normal region. The scattering matrix s is due to the normal scattering region, whereas r_A is due to Andreev reflection at the superconductor-normal metal interface. In the basis where the outgoing modes are time-reversed partners of the incoming modes, the matrix r_A is given by

$$r_A = \begin{bmatrix} ie^{i\phi/2}\mathbf{1}_{n_1} & 0 \\ 0 & ie^{-i\phi/2}\mathbf{1}_{n_2} \end{bmatrix}, \tag{2.18}$$

with ϕ the superconducting phase difference between the two superconducting leads.

We square Eq. (2.16), making it block-diagonal and take one of the subblocks to obtain an equivalent eigenproblem for the Andreev bound states:

$$A^\dagger A \Psi^e_{\text{in}} = \frac{E^2}{\Delta^2}\Psi^e_{\text{in}}. \tag{2.19}$$

Differentiating this with respect to ϕ we obtain:

$$\frac{dE}{d\phi} = \frac{\Delta^2}{2}\frac{1}{E}\left\langle \Psi^e_{\text{in}} \middle| \frac{d(A^\dagger A)}{d\phi} \middle| \Psi^e_{\text{in}} \right\rangle. \tag{2.20}$$

Further substituting $d(A^\dagger A)/d\phi$ from Eqs. (2.17, 2.18) provides us with a closed form expresion for the supercurrent when combined with the eigenvectors from the Eq. (2.19). We finally arrive to the supercurrent

$$I = -\frac{2e}{\hbar}\sum_p \tanh(E_p/2k_BT)\frac{dE_p}{d\phi}, \tag{2.21}$$

with $dE_p/d\phi$ obtained from Eqs. (2.19, 2.20).

We calculate the normal state scattering matrix using the Kwant software package [26]: we discretize the Hamiltonian Eq. (2.1) on a square lattice with lattice constant a and a shape of an hourglass, as shown in Fig. 2.1(b). To analyse the effect of disorder we consider a random onsite potential, uniformly varying between $-U/2$ to $U/2$. The quasiparticle mean free path l_0 in the scattering region is then given by [27]

$$l_0 = \frac{6\lambda_F^3}{\pi^3 a^2}\left(\frac{\mu}{U}\right)^2, \tag{2.22}$$

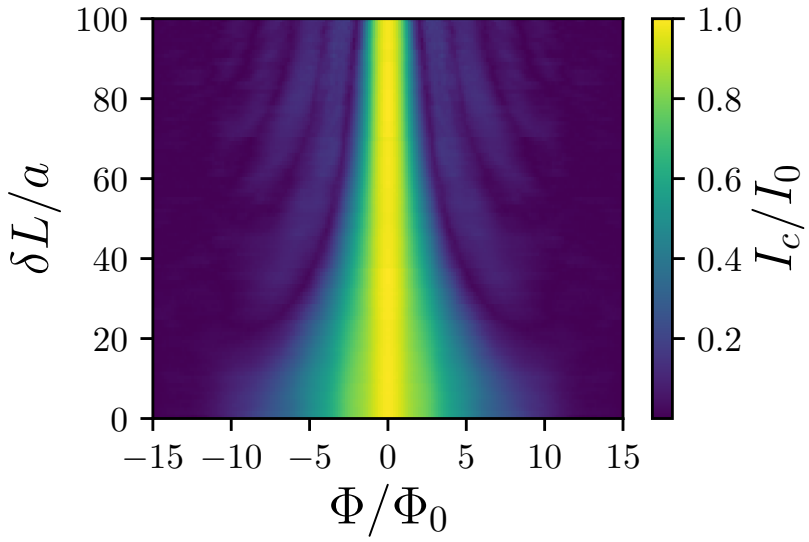

Figure 2.4: Critical current as a function of applied magnetic field and the asymmetry of the device with $W = L = 500a$ and $W_b = 20a$.

with λ_F Fermi wavelength. In our simulation, we chose $\mu = 1.01t$, with t the nearest-neighbour hopping constant. We then evaluate the supercurrent at $T = 0$.

To confirm the quasiclassical simulations we compute the supercurrent in an asymmetric device, with the results shown in Fig. 2.4 for a system of length $L = 500a$, lead width $W = 500a$, and the width of bottleneck $W_b = 20a$. In a symmetric device we observe a monotonically decaying bell-shaped pattern, with the lack of the secondary lobes likely due to the small ratio $\lambda_F/W_b \approx 3$. We observe that the predictions of the quasiclassical calculations agree with those of the fully quantum-mechanical one and confirm that the device asymmetry controls the sensitivity of the critical current to the magnetic field.

The effect of the disorder scattering on the geometric focusing is shown in the Fig. 2.5. The central lobe of the Fraunhofer pattern decays much faster in the presence of a uniform disorder as compared to the ballistic case, recovering the magnetic field sensitivity of a conventional junction when $l_0 \sim L$. This qualitative change in the Fraunhofer pattern makes the hourglass SNS junction uniquely sensitive to disorder scattering and even allows to distinguish purely ballistic transport from even quasi-ballistic transport when the mean free path is comparable to the system size.

Finally we compute the supercurrent density, as shown in Fig. 2.6, for three different values of magnetic flux through the device and with $\phi = \pi/2$. The left panel shows the supercurrent distribution for no magnetic field, with the current density approximately matching that of the normal current. In the middle panel at magnetic flux $\Phi = 3\Phi_0$, we see the effect of the magnetic field which bends different trajectories in a vortex-like structure. While the decrease of critical current at this flux value in Fig. 2.5 from zero magnetic field

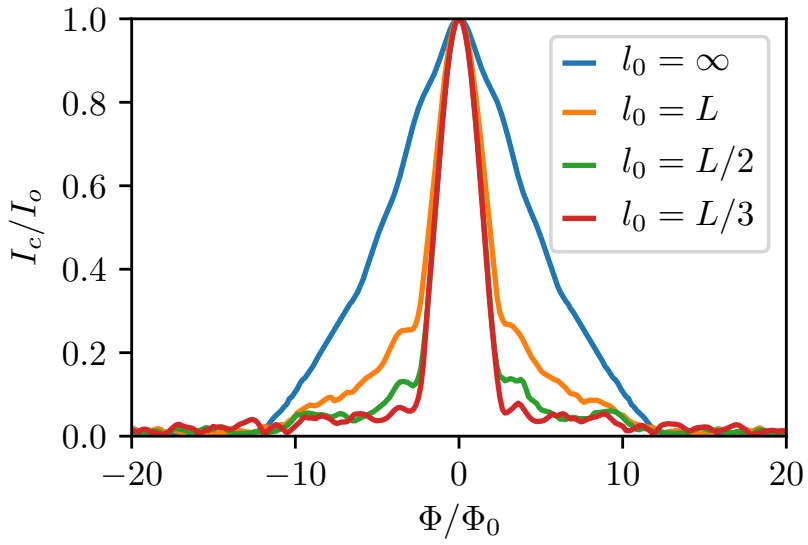

Figure 2.5: Critical current as a function of magnetic flux through the normal scattering region for ballistic and diffusive Josephson junctions of dimensions $L = W = 500a$ and $W_b = 20a$, calculated from Eq. 2.21 using the tight-binding calculations. The mean free path l_0 is determined by the strength of disorder.

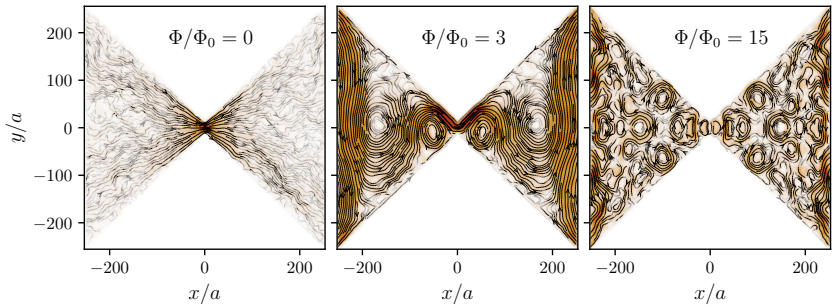

Figure 2.6: Supercurrent density maps for a system of size $W = L = 500a$, $W_b = 20a$ at the superconducting phase $\phi = \pi/2$ for different values of total flux $\Phi = B(W_b + W)L/2$ through the normal scattering region. Left panel: At zero magnetic flux, straight trajectories give maximum supercurrent. Middle panel: At $\Phi = 3\Phi_0$, a supercurrent vortex appears, accompanies by only a slight decrease in net supercurrent [*cf.* Fig. 2.5]. Right panel: At high magnetic flux $\Phi = 15\Phi_0$, several supercurrent vortex appear while the net supercurrent vanishes.

case is small, we see a completely different supercurrent density profile. The additional supercurrent is mediated by the trajectories that start and end the same superconductor: in a device with a thin bottleneck, these trajectories comprise a majority. The observation of the change in the supercurrent distribution by a scanning magnetometer [28, 29] may then serve as an independent confirmation of the focusing effect. The right panel

shows a supercurrent density map at a higher magnetic field with many supercurrent vortices [11, 16, 30] and vanishing overall supercurrent.

2.5. CONCLUSIONS

We have proposed a strategy to observe supercurrent carried by ballistic trajectories by identifying a geometry where ballistic supercurrent vanishes at a larger magnetic field scale Φ_0/W_bL instead of the conventional Φ_0/WL. We confirm our predictions using both quasiclassical and fully quantum-mechanical analysis and confirm that breaking the phase cancellation condition leads to a faster decay of the central lobe and a conventional Fraunhofer pattern. Although we consider a conventional two-dimensional electron gas in our analysis, we expect that the proposed phenomenon should exist in any mesoscopic Josephson device due to being a geometrical effect. Therefore, the proposed device design is well within the reach of the current experimental technology and can be implemented using both semiconducting quantum wells [31, 32] or high-quality graphene Josephson junctions [9, 33, 34].

The source code and data used for figures in this work is available at [35].

REFERENCES

[1] J. M. Rowell, *Magnetic field dependence of the Josephson tunnel current,* Phys. Rev. Lett. **11**, 200 (1963).

[2] V. P. Galaiko, *Quantization of electron excitations in S-N-S film contacts in a magnetic field,* Sov. Phys. JETP **30**, 514 (1970).

[3] V. P. Galaiko and E. V. Bezuglyi, *Magnetic quantization and absorption of ultrasound in superconductors in the intermediate state,* Sov. Phys. JETP **33**, 796 (1971).

[4] G. A. Gogadze and I. O. Kulik, *Oscillatory and resonant effects in S-N-S junctions in a magnetic field,* Sov. Phys. JETP **33**, 984 (1971).

[5] R. C. Dynes and T. A. Fulton, *Supercurrent density distribution in Josephson junctions,* Phys. Rev. B **3**, 3015 (1971).

[6] H.-Y. Hui, A. M. Lobos, J. D. Sau, and S. Das Sarma, *Proximity-induced superconductivity and Josephson critical current in quantum spin Hall systems,* Phys. Rev. B **90**, 224517 (2014).

[7] S. Hart, H. Ren, T. Wagner, P. Leubner, M. Mühlbauer, C. Brüne, H. Buhmann, L. W. Molenkamp, and A. Yacoby, *Induced superconductivity in the quantum spin Hall edge,* Nature Physics **10**, 638 (2014).

[8] V. S. Pribiag, A. J. A. Beukman, F. Qu, M. C. Cassidy, C. Charpentier, W. Wegscheider, and L. P. Kouwenhoven, *Edge-mode superconductivity in a two-dimensional topological insulator,* Nature Nanotechnology **10**, 593 (2015).

[9] M. T. Allen, O. Shtanko, I. C. Fulga, A. R. Akhmerov, K. Watanabe, T. Taniguchi, P. Jarillo-Herrero, L. S. Levitov, and A. Yacoby, *Spatially resolved edge currents and guided-wave electronic states in graphene,* Nature Physics **12**, 128 (2016).

[10] V. Barzykin and A. M. Zagoskin, *Coherent transport and nonlocality in mesoscopic SNS junctions: anomalous magnetic interference patterns,* Superlattices and Microstructures **25**, 797 (1999).

[11] J. C. Cuevas and F. S. Bergeret, *Magnetic interference patterns and vortices in diffusive SNS junctions,* Phys. Rev. Lett. **99**, 217002 (2007).

[12] F. Chiodi, M. Ferrier, S. Guéron, J. C. Cuevas, G. Montambaux, F. Fortuna, A. Kasumov, and H. Bouchiat, *Geometry-related magnetic interference patterns in long SNS Josephson junctions,* Phys. Rev. B **86**, 064510 (2012).

[13] M. Alidoust and J. Linder, *φ-state and inverted Fraunhofer pattern in nonaligned Josephson junctions,* Phys. Rev. B **87**, 060503 (2013).

[14] M. Amado, A. Fornieri, F. Carillo, G. Biasiol, L. Sorba, V. Pellegrini, and F. Giazotto, *Electrostatic tailoring of magnetic interference in quantum point contact ballistic Josephson junctions,* Phys. Rev. B **87**, 134506 (2013).

[15] H. Meier, V. I. Fal'ko, and L. I. Glazman, *Edge effects in the magnetic interference pattern of a ballistic SNS junction,* Phys. Rev. B **93**, 184506 (2016).

[16] V. P. Ostroukh, B. Baxevanis, A. R. Akhmerov, and C. W. J. Beenakker, *Two-dimensional Josephson vortex lattice and anomalously slow decay of the Fraunhofer oscillations in a ballistic SNS junction with a warped Fermi surface,* Phys. Rev. B **94**, 094514 (2016).

[17] I. O. Kulik, *Macroscopic quantization and the proximity effect in S-N-S junctions,* Sov. Phys. JETP **30**, 944 (1970).

[18] C. Ishii, *Josephson currents through junctions with normal metal barriers,* Prog Theor Phys **44**, 1525 (1970).

[19] J. Bardeen and J. L. Johnson, *Josephson current flow in pure superconducting-normal-superconducting junctions,* Phys. Rev. B **5**, 72 (1972).

[20] A. V. Svidzinsky, T. N. Antsygina, and E. N. Bratus', *Concerning the theory of the Josephson effect in pure SNS junctions,* J Low Temp Phys **10**, 131 (1973).

[21] I. O. Kulik and A. N. Omel'yanchuk, *Contribution to the microscopic theory of the Josephson effect in superconducting bridges,* JETP Lett. **21**, 96 (1975).

[22] A. A. Golubov, M. Y. Kupriyanov, and E. Il'ichev, *The current-phase relation in Josephson junctions,* Rev. Mod. Phys. **76**, 411 (2004).

[23] K. K. Likharev, *Superconducting weak links,* Rev. Mod. Phys. **51**, 101 (1979).

[24] C. W. J. Beenakker, *Universal limit of critical-current fluctuations in mesoscopic Josephson junctions,* Phys. Rev. Lett. **67**, 3836 (1991).

[25] B. van Heck, S. Mi, and A. R. Akhmerov, *Single fermion manipulation via superconducting phase differences in multiterminal Josephson junctions,* Phys. Rev. B **90**, 155450 (2014).

[26] C. W. Groth, M. Wimmer, A. R. Akhmerov, and X. Waintal, *Kwant: a software package for quantum transport,* New J. Phys. **16**, 063065 (2014).

[27] T. Ando, *Quantum point contacts in magnetic fields,* Phys. Rev. B **44**, 8017 (1991).

[28] L. Embon, Y. Anahory, Z. L. Jelic, E. O. Lachman, Y. Myasoedov, M. E. Huber, G. P. Mikitik, A. V. Silhanek, M. V. Milosevic, A. Gurevich, and E. Zeldov, *Imaging of super-fast dynamics and flow instabilities of superconducting vortices,* Nature Communications **8**, 85 (2017).

[29] J. R. Kirtley, L. Paulius, A. J. Rosenberg, J. C. Palmstrom, D. Schiessl, C. L. Jermain, J. Gibbons, C. M. Holland, Y.-K.-K. Fung, M. E. Huber, M. B. Ketchen, D. C. Ralph, G. W. G. Jr, and K. A. Moler, *The response of small SQUID pickup loops to magnetic fields,* Supercond. Sci. Technol. **29**, 124001 (2016).

[30] F. S. Bergeret and J. C. Cuevas, *The vortex state and Josephson critical current of a diffusive SNS junction,* J Low Temp Phys **153**, 304 (2008).

[31] H. J. Suominen, J. Danon, M. Kjaergaard, K. Flensberg, J. Shabani, C. J. Palmstrøm, F. Nichele, and C. M. Marcus, *Anomalous Fraunhofer interference in epitaxial superconductor-semiconductor Josephson junctions,* Phys. Rev. B **95**, 035307 (2017).

[32] N. Pankratova, H. Lee, R. Kuzmin, M. Vavilov, K. Wickramasinghe, W. Mayer, J. Yuan, J. Shabani, and V. E. Manucharyan, *The multi-terminal Josephson effect,* arXiv:1812.06017 [cond-mat] (2018).

[33] R. Kraft, J. Mohrmann, R. Du, P. B. Selvasundaram, M. Irfan, U. N. Kanilmaz, F. Wu, D. Beckmann, H. Löhneysen, R. Krupke, A. Akhmerov, I. Gornyi, and R. Danneau, *Tailoring supercurrent confinement in graphene bilayer weak links,* Nature Communications **9**, 1722 (2018).

[34] A. W. Draelos, M.-T. Wei, A. Seredinski, H. Li, Y. Mehta, K. Watanabe, T. Taniguchi, I. V. Borzenets, F. Amet, and G. Finkelstein, *Supercurrent flow in multiterminal graphene Josephson junctions,* Nano Lett. **19**, 1039 (2019).

[35] M. Irfan and A. R. Akhmerov, *Geometric focusing of supercurrent in hourglass-shaped ballistic Josephson junctions* (Zenodo, 2018).

3

TAILORING SUPERCURRENT CONFINEMENT IN GRAPHENE BILAYER WEAK LINKS

This chapter has been previously published as Rainer Kraft, Jens Mohrmann, Renjun Du, Pranauv Balaji Selvasundaram, Muhammad Irfan, Umut Nefta Kanilmaz, Fan Wu, Detlef Beckmann, Hilbert von Löhneysen, Ralph Krupke, Anton Akhmerov, Igor Gornyi, and Romain Danneau, *Tailoring supercurrent confinement in graphene bilayer weak links*, Nat. Commun. **9**, 1722 (2018).
My contribution to this work is the tight-binding simulation of bilayer graphene Josephson junction.

3.1. INTRODUCTION

Superconductivity can be induced in a material by direct contact to a superconductor. This proximity effect allows the transmission of Andreev pairs from a superconducting electrode to another when these are close enough. The Josephson effect can then be measured as it is observed in tunnel junctions [1–3]. However, the tuning of the dissipationless current in such Josephson junctions is not possible without changing its geometry or temperature. By replacing the tunnel junction by a so-called weak link [4, 5], *i.e.* any kind of conductive system, the supercurrent may flow over a much larger distance than the couple of nanometers of a tunnel barrier. The magnitude of the supercurrent mainly depends on the contact transparency, the disorder in the weak link and the temperature [4].

Many different types of materials and systems have been used as weak links, ranging from mesoscopic diffusive metallic wires [6], two-dimensional (2D) electron gas [7], graphene [8], topological insulators [9–14] and quantum dots [15], as well as atomic contacts [16]. When graphene is utilised as a weak link, the Josephson effect can be tuned by electrostatic gating [8, 17–23] and, thanks to edge connection which provides very low contact resistance [24], it is possible to measure large supercurrent amplitudes as well as ballistic interferences [25–29]. However, in spite of these excellent predispositions to mediate superconductivity, a full control of the supercurrent both in its amplitude and spatial distribution has not been demonstrated up to now. One of the reasons behind this is the difficulty to confine charge carriers in graphene due to the absence of back scattering and Klein tunnelling [30]. The use of bilayer graphene (BLG) could circumvent these problems since it is possible to engineer an electronic band gap by breaking the lattice inversion symmetry of the AB-stacked bilayer [31, 32]. Indeed, by means of local gating, BLG can provide a way to shape the supercurrent distribution and allow a complete monitoring of proximity induced superconductivity. Here, we have used edge connected BLG-hexagonal boron nitride (hBN) heterostructures as a medium for induced superconductivity, and use a quantum point contact (QPC)-like geometry to study supercurrent confinement.

3.2. RESULTS

3.2.1. READING A DUAL GATE MAP AND INDUCING A 1D CONSTRICTION

The sample geometry used in this study is depicted in Fig. 3.1. Following the fabrication method of Wang *et al.* [24], we employ BLG encapsulated between hBN multilayers connected from the edge of the mesa with superconducting titanium/aluminium electrodes. The constriction is realised by inducing displacement fields between an overall pre-patterned back-gate and a local top-gate designed in a QPC-like split-gate geometry (see Fig. 3.1). Two devices were measured which show similar behaviour, here we present the data based on the shortest sample (details on the sample fabrication are presented in Supplementary Note 3.4.1).

The normal state characteristics of our sample show a residual charge carrier density as low as $2.6 \cdot 10^{10}\,\mathrm{cm}^{-2}$, well developed Landau fans in magnetotransport experiments as well as multiple Fabry-Pérot interferences generated by the charge carriers travelling back and forth within the several cavities formed in our system (see Supplementary Note 3.4.2,

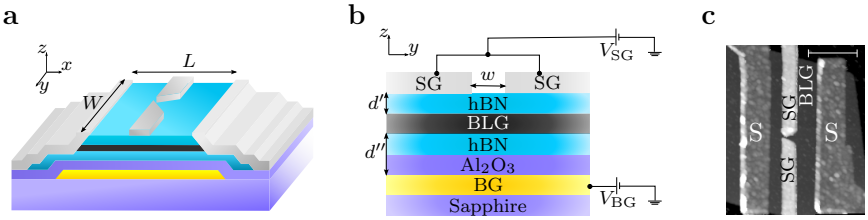

Figure 3.1: **Device geometry. a,** 3D Schematics of the device and **b,** cross-sectional view as a cut through the dual-gated region. The device consists of a hBN-BLG-hBN heterostructure (with a bottom and top hBN multilayer of ~35 and ~38 nm thick) on a pre-patterned overall back-gate (BG) covered with a 20 nm thick Al_2O_3 and a split-gate (SG) on top of the heterostructure. The superconducting leads are edge connected to the mesa. The width $W = 3.2\,\mu$m and length $L = 950$ nm while the distance between the two fingers of the split-gate $w \sim 65$ nm (and $d' \sim 38$ nm and $d" \sim 55$ nm). **c,** AFM image of the device. Scale bar is 1 µm.

Supplementary Note 3.4.3, Supplementary Fig. 3.9, Supplementary Fig. 3.10 and Supplementary Fig. 3.11 for full analysis). Figure 3.2(a, b) display resistance maps as a function of split- and back-gate voltage measured in the normal and superconducting state respectively (*i.e.* at 20 mT and zero magnetic field). In both cases, distinct deviations from the expected quadrants formed in lateral npn-junctions corresponding to the differently doped regions [33–35] are clearly visible (unipolar and bipolar regions NNN, PPP and NPN, PNP respectively).

In BLG dual-gated devices, the displacement field is used to break the lattice inversion symmetry of the AB-stacked bilayer: the two layers being at different potentials a band gap opens [31, 32], inducing an insulating state with strongly suppressed conductivity. The resistance then raises monotonically with increasing displacement field as the band gap develops [33–35]. Here, we observe a non-monotonic change of the resistance which first increases and then drops after reaching a maximum while following the displacement field line (*i.e.* when the displacement field generated by the back- and split-gates, respectively D_b and D_t are equal, at $\delta D = D_b - D_t = 0$ [36]). In addition, the resistance peak does not follow the displacement field line which is indicated by the gray arrow as depicted in Fig. 3.2(a, b), but diverges into the bipolar regions (NPN and PNP). This trend is already noticeable in the normal state resistance (Fig. 3.2(a)), but becomes strikingly evident in the superconducting state (Fig. 3.2(b)). This unexpected behaviour can be understood as the competitive action of back- and split-gates within the constriction. As the displacement field increases, the charge carrier density mostly driven by the back-gate becomes less and less affected by the stray fields developed by the split-gate which cannot compensate the influence of the back-gate on the channel region. Instead of being maximum along the displacement field line [33–35] (marked as a diagonal arrowed line on the gate maps), the resistance increases up to a maximum then decreases as plotted in Fig. 3.2(d) for both normal and superconducting states. Consequently, the device remains highly conductive in contrast to the pinch-off characteristic of gapped BLG with full-width top-gate. Instead, the maximum resistance deviates from the displacement field line and “bends”. The bent line of the resistance peak results then from the required overcompensation of the split-gate voltage to diminish the induced charge carriers within the channel region. In the superconducting state, the resistance follows the same tend to finally drop to zero

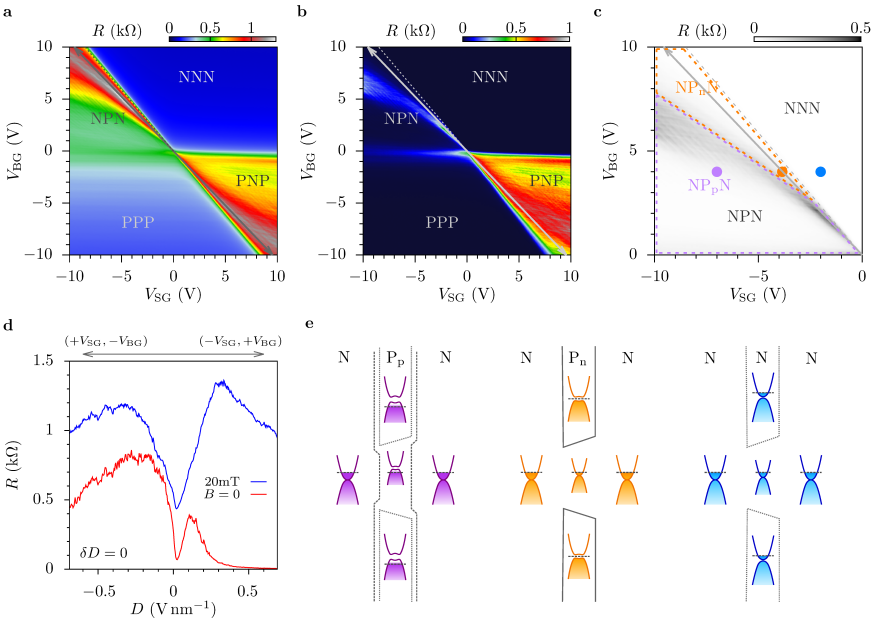

Figure 3.2: **Formation of the constriction: resistance gate map analysis. a,** Resistance map as a function of back- and split-gate voltage, V_{BG} and V_{SG} respectively, measured at ~ 25 mK in the normal state ($B = 20$ mT) with a maximum current of 2.6 nA. The arrow marks the displacement field line along which the charge carrier density in the dual-gated region is zero. The dashed line indicates the transition when E_F is tuned from the conduction band into the induced band gap, highlighting the crossover to a confined system. **b,** Resistance map versus V_{BG} and V_{SG} measured at ~ 25 mK in the superconducting state ($B = 0$) with a maximum current of 2.5 nA. **c,** Zoom-in on the upper left part of the resistance map in the superconducting state (**b**) where the different regime areas are enlightened. **d,** Normal (blue curve) and superconducting (red curve) state resistance measured along the displacement field line. **e,** Schematics of the spatially resolved energy band diagrams of our QPC geometry where top-views of the device refer to the three different regimes of panel **c**.

(Fig. 3.2(d)).

However, this imbalance between applied split- and back-gate voltages starts to induce charge carriers of opposite sign in the dual-gated cavities, resulting in pn-junctions. As a consequence, the bipolar regions become then subdivided into two parts depending on the doping in the constriction (denoted by a sub-label like NP_nN, see Fig. 3.2(c)). The QPC-like structure can then be driven in an "open" (the 1D channel doping is of the same type as the 2D reservoirs) or "closed" (the 1D channel doping is of opposite type as the reservoirs forming a non-uniform potential barrier) regime.

The schematics in Fig. 3.2(e) summarize the different scenarios which govern the behaviour of such an electrostatically induced constriction, *i.e.* the formed 1D constriction area NP_nN, the unipolar regime NNN and the non-uniform NP_pN junction. It is important to note that the overall resistance remains higher on the p-side (PPP and PNP) due to the slight n-doping provided by the leads which create a pn-junction at each contact. This becomes particularly clear in the superconducting state where the PNP region remains resistive while a large part of the NPN section displays a zero resistance state. For this reason, we focus on the NPN area and in particular on the NP_nN part where we can study the supercurrent flowing through the constriction.

3.2.2. SUPERCURRENT ANALYSIS

Now we describe how to control both supercurrent amplitude and spatial distribution using our split-gate geometry. We have seen in the previous section that our device becomes superconducting in the area where the constriction is formed, namely the NP_nN region. One way to verify our hypothesis consists of probing the critical current I_c which corresponds to the maximum supercurrent that a weak link can support before switching to a resistive state (see method section for a description of the critical current extraction procedure). I_c being extremely sensitive to any external perturbations such as magnetic field, potential landscape inhomogeneities or thermal excitation, drastic changes of the confinement should be clearly observed. Indeed, the variation of the normal state resistance is directly reflected in the supercurrent amplitude. For example, small oscillations in the resistance produced by Fabry-Pérot interferences are directly detected in the supercurrent [25, 26, 29, 37] (see Supplementary Fig. 3.11). Here, we focus our attention on the effect of the 1D constriction on the supercurrent amplitude.

The amplitude of the supercurrent can be monitored by tuning the charge carrier density with the overall back-gate voltage V_{BG}. In Fig. 3.3(a) the current-voltage characteristics are shown in the absence of a constriction, *i.e.* for a uniform 2D weak link at $V_{SG} = 0$. The supercurrent evolves from zero at the charge neutrality point up to a measured maximum of 1.86 µA at high charge carrier density $n \approx 4 \cdot 10^{12}\,\mathrm{cm}^{-2}$ (*i.e.* $V_{BG} = 10\,\mathrm{V}$). It is important to note that the *I*-*V* characteristics only display a rather limited hysteretic behaviour visible only at large charge carrier density corresponding to a weakly underdamped junction within the resistively and capacitively shunted junction (RCSJ) model [3]. When the Fermi level lies in the valence band ($V_{BG} < 0$), the weak link is disturbed by the presence of the pn-junctions which strongly suppresses the supercurrent by an order of magnitude (approximately 200 nA at $V_{BG} = -10\,\mathrm{V}$). This is clearly seen in Fig. 3.3(c) where the critical current I_c is plotted as a function of the back-gate voltage V_{BG} (supercurrent amplitude values are summarised in Supplementary Table 3.1; see also Supplementary Fig. 3.12 for

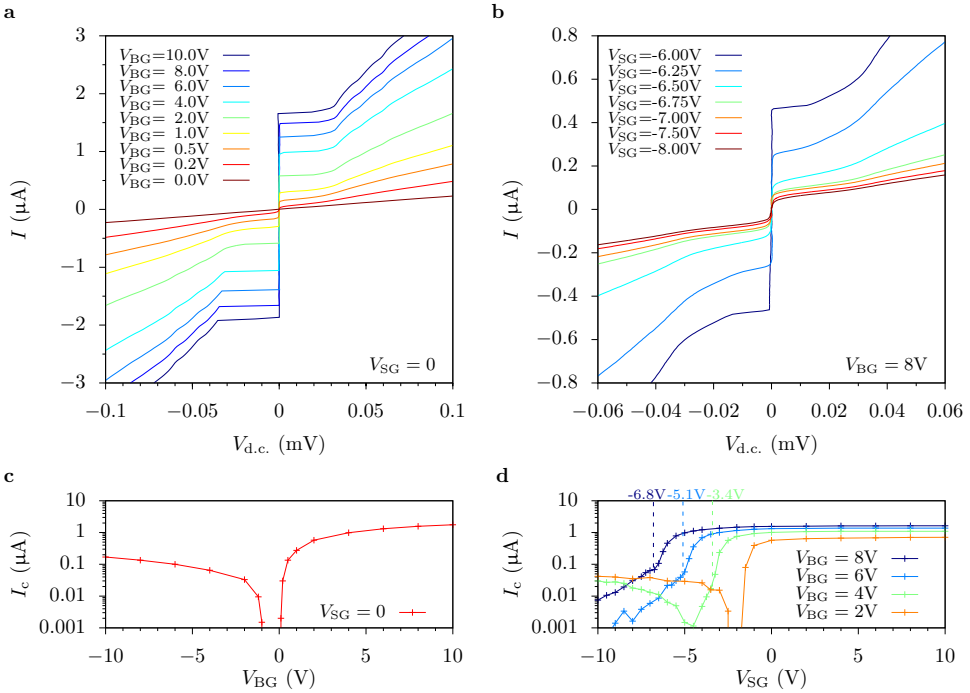

Figure 3.3: **Gate-controlled current in a superconducting BLG weak link. a,** *I-V* curves for different V_{BG}, *i.e.* densities, characterising the 2D system at $V_{SG} = 0$V. **b,** *I-V* curves at fixed back-gate voltage $V_{BG} = 8$V for various displacement fields D in the dual-gated region, *i.e.* for split-gate voltages close to the transition from NNN to NP_nN. **c,** Back-gate voltage dependence V_{BG} of the critical current I_c. **d,** $I_c(V_{SG})$ for constant charge carrier densities (*i.e.* constant V_{BG}).

negative back-gate voltage V_{BG}).

Figure 3.3(b) displays a series of *I-V* curves at fixed charge carrier density (here at $V_{BG} = 8$V) for different split-gate values in the vicinity of the NP_nN area. When approaching the formation of the constriction, I_c decreases rapidly until $V_{SG} \sim -6.65$V. At this point, the Fermi level underneath the split-gate is positioned in the gap. Therefore, charge carriers can only flow through the 1D constriction. Beyond the formation of the constriction, I_c decreases in a much slower fashion. The extracted critical current I_c is plotted in Fig. 3.3(d) as a function of the split-gate voltage V_{SG} at different densities. At small densities, *i.e.* $V_{BG} = 2$V (orange curve in Fig. 3.3(d)), the starting point of the NPN region appears early in gate voltage and the supercurrent is switched off. Then, the Fermi level in the constriction which remains mainly driven by the stray fields of the split-gate moves towards the valence band. Due to the close proximity of the split-gates, the stray fields are strong enough to close the channel. A small supercurrent can be detected despite the presence of a weak pn-junction as depicted in Fig. 3.2(d) (NP_pN area). In contrast, at higher densities the back-gate starts to electrostatically dominate the constriction region. The creation of the 1D channel is directly reflected in the sudden change of slope of $I_c(V_{SG})$ curves (blue and dark blue curves in Fig. 3.3(d), the change of slope being marked

by dotted lines). The supercurrent through the channel is then only slowly reduced with increasing split-gate voltage owing to the narrowing of the channel by the stray fields. Once the channel is created, the amplitude of the supercurrent drops way below 100 nA while multiple Andreev reflections completely vanish (see Supplementary Note 3.4.4 and Supplementary Fig. 3.12). At intermediate density (green curve in Fig. 3.3(d)), the channel is first created (rapid drop in $I_c(V_{SG})$ then change of slope marked by the dotted curve), then closed with the Fermi level positioned in the gap (supercurrent switched off), to finally form a non-uniform pn-junction as depicted in Fig. 3.2(e) (NP_pN area). We note that, on the presented device, we observe features visible in the normal and the superconducting state which could be related to quantized conductance and supercurrent (see Supplementary Note 3.4.5, Supplementary Figs. 3.13 and 3.14) as predicted for ballistic supercurrents in quantum point contacts [38–40].

3.2.3. MAGNETO-INTERFEROMETRY

The supercurrent density distribution across the sample width can be explored by probing its interference pattern [41] in response to a perpendicular magnetic flux penetrating the junction [5, 13, 27, 42–48]. Therefore, by changing the geometry of the system one can observe a large variety of interference patterns directly related to the supercurrent density distribution [5]. As recently shown [13, 27], superconducting interferometry is a powerful tool to probe confinement where the current density distribution can be extracted by complex Fourier transform following the approach of Dynes and Fulton [42]. However, this technique of recovering the supercurrent assumes that it is carried strictly in a direction normal to the superconducting electrodes, and therefore does not apply to our device because of the non-uniform supercurrent density in x-direction and its small aspect ratio in the QPC regime.

Here, we show that the magnetic interference pattern indicates clear signatures of the supercurrent confinement. Figure 3.4(a) exhibits a series of resistance maps versus current and magnetic field at constant density ($V_{BG} = 8\,V$). By increasing V_{SG}, *i.e.* the confinement, a progressive change of the interference pattern is observed as the split-gate is tuned and the 1D constriction forms. First, a beating pattern appears, resembling Fraunhofer-like interference (upper panel) when the system remains two-dimensional. Then the interference pattern turns to a "lifting lobes" shape just before the formation of the constriction (middle panel). Finally a non-beating "bell-shaped" pattern is formed while the supercurrent flows only through the confined 1D constriction (lower panel). We note that the transition from a beating to a non-beating pattern occurs on a rather narrow voltage range $-7\,V < V_{SG} < -6\,V$ (at $V_{BG} = 8\,V$, additional data at $V_{BG} = 4\,V$ are shown in Supplementary Note 3.4.6 and Supplementary Fig. 3.15). In Fig 3.4(b) we can observe a map of the critical current I_c (left panel) as well as the critical current normalized to the maximum critical current (at $B = 0$) $I_c^{norm.} = I_c / I_c(0)$ (right panel) as a function of magnetic field B and split-gate voltage V_{SG}, allowing a more accurate vision of the transition from 2D (beating pattern) to 1D ("bell-shaped" pattern). Each horizontal slice of such maps corresponds to the extracted critical current (or normalized critical current) of a single magnetic interference pattern (additional remarks and data can be seen in Supplementary Note 3.4.6 and Supplementary Fig. 3.15). We note that such non-beating pattern has been observed in rectangular superconducting weak links with low aspect

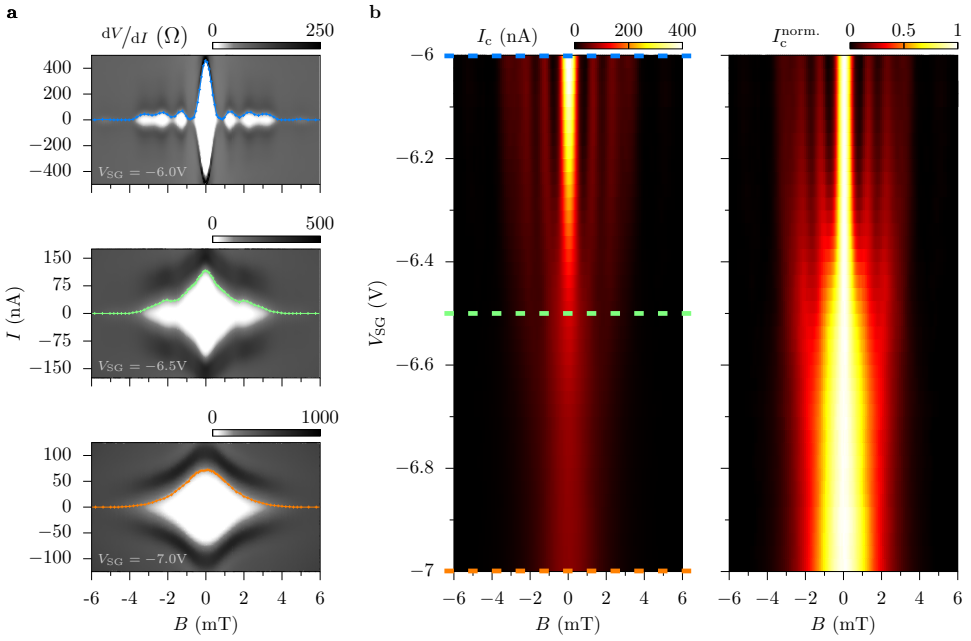

Figure 3.4: **Magnetic interferometry study of the transition from 2D to 1D confinement of the supercurrent. a,** Gray-scale map of the differential resistance $\mathrm{d}V/\mathrm{d}I$ versus magnetic field B and current I. The coloured dotted lines correspond to the extracted I_c. These measurements are taken at three different split-gate voltage values ($V_{SG} = -6\,V$, $-6.5\,V$ and $-7\,V$) at constant charge carrier density ($V_{BG} = 8\,V$). Drastic change in the interference pattern is observed highlighting a clear transition from 2D to 1D confined supercurrent. **b,** Critical current amplitude I_c (left panel) and normalised critical current amplitude $I_c^{norm.}$ (right panel) mapped as a function of magnetic field B and split-gate voltage V_{SG}. The transition from a beating pattern (Fraunhofer-like) to a monotonically decaying pattern is visible confirming the continuous change in the supercurrent confinement from 2D to 1D. The coloured dashed lines correspond to the split-gate values where the $\mathrm{d}V/\mathrm{d}I(V_{SG}, B)$ maps were measured in panels **a**.

ratio [46–48].

ANALYTICAL MODEL

In order to gain deeper understanding how the magnetic interferences should evolve with the creation of a 1D constriction into a 2D system, we have designed an analytical model where we calculate the Josephson current through the sample in the presence of a magnetic field B (see Supplementary Note 3.4.7, Supplementary Fig. 3.16 and Supplementary Fig. 3.17 for details), using a quasi-classical approach (as in [44, 49, 50]) with an additional input given by the presence of a QPC-like structure in the middle of the device (see the geometry used in Fig 3.5(a)). We have used our analytic expression to fit the maximum critical current as a function of magnetic field (see Fig 3.5(b)). The theoretical critical current (magenta curve) is matched to the experimental data $I_c(B)$ (turquoise crosses) by scaling the curve by a factor of the extracted maximum critical current $I_c(0) = 43.5\,nA$ using a junction area of $\sim 6.08 \cdot 10^{-12}\,m^2$ with a total junction length of $\tilde{L} = L + 2\lambda_L = 1.90\,\mu m$ where λ_L is the London penetration depth ($\lambda_L \sim 450\,nm$).

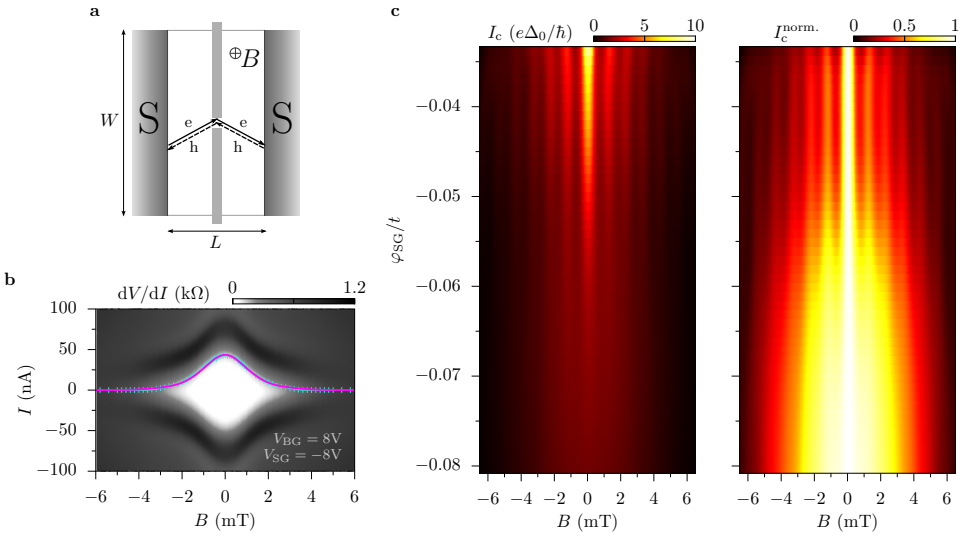

Figure 3.5: **Modelling supercurrent confinement. a,** Schematic of the superconducting weak link with a quantum point contact like geometry used for our analytical model. **b,** Differential resistance $\mathrm{d}V/\mathrm{d}I$ versus magnetic field B and current I including the extracted critical current I_c (turquoise crosses) fitted with our analytical model (magenta line) when the 1D constriction is formed (at $V_{BG} = 8\,V$ and $V_{SG} = -8\,V$). **c,** Numerical simulations of critical current amplitude I_c (left panel) and normalized critical current amplitude $I_c^{norm.}$ (right panel) mapped as a function of magnetic field B and split-gate strength φ_{SG} showing the transition from 2D to 1D of the magnetic interferences. The x-axis is rescaled to magnetic field B using the parameters extracted by fitting the numerical simulation to the experimental data at V_{SG}=0 (see Supplementary Note 3.4.7, Supplementary Fig. 3.16, and Supplementary Fig. 3.17 for details).

Our model follows clearly the experimental data $I_c(B)$ which, once again, proves that the supercurrent has been strongly confined in our quantum point contact edge connected BLG.

NUMERICAL MODEL: SHORT JUNCTION

We also performed tight-binding simulations using Kwant package [51]. We model a superconductor–bilayer-graphene–superconductor (SBLGS) Josephson junction (JJ) in the presence of top split gates in the experimental geometry. We used the actual device image in Fig. 3.1(c) and converted it into a bilayer graphene mesh as shown in Fig. 3.6. We investigate the orbital effects of the magnetic field which is applied perpendicular (say in z-direction) to the junction in the normal region. For numerical simulations, we use a Landau gauge such that the vector potential is given by $\mathbf{A} = (-By\hat{x}, 0, 0)$.

The tight-binding Hamiltonian for the normal scattering region can be written as:

$$H = -t\sum_{i,j,m} e^{\iota\phi_{ij}} a^\dagger_{mi} b_{mj} - \gamma_1 \sum_j a^\dagger_{1j} b_{2j} - \sum_{i,m} (\mu_i - (-1)^m \delta_i)(a^\dagger_{mi} a_{mi} + b^\dagger_{mi} b_{mi}) + H.c., \quad (3.1)$$

with the magnetic phases $\phi_{i,j} = \frac{2\pi e}{h}\int_i^j \mathbf{A}\cdot\mathrm{d}\mathbf{r}$. The indices i, j corresponds to the lattice sites, whereas $m = 1, 2$ denote the two layers of the BLG. The operators $a_{mi}, a^\dagger_{mi}$ ($b_{mi}, b^\dagger_{mi}$) are the annihilation and creation operators for electrons at site i in sublattice A_m (B_m),

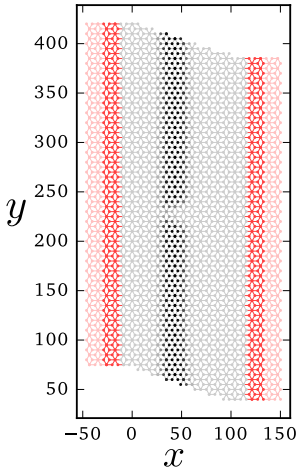

Figure 3.6: **Illustration of the setup used for the simulations.** The darker region represents the QPC area while the red strips represent the leads attached to the scattering region. The scales of the x- and y-axis are defined in terms of the tight-binding lattice constant.

respectively. The parameters t and γ_1 are the intralayer and interlayer (between dimer sites) hopping constants, respectively, whereas μ and δ correspond to the onsite energies given by

$$\mu_i = (\varphi_{\mathrm{BG}} + u_{\mathrm{i}}\varphi_{\mathrm{SG}})/2, \tag{3.2}$$

and

$$\delta_i = -(u_i\varphi_{\mathrm{SG}} - \varphi_{\mathrm{BG}})/\eta. \tag{3.3}$$

Here u_i defines the gated region such that:

$$u_i = \begin{cases} 1 & \text{if } i \text{ is inside gated region} \\ 0 & \text{if } i \text{ is outside gated region} \end{cases} \tag{3.4}$$

and η is the numerical factor accounting for the geometry of the setup in the direction perpendicular to the graphene plane. In what follows, we choose $\eta = 2.5$.

In the above equations, φ_{BG} and φ_{SG} represent the strengths of the on-site potentials introduced by the back gate and top split gate, respectively. The corresponding Bogoliubov-De Gennes Hamiltonian for the SBLGS junction reads:

$$H_{\mathrm{BdG}} = \begin{pmatrix} H & \Delta \\ \Delta^* & -H^* \end{pmatrix}, \tag{3.5}$$

where Δ is a step-like function given by

$$\Delta = \begin{cases} \Delta_0 e^{i\chi_1} & \text{left lead} \\ \Delta_0 e^{i\chi_2} & \text{right lead} \\ 0 & \text{scattering region} \end{cases}, \tag{3.6}$$

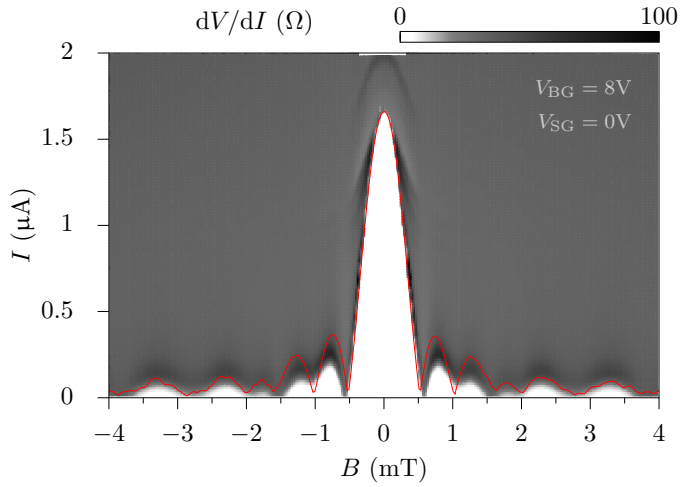

Figure 3.7: **Magneto-interference pattern of the 2D system.** Fit (red curve) of experimental magnetic interference pattern $\mathrm{d}V/\mathrm{d}I(B, I)$ at zero split-gate voltage and $V_{\mathrm{BG}} = 8\,\mathrm{V}$ (grey-scale map).

with $\chi_i(\chi_2)$ the superconducting phase of left (right) lead such that the corresponding superconducting phase difference is $\chi = \chi_1 - \chi_2$.

To calculate the supercurrent, we use Eq. (2.20) derived in chapter 2 which gives the derivative of Andreev bound state energy as a function of the superconducting phase difference:

$$\frac{d\epsilon}{d\chi} = \frac{\Delta^2}{2}\frac{1}{\epsilon}\left\langle \Psi^e_{\mathrm{in}} \left| \frac{d(A^\dagger A)}{d\chi} \right| \Psi^e_{\mathrm{in}} \right\rangle. \tag{3.7}$$

The supercurrent is then given by Eq. (2.21):

$$J(\chi) = -\frac{2e}{\hbar}\sum_p \tanh(\epsilon_p/2k_{\mathrm{B}}\mathcal{T})\frac{\mathrm{d}\epsilon_p}{\mathrm{d}\chi}. \tag{3.8}$$

To calculate the quantity in Eq. (3.7), we use Kwant [51] where we discretise Eq. (3.1) on a honeycomb lattice Fig. 3.6. We show the numerically calculated critical current I_{c} as a function of magnetic field B and split-gate strength φ_{SG} (in units of the intralayer hopping constant t) in Fig 3.5(c). The simulation results are in good qualitative agreement with our experimental data of Fig 3.4(b). For simulations, we take the parametersc $\varphi_{\mathrm{BG}} = 0.2t$, $\gamma_1 = 0.4t$ and vary φ_{SG} starting from the "open" regime (ungapped BLG in gated region) to the "closed" regime (gapped BLG in the gated region). The numerical calculations are performed in the short-junction limit and at finite temperature $k_{\mathrm{B}}\mathcal{T} = \Delta_0/20$. The fitting is done by rescaling both axes to match the experimental plot using a junction area of $\sim 4.60 \cdot 10^{-12}\,\mathrm{m}^2$ (corresponding to $\lambda_{\mathrm{L}} = 245\,\mathrm{nm}$).

We note that the experimental magnetic interference pattern at zero split-gate voltage is quite distorted with some missing/suppressed lobs as compared to a $sinc$ function of a regular, short and wide rectangular junction [3]. We fit this data at zero split-gate voltage with the simulation data at a finite but small top-gate strength ($\varphi_{\mathrm{SG}}/t = -0.024$)

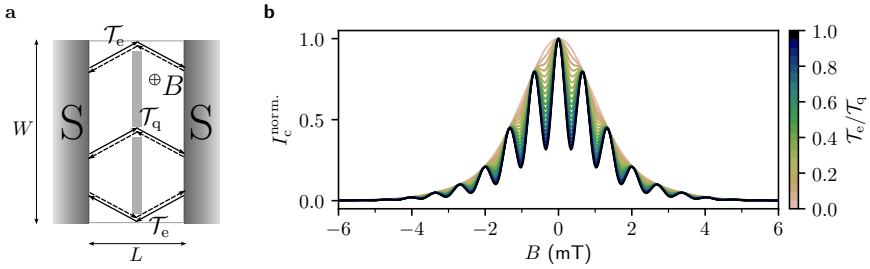

Figure 3.8: **Effect of the edge currents on the interferometric pattern. a,** Schematic of the superconducting weak link with a quantum point contact like geometry including possibility of edge currents used for our analytical model. **b,** Calculated $I_c^{norm.}$ versus magnetic field B for different values of the transmission coefficient ratio $\mathcal{T}_e/\mathcal{T}_q$.

showing excellent match Fig. 3.7, which may indicate the presence of a small but non-zero potential in the gated region in our experiments. This potential can result from the charge redistribution in the metallic top-gate which is induced by the electrostatic interaction between electrons in the gate and in bilayer graphene.

EDGE EFFECTS

Finally, from the magneto-interferometry experiments, no obvious signs of induced current through topological channels appearing due to AB stacking faults [52] or edge states [27, 53, 54] have been detected. In order to verify this assumption, we have estimated what would be the effect of additional current flowing at the edges (with a transmission $\mathcal{T}_e$) while the current is confined by the QPC (with a transmission $\mathcal{T}_q$) as depicted in Fig. 3.8(a). Our analytical model (see Supplementary Note 3.4.8 and Supplementary Fig. 3.18 for details) shows that the presence of edge states develops a beating on top of the pattern formed by the 1D confinement. When we look at the expected magneto-interferometric pattern as displayed in Fig. 3.8(b), we clearly see the effect of the additional current which modulates periodically with magnetic field B the amplitude of $I_c^{norm.}$. The modulation becomes visible for $\mathcal{T}_e \sim \mathcal{T}_q/100$. In absence of edge states, $\mathcal{T}_e = 0$, we recover our previous result shown in see Fig 3.5(b). Thus, it is clear that if one would be confronted to the presence of current flowing through the edges (or any other current path) in our QPC geometry, the magneto-interferometric pattern should be directly affected for, at least, current values down to a hundredth of the current through the constriction. Here, we have measured a confined supercurrent down to ~ 20 nA. Therefore, one should be able to detect the presence of edge currents down to 200 pA or less, (*i.e.* 25 times less than measured in [53]).

At back- and split-gate values of $V_{BG} = 8\,V$ and $V_{SG} = -7.6\,V$ respectively, the induced displacement field of $D \approx 0.56\,V/nm$ (one order of magnitude larger than in [53]) opens a significantly large band gap $E_g \approx 85.4\,meV$ (for the gap extraction see Supplementary Note 3.4.2) and no edge current is detected by mangeto-interferometry. The absence of edge contribution to the total current could be explained by the edge-state localisation in the case of large band gap as reported in [55]. The characteristic value of the localisation length was found to be about tens of nanometers, which is much smaller than the top-gated region in our experiment, thus implying strong suppression of edge currents.

On the basis of our model, the presence of conducting edge channels should be detectable within our experimental conditions. However, the relatively large band gap may cause the suppression of the edge currents which could be the reason why we do not observe their presence in our measurements.

3.3. DISCUSSION

In this work, we have demonstrated a full monitoring, both spatially and in amplitude, of the supercurrent in a clean and edge connected hBN-BLG-hBN heterostructure. In a split-gate geometry we have explored the consequences of the 1D confinement on the supercurrent and on its magnetic interferences. Thanks to in turn, the possibility to locally engineer an electronic band gap in BLG, the injection of a large and fully controllable critical current, the ultra-low disorder of encapsulated hBN-BLG-hBN heterostructures and the absence of edge currents, we have designed a unique platform allowing the creation of new types of superconducting circuits based on fully tunable weak links which can be controlled by the combination of top- and back-gates.

3.3.1. METHOD SUBSECTION.

Experimental: The low-temperature electrical measurements were performed in a Bluefors LD250 ^{3}He/^{4}He dilution fridge at a base temperature of ~25 mK. All dc-lines were strongly filtered using 3-stage RC-filters with a cut-off frequency of 1 kHz, as well as PCB-powder filters with a cut-off frequency of about 1 GHz. The differential resistance/conductance data was measured using standard low-frequency (~13 Hz) and various low excitation (between 1 and 10 μV), the gating and the out-of-equilibrium measurements were performed using ultra-low noise dc-power supply from Itest. The normal state was obtained by applying a perpendicular magnetic field of 20 mT. The experiments were performed within several thermal cycles (room temperature ⇌ milli-Kelvin temperature). Data have been reproduced and implemented in each cooldown.

Data treatment and I_c extraction: The critical current I_c is extracted using a voltage threshold method, where the threshold is set to 1 μV. The two adjacent data points of recorded IVs right before and after the threshold are evaluated and I_c is determined by linear extrapolation in the current of these two points depending on the difference of the voltage drop with respect to the threshold. The extracted critical current is corrected by subtracting the artificial offset that is produced by this method.

3.4. SUPPLEMENTARY INFORMATION

3.4.1. SUPPLEMENTARY NOTE 1: DEVICE FABRICATION

The edge connected van der Waals heterostructures based on hBN-bilayer graphene-hBN are prepared following the method developed by Wang *et al.* [24]. Bilayer graphene (BLG) flakes and hexagonal boron nitride multilayers (bottom and top hBN multilayer are ~ 35 nm and ~ 38 nm thick respectively) are obtained by mechanical exfoliation from natural bulk graphite (NGS Naturgraphit GmbH) and commercial hBN powder (Momentive, grade PT110) respectively and transferred on p-doped Si substrates with 300 nm thick thermally grown SiO_2 layer and selected by optical contrast [56]. Raman spectroscopy was used to unambiguously identify BLG [57] (Renishaw inVia Raman spectrometer, using a laser

of wave length $\lambda = 532\,\text{nm}$). The graphene was then encapsulated between a top and a bottom hBN flake by piling up the layers sequentially by using a polymer-free assembly technique [24] and a home-made transfer set-up. Then, the whole stack was transferred onto a sapphire substrate with a Cr/Au (5 nm/50 nm) pre-patterned back-gate which is covered by a dielectric of 20 nm Al_2O_3 deposited by atomic layer deposition [58] (182 cycles at 200 °C). Edge contacts are designed on the mesa and defined by electron beam lithography using a single resist layer of PMMA covered by conductive polymers (Espacer 300Z from Showa Denko K.K., see [59]) for both etching and subsequent metallisation. The conductive polymer insures good evacuation of charges allowing e-beam lithography on a fully insulating substrate such as sapphire. Unlike in [24], only PMMA was used as a mask (~ 250 nm). The hBN-BLG-hBN sandwich was then etched in an Oxford Instruments Plasmalab 80 reactor with a mixture of CHF_3 and O_2 forming a 60 W plasma (40 sccm CHF_3 with 4 sccm O_2 at a pressure of 60 mTorr; etching rate: 23 and 48 nm/min for PMMA and hBN respectively). A double layer of titanium/aluminium (5 nm/80 nm) electrodes were then deposited by molecular beam epitaxy (at pressure and sample temperature $\sim 10^{-10}$ mTorr and ~ −130 °C respectively) using the same already patterned PMMA resist, followed by lift-off in acetone. In a subsequent step, split-gates are fabricated in the similar fashion, *i.e.* e-beam lithography followed by metallisation (a Ti/Al double layer of 5 nm and 80 nm thickness respectively). It is important to note that the width of the split-gates (~ 300 nm) does not exceed two times the London penetration depth ($\lambda_L > 200\,\text{nm}$ in aluminium thin films according to [60]) so that the applied magnetic field is not disturbed by the split-gate electrodes becoming superconducting at very low temperature. Finally, the devices are shaped into the desired geometry by a third lithography step and subsequent etching using the parameters of the previous etch process. The distance between the two fingers of the split-gate is $w \sim 65\,\text{nm}$.

3.4.2. SUPPLEMENTARY NOTE 2: NORMAL STATE CHARACTERIZATION

Supplementary Figure 3.9(a) shows both normal state resistance R and conductance G as a function of back-gate voltage V_{BG} and charge carrier density n, while Supplementary Figure 3.9(b) displays the electron conductivity (minus the estimated contact resistance calculated below) *vs* charge carrier density.

The contact resistance per contact is estimated as $R_C = (R - R_Q)/2$, where the quantum resistance R_Q is subtracted from the measured resistance R. The quantum resistance $R_Q = \frac{h}{ge^2}\frac{1}{M}$ is defined as the resistance set by the ballistic limit of all contributing conductance modes $M = \frac{W}{\lambda_F/2}$, where $\lambda_F = 2\pi/k_F = 2\pi/\sqrt{\pi n}$ is the Fermi wavelength at charge carrier density n and $g = 4$ accounts for the spin and valley degeneracy. At high charge carrier density $n \approx 4 \cdot 10^{12}\,\text{cm}^{-2}$ ($M = 361$ and $R_Q = 18\,\Omega$) a resistance of $R = 90\,\Omega$ is measured, yielding the contact resistance $R_C = 36\,\Omega$ and contact resistivity $\rho_C = R_C W = 115\,\Omega\mu\text{m}$, comparable to the values given by Wang *et al.* [24].

We estimate the residual density of $n_{res} \approx 2.6 \cdot 10^{10}\,\text{cm}^{-2}$ as to [17] on the electron side (see Supplementary Figure 3.9(a)). Supplementary Figure 3.10(a) displays a grey-scale map of the two-terminal conductance $G(B, V_{BG})$ (upper panel) and $G(V_{BG})$ curves for various B (lower panel). The two-terminal differentiated conductance dG/dV_{BG} map as a function of the magnetic field B and the back-gate voltage V_{BG} is shown in Supplementary Figure 3.10(b). The two-terminal quantum Hall conductance curves display distorted

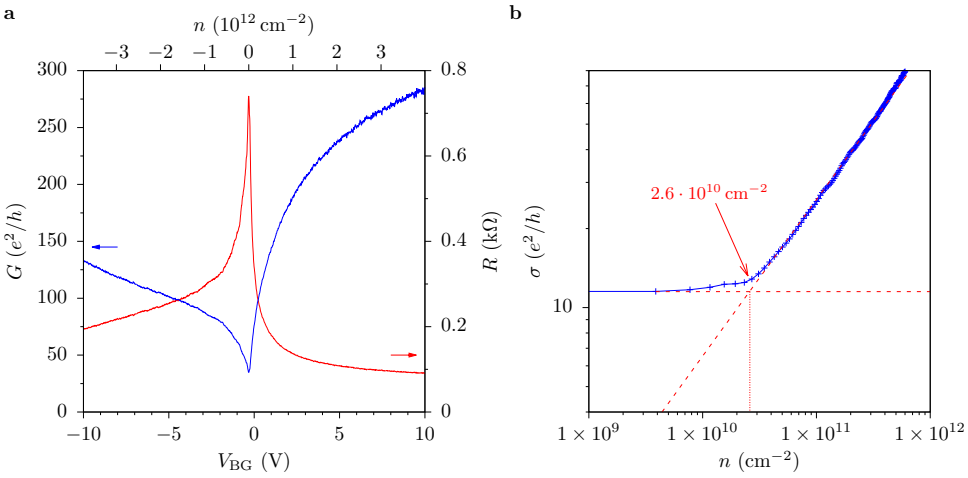

Figure 3.9: **Normal state characterisation. a,** Resistance R (red curve) and conductance G (blue curve) as a function of the back-gate voltage V_{BG} (lower abscissa) or converted charge carrier density n (upper abscissa) of the 2D system respectively. The curve was measured in a separate cooldown at a split-gate voltage $V_{SG} = V_{SG}^{(0)} = 0.2$ V. **b,** log-log-plot of the conductivity σ as a function of n. A contact resistance of $2R_C = 72\,\Omega$ was subtracted. The crossing of the saturation conductivity with the extrapolated linear fit to the data at high charge carrier density yields a residual charge inhomogeneity of the order of 10^{10} cm^{-2}. It is important to note that clear Fabry-Pérot resonances (see Fig. 3.2 of the main text and Supplementary Fig. 3.11) are visible in all cavities formed by the split-gate or by the unintentional doping from the leads, indicating ballistic transport across the device.

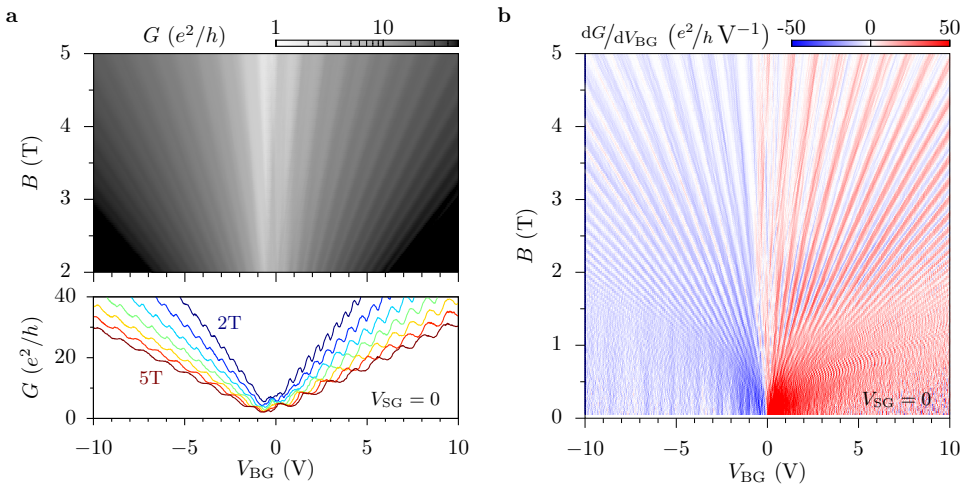

Figure 3.10: **Two-terminal magnetotransport of the 2D bilayer graphene.** Landau fan diagram of, **a,** the two-terminal conductance $G(B, V_{BG})$ and **b,** the two-terminal differentiated conductance $\mathrm{d}G/\mathrm{d}V_{BG}(B, V_{BG})$ as a function of the magnetic field B and the back-gate voltage V_{BG}, measured at a temperature ~ 25 mK.

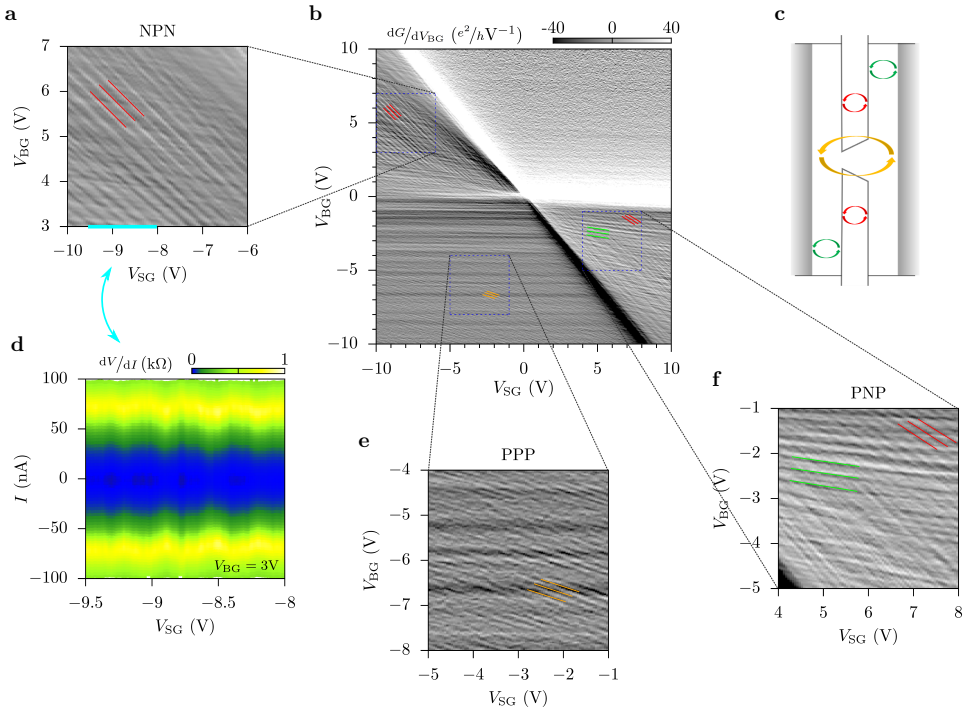

Figure 3.11: **Fabry-Pérot resonances. b,** Differentiated conductance dG/dV_{BG} as a function of back- and split-gate voltage (V_{BG}, V_{SG}) measured at 20 mT (normal state). Fabry-Pérot resonances can be observed in the parts of the map where cavities are formed by pn-junctions. **a, e, f,** Zoom-in on the NPN, PNP and PPP region of the gate map. The visible resonances are highlighted by exemplary lines and schematically represented on panel **c,** where the device can be divided into the corresponding cavities. **d**, differential resistance dV/dI *vs* current bias I and split-gate voltage V_{SG} measured along the cyan line of panel **a**. Oscillations of the supercurrent due to the Fabry-Pérot interferences are visible.

conductance plateaus as expected for high aspect ratio W/L sample geometry [61–65]. One can observe a well developed Landau fan even at relatively low magnetic field, highlighting the high quality of our device.

We provide quantitative estimation of the gap induced by the displacement field that break the lattice symmetry underneath the split-gate using the formula provided in [31, 32]. The gap should be larger than the potential fluctuation coming from the residual charge carrier inhomogeneity $n_{res} \approx 2.6 \cdot 10^{10}\,cm^{-2}$ which corresponds to an excitation of $E \approx 1$ meV (a band gap of 1 meV can be obtained by applying back and top gate values of for example $V_{BG} = 0.14$ V and $V_{SG} = -0.13$ V respectively). At back and split gate values of $V_{BG} = 8$ V and $V_{SG} = -7.6$ V respectively, which corresponds to a displacement field of $D \approx 0.56$ V/nm following Zhang *et al.* [36], we obtain an energy band gap of $E_g \approx 85.4$ meV, *i.e.* a value much larger than the potential fluctuation.

3.4.3. SUPPLEMENTARY NOTE 3: FABRY-PÉROT INTERFERENCE ANALYSIS

The gate dependence of the conductance reveals multiple oscillation patterns that can be attributed to Fabry-Pérot interferences of different cavities [35, 66–68]. Supplementary Figure 3.11 shows dG/dV_{BG} as a function of back- and split-gate voltage (V_{BG}, V_{SG}), where the data of the conductance G is numerically differentiated with respect to V_{BG}. Taking into account the size of the cavity and the gate dependence of the interferences, *i.e.* slope and appearance in the gate map, the observed patterns can be unambiguously assigned to the corresponding cavities (see Supplementary Figure 3.11(a, c, e, f)). The effective cavity length L can be determined by the relation $\Delta n = 2\sqrt{\pi n}/L$ which follows from the resonance condition $\Delta k \cdot L = \pi$.

In the unipolar regime PPP, pn-junctions arise at the interface of the graphene sheet with the two metallic electrodes. Thus, a cavity is formed between the two outer contacts. At a density $n \approx 2 \cdot 10^{12}\,\mathrm{cm}^{-2}$ ($V_{SG} = 0$) the spacing between interference peaks is $\Delta n \approx 5 \cdot 10^{10}\,\mathrm{cm}^{-2}$. By using $\Delta n = 2\sqrt{\pi n}/L$, we find an effective cavity length of $L \approx 1\,\mu\mathrm{m}$ which is consistent with the geometrical size of the device. Therefore, we can conclude that such Fabry-Pérot interferences indicate ballistic transport on a length scale of at least twice the device length, *i.e.* $\approx 2\,\mu\mathrm{m}$.

3.4.4. SUPPLEMENTARY NOTE 4: SUPERCURRENT AND MULTIPLE ANDREEV REFLECTION

Here, we provide additional information on the superconducting properties of our sample. As we have seen, the magnitude of the supercurrent is back-gate tunable, *i.e.* depends on the charge carrier density. While at the charge neutrality point superconductivity is fully suppressed, large supercurrent densities of $\sim 580\,\mathrm{nA\,\mu m}^{-1}$ at $n \approx 4 \cdot 10^{12}\,\mathrm{cm}^{-2}$ are measured. Furthermore, the supercurrent amplitude is dramatically reduced by the two pn-junctions formed at bilayer graphene-metal contact interfaces when the back-gate tunes the Fermi level in the valence band ($V_{BG} < 0$) (*i.e.* the PPP and PNP regions). The current-voltage characteristics extracted from the PPP region show a strong attenuation (by approximately one order of magnitude) compared to the NNN part where no pn-junction is formed (see Supplementary Figure 3.12(a)). The product of the critical current and the normal state resistance $I_c R_n$ as a function of the back-gate voltage V_{BG} at $V_{SG} = 0$ (in blue) and $I_c R_n$ as a function of the split-gate voltage V_{SG} at $V_{BG} = 8\,\mathrm{V}$ (in red) are displayed in Supplementary Figure 3.12(b). In the absence of voltage applied on the split-gate, a clear asymmetry between hole and electron conduction is visible in the bipolar supercurrent amplitude reflecting the presence of the two pn-junctions formed at the contacts. When the split-gate voltage increases, the $I_c R_n$ product remains stable until the constriction starts to form. Then, the $I_c R_n$ product decreases rapidly. We note that contrary to $I_c(V_{SG})$ which decays monotonically, the $I_c R_n$ product suddenly increases slightly between 6 V and 7 V corresponding to the voltage range of the 2D to 1D transition, before decreasing again as the constriction size shrinks.

The impact of the constriction on the hysteretic behaviour of the Josephson effect is shown in Supplementary Figure 3.12(c). As we can see on the *I-V* curves (up and back bias sweeps), the hysteresis occurs at sufficiently high charge carrier density and disappears once the constriction develops. Supplementary Table 3.1 recapitulates the extracted I_c, the retrapping current I_r and the ratio I_r/I_c in the various regions of the gate map (see

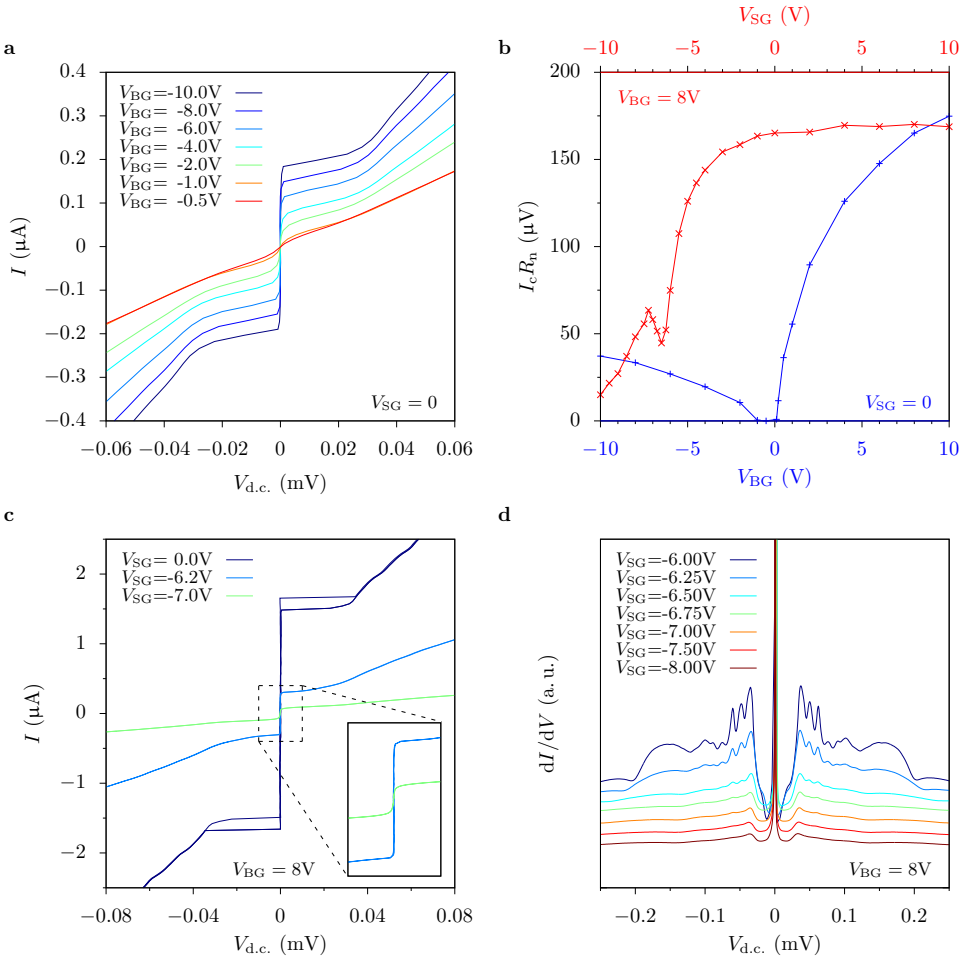

Figure 3.12: ***I-V* curves, $I_c R_n$ product and multiple Andreev reflection. a,** Series of *I-V* curves in the p-doped region at $V_{SG} = 0$. **b,** $I_c R_n$ versus V_{BG} at $V_{SG} = 0$ (in blue) and $I_c R_n$ versus V_{SG} at $V_{BG} = 8\,V$ (in red). **c,** The *I-V* curves show the behaviour for the three different cases: no split-gate ($V_{SG} = 0$), right before ($V_{SG} = -6.2\,V$) and once the constriction is fully developed ($V_{SG} = -7\,V$), at $V_{BG} = 8\,V$. A zoom-in of the two curves taken at $V_{SG} = -6.2\,V$ and $-7\,V$ is displayed in the inset, highlighting the absence of hysteresis before and after the formation of the constriction. **d,** Series of differential conductance dI/dV *vs* voltage V_{DC} for various split-gate voltages V_{SG} at $V_{BG} = 8\,V$. The curves are shifted for clarity. MAR clearly vanishes with the creation of the 1D constriction.

	V_{SG}(V)	V_{BG}(V)	n(cm^{-2})	I_c(μA)	I_r(μA)	I_r/I_c	I_cR_n(μV)
NNN	0	10	$\sim 4\times10^{12}$	1.86	1.66	0.9	174.8
	0	8	$\sim 3.2\times10^{12}$	1.66	1.48	0.9	165.1
	0	6	$\sim 2.4\times10^{12}$	1.38	1.25	0.9	147.7
	0	4	$\sim 1.6\times10^{12}$	1.05	0.95	0.9	126
	0	2	$\sim 0.8\times10^{12}$	0.585	0.585	1	89.5
PPP	0	-10	$\sim -4\times10^{12}$	0.185	0.185	1	37.2
	0	-8	$\sim -3.2\times10^{12}$	0.152	0.152	1	33.4
NNN	-6.2	8	$\sim 3.2\times10^{12}$	0.295	0.295	1	56.3
NP_nN	-7	8	$\sim 3.2\times10^{12}$	0.071	0.071	1	58.1

Table 3.1: **Compilation of some of the superconducting characteristics**. Critical current I_c, the retrapping current I_r, I_r/I_c and I_cR_n product under several gate conditions corresponding to different regions of the gate map (see Fig. 3.2 of the main text).

Fig. 3.2 of the main text). Within the RCSJ model [3], the Josephson junction is tuned from underdamped to overdamped. We note that for small n-doping, *i.e.* $n < 1.5\cdot10^{12}$ cm^{-2}, as well as for p-doping no hysteresis is detected.

Supplementary Figure 3.12(d) exhibits the effect of the constriction on multiple Andreev reflection (MAR). MAR appears as peaks in the differential conductance dI/dV versus bias voltage V_{DC} and are positioned at $2\Delta/en$ (with $n = 1,2,3,4,...$ and Δ being the superconducting gap, here estimated at $\sim$ 100μeV). When the constriction is formed, these subgap features disappear while a finite supercurrent remains detectable. The constriction limits dramatically the possibilities for the reflected quasi-particles to return to the opposite lead, and therefore vanishes the MAR. It is important to note that the disappearance of MAR coincides with the reduction of the supercurrent amplitude and the change in the magneto-interferometric pattern (see Fig. 3.3(d) and 3.4 in the main text).

3.4.5. SUPPLEMENTARY NOTE 5: ANY SIGNS OF QUANTIZED SUPERCURRENT?

In our experiments, we clearly observe Fabry-Pérot interferences highlighting ballistic transport of the charge carriers all across the length of the device. Therefore, one might expect to observe quantized conductance while inducing a constriction in a two-dimensional system [69, 70]. This phenomenon has been extensively studied in particular

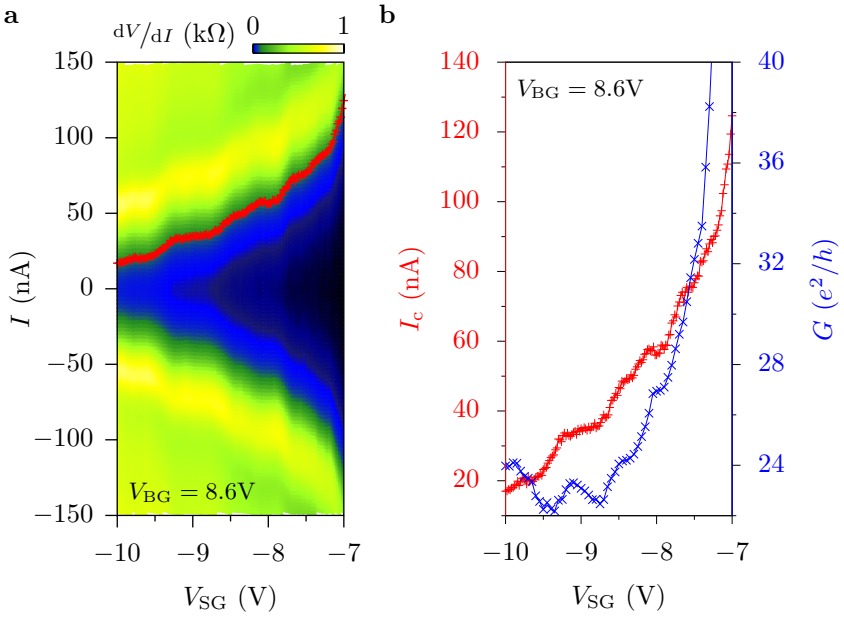

Figure 3.13: **Step-like features in the supercurrent and in the normal state conductance**. **a,** Differential resistance $dV/dI(V_{SG}, I)$ map as a function of split-gate voltage V_{SG} and current I zoomed-in on the NP_nN region, revealing a step-wise reduction of the critical current I_c (red curve). **b,** Critical current I_c (red) and normal state conductance G (blue) *vs* V_{SG} at $V_{BG} = 8.6$ V.

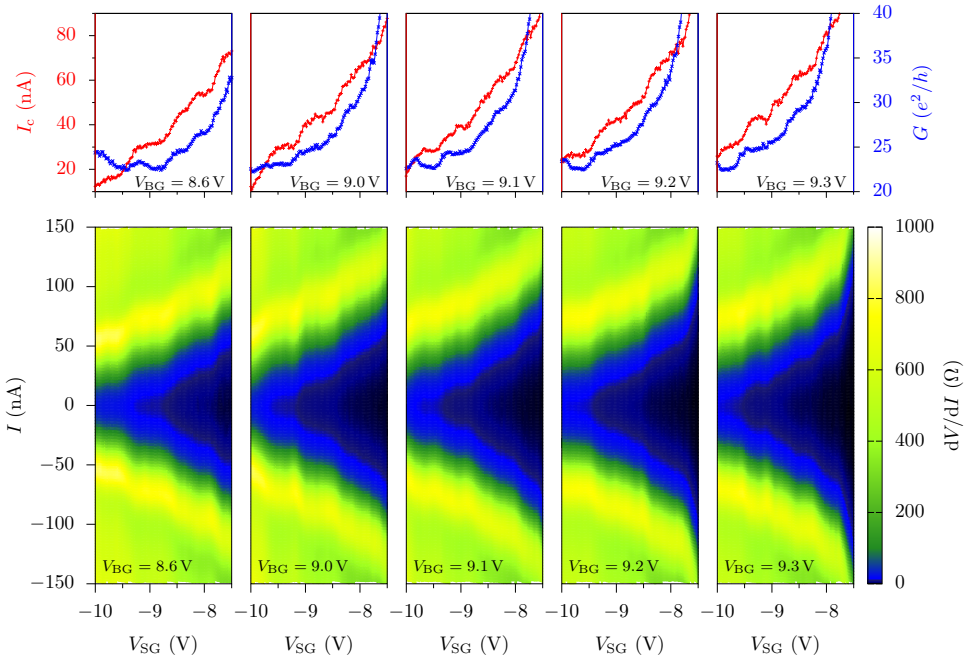

Figure 3.14: **Step-like features in the supercurrent under various back-gate conditions**. Critical current I_c and conductance G (top) and differential resistance $dV/dI(V_{SG}, I)$ maps (bottom) showing step-like features in the supercurrent for various back-gate voltages, from left to right $V_{BG} = 8.6, 9.0, 9.1, 9.2$ and 9.3 V respectively.

in AlGaAs/GaAs heterostructures [71]. Until now, step-like-features in the conductance have been observed in graphene (both single and bilayers) but none of them quantized in the expected value of $4e^2/h$ [72–81] (the prefactor 4 refers to the spin and valley degeneracy). For our configuration using only one overall back-gate and a local split-gate, both the tuning of the Fermi energy and the opening of the gap cannot be fully independently controlled within the 1D constriction. At V_{BG} and V_{SG} sufficiently large to form the constriction and confine the supercurrent, the charge carrier density within the constriction (mostly influenced by the back-gate compared to the stray field generated by the split-gate) might appear too large and the confinement not strong enough to clearly form 1D subbands and therefore both quantized conductance and supercurrent appear to be hard to observe. Therefore the picture drawn for more conventional semiconductors might not be applicable [38–40]. In our case we observe features in the normal and superconducting state conductance although non-quantized, here at $V_{BG} = 8.6\,\text{V}$ (see Supplementary Figure 3.13). At this back gate value the NP_nN and NP_pN border corresponds to $V_{SG} \sim -8.5\,\text{V}$. As we can see, the minimum conductance reaches $24e^2/h$ corresponding to 6, four times degenerated, opened channels and a resistance of $\sim 1\,\text{k}\Omega$. We note that these features are observable in a large back-gate range (see Supplementary Figure 3.14). What we define as signs of quantized supercurrent (together with signs of quantized conductance) was measured in our shorter device with $w \sim 65\,\text{nm}$ split-gate distance but not in our longer device with a wider constriction ($w \sim 150\,\text{nm}$ split-gate distance, not shown here) which showed all properties of confinement (in both amplitude and magneto-interferometric pattern) that we present in this work.

3.4.6. SUPPLEMENTARY NOTE 6: MAGNETIC INTERFERENCE PATTERNS AT $V_{BG} = 4\,\text{V}$

Here we show an additional series of data where the change of the magnetic interferences clearly shows a transition from a beating to a non-beating pattern corresponding to the creation of the 1D constriction. Supplementary Figure 3.15(a) displays a series of resistance maps versus current and magnetic field at constant density ($V_{BG} = 4\,\text{V}$) in a similar fashion as the data taken at higher density presented in the main text. Here, the transition from a beating to a non-beating pattern occurs in a voltage range -3 V < V_{SG} < -3.5 V. In Supplementary Figure 3.15(b), we see the two coloured maps of the critical current I_c (left panel) and the critical current normalised with the maximum critical current (at $B = 0$) $I_c^{\text{norm.}}$ (right panel) as a function of magnetic field B and split-gate voltage V_{SG}.

3.4.7. SUPPLEMENTARY NOTE 7: ANALYTICAL MODEL: LONG JUNCTION

We calculate the Josephson current $J(\chi)$ through the sample as a function of the superconducting phase difference $\chi = \chi_2 - \chi_1$ in the presence of magnetic field B, using the quasiclassical approach developed in Refs. [44, 49] and [50]. The essence of this approach lies in expressing the superconducting current density in terms of quasiclassical trajectories connecting the superconducting leads. These paths can be viewed as electron-hole "tubes" of width $\sim \lambda_F$, resulting from the Andreev reflection at the NS interfaces and corresponding to Andreev bound states. Each path is associated with the partial contribution to the Josephson current that depends on the positions of end points (y_1, y_2 in Supple-

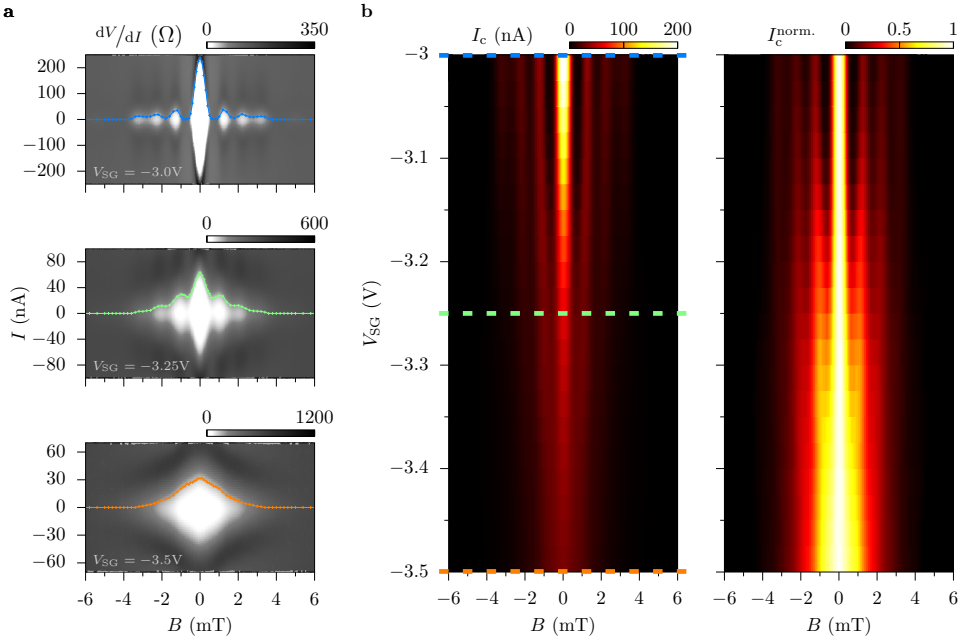

Figure 3.15: **Magnetic interferometry study of the transition from 2D to 1D confinement of the supercurrent at V_{BG} = 4 V. a,** Grey-scale maps of the differential resistance dV/dI versus bias current I and magnetic field B measured at $V_{SG} = -3$ V, $V_{SG} = -3.25$ V and $V_{SG} = -3.5$ V. The coloured doted lines correspond to the extracted I_c. **b,** Critical current I_c (left panel) and normalised critical current $I_c^{norm.}$ (right panel) mapped as a function of magnetic field B and split-gate voltage V_{SG}. The coloured dashed lines correspond to side-gate values where the $dV/dI(B, I)$ maps were measured in panels **a**.

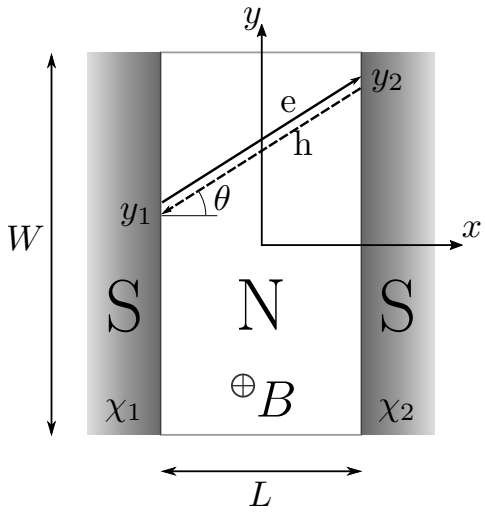

Figure 3.16: **Schematics of the SNS junction.** Schematics of the SNS setup at zero split-gate voltage.

mentary Figure 3.16) and on magnetic field that enters through the Aharonov-Bohm phase.

The magnetic interference pattern is obtained after the summation over all paths and maximizing the Josephson current with respect to χ:

$$I_c(\phi) = \max_\chi\{J(\chi,\phi)\}. \tag{3.9}$$

Here $\phi = \Phi/\Phi_0 = BWL/\Phi_0$ is the dimensionless magnetic flux through the sample in units of $\Phi_0 = \pi\hbar c/e$.

Since the thermal length $L_\mathcal{T} \sim \hbar v/(k_B\mathcal{T})$ for the experimental temperature is much larger than L, we set $\mathcal{T} = 0$. Following Ref. [44], we write the Josephson current for a long junction ($L \gg \xi$, where ξ is the superconducting coherence length) as an integral over the end points of the Andreev tubes (Supplementary Figure 3.16)

$$J(\chi,\phi) = \frac{2ev_F}{\pi\lambda_F L^2}\iint_{-W/2}^{W/2} dy_1 dy_2 \frac{\mathcal{J}[\tilde{\chi}(y_1,y_2)]}{\left[1+\left(\frac{y_1-y_2}{L}\right)^2\right]^2}, \tag{3.10}$$

where $\mathcal{J}$ is the dimensionless partial Josephson current associated with points y_1 and y_2 and $\tilde{\chi}(y_1,y_2)$ is the effective phase difference in magnetic field. Each straight trajectory connecting points y_1 and y_2 is characterised by angle θ between the trajectory and x-axis, $\tan\theta = (y_2-y_1)/L$. In the long-junction limit, the partial current is given by

$$\mathcal{J}(\chi) = \sum_{k=1}^{\infty}\frac{(-1)^{k+1}T^k}{k}\sin(k\chi) = \mathrm{Im}\left[\ln\left(1+Te^{i\chi}\right)\right], \quad \xi \ll L, \tag{3.11}$$

where we introduced the transmission probability $T \le 1$. For $T \ll 1$ only the $k = 1$ term is important, leading to

$$\mathcal{J}(\chi) \simeq T\sin\chi, \quad T \ll 1, \tag{3.12}$$

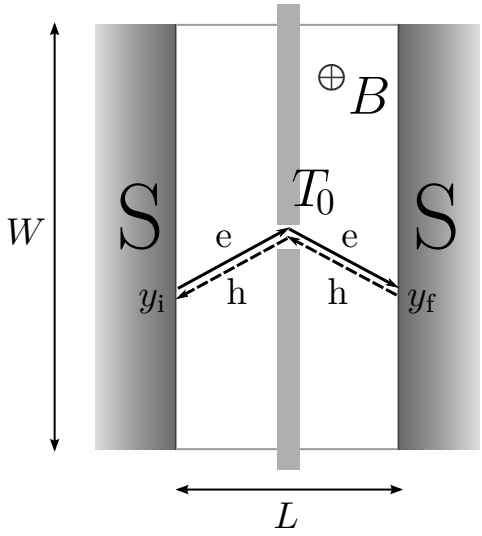

Figure 3.17: **Schematics of the SNS junction with QPC.**QPC setup with split-gate.

which is the conventional Josephson relation (also valid for $T \ll 1$ in the short-junction limit).

To include the magnetic field into the consideration, it is convenient to choose the x dependent gauge for the vector potential as in Ref. [50] (assuming small London penetration length for superconducting leads):

$$\mathbf{A} = A_y \mathbf{e}_y, \quad A_y = \begin{cases} -Bx, & -L/2 \le x \le L/2, \\ -\frac{1}{2}BL \operatorname{sign} x, & |x| > L/2. \end{cases} \tag{3.13}$$

For such a vector potential, the phase difference due to the magnetic phase acquired on straight trajectories connecting the two interfaces vanishes. At the same time, the superconducting phases at the interfaces become functions of y [50]:

$$\tilde{\chi}(y_1, y_2) = \chi - \frac{\pi\phi(y_1 + y_2)}{W}. \tag{3.14}$$

Let us now employ the formalism described above to the QPC setup. For simplicity, we neglect the geometrical width of the infinitely strong barriers. We assume that the setup is symmetric, *i.e.*, the QPC is located at $x = 0$ and $y = 0$. The QPC has the width which is of the order of (or smaller than) λ_F and hence is approximately characterised by an isotropic transmission probability. For low transmission $T_0 \ll 1$, one can retain only the conventional first harmonics in the partial Josephson currents, Supplementary Equation (3.12). This implies that under these assumptions, the shape of the magnetic interference pattern is, in fact, not sensitive to the relation between ξ and L (long *vs.* short junction).

In terms of the quasiclassical trajectories, the only possible trajectory connecting the points y_i and y_f at the opposite interfaces should pass through the QPC (here we discard

the boundary scattering). The trajectory is now parameterised by the two angles: θ_i, corresponding to the velocity in the region $-L/2 < x < 0$, and θ_f in the region $0 < x < L/2$ after transmission through the QPC. These angles satisfy the relations:

$$\tan\theta_i = -\frac{2y_i}{L}, \quad \tan\theta_f = \frac{2y_f}{L}. \tag{3.15}$$

With the gauge (3.13), the magnetic phase acquired within the sample reads:

$$\frac{2\pi}{\Phi_0}\int \mathrm{d}\mathbf{l}\cdot\mathbf{A} = -\frac{\pi B}{\Phi_0}\left(\frac{L}{2}\right)^2(-\tan\theta_i+\tan\theta_f) = -\frac{\pi\phi(y_i+y_f)}{2W}. \tag{3.16}$$

The total phase difference is given by the difference of the magnetic phase (3.16) and the superconducting phase difference in the presence of magnetic field [Supplementary Equation (3.14)]:

$$\tilde{\chi}(y_i,y_f) = \chi - \frac{\pi\phi}{2W}(y_i+y_f). \tag{3.17}$$

As compared to the case without the QPC, the phase difference induced by magnetic field is reduced by a factor of two. Indeed, the area between the Andreev tube connecting the points y_i and y_f and the line $y = 0$ is twice smaller for the trajectory going through the point $x = 0$, $y = 0$ than for the straight line.

The normalised critical current now reads

$$\frac{I_c(\phi)}{I_c(0)} = \frac{\max_\chi \int \mathrm{d}\theta_i \cos^2\theta_i \int \mathrm{d}\theta_f \cos\theta_f \mathscr{J}(\tilde{\chi}(\theta_i,\theta_f))}{\max_\chi \int \mathrm{d}\theta_i \cos^2\theta_i \int \mathrm{d}\theta_f \cos\theta_f \mathscr{J}(\chi)}. \tag{3.18}$$

In the limit of small transmission probability $T_0 \ll 1$ we use Supplementary Equation (3.12) for the partial Josephson current. The integrations over θ_i and θ_f then separate and the normalised critical current can be written as

$$\frac{I_c(\phi)}{I_c(0)} = \frac{\mathscr{I}_2(\phi)\mathscr{I}_{3/2}(\phi)}{\mathscr{I}_2(0)\mathscr{I}_{3/2}(0)}. \tag{3.19}$$

Here, the integrals $\mathscr{I}$ are defined as

$$\mathscr{I}_k(\phi) = \frac{2}{L}\int_{-W/2}^{+W/2} \mathrm{d}y \frac{\cos\left(\frac{\pi\phi y}{2W}\right)}{\left[1+\left(\frac{2y}{L}\right)^2\right]^k}. \tag{3.20}$$

At $\phi = 0$ we get

$$\mathscr{I}_2(0)\mathscr{I}_{3/2}(0) = \frac{L}{\sqrt{L^2+W^2}}\arctan\frac{W}{L} + \frac{L^2W}{(L^2+W^2)^{3/2}}. \tag{3.21}$$

The parabolic asymptotics of the critical current at small ϕ is found by expanding the cosine factors in the numerator:

$$\frac{I_c(\phi)}{I_{c0}} \simeq 1 - \frac{\pi^2\phi^2}{32} f_0(W/L), \tag{3.22}$$

$$f_0(x) = \frac{\sqrt{x^2+1}\log\left(\sqrt{x^2+1}+x\right)}{x} - \frac{x}{x+\left(x^2+1\right)\arctan(x)}. \tag{3.23}$$

In the limit of high fields, $\phi \to \infty$, we extend the integration in Supplementary Equation (3.20) over y_i and y_f to $\pm\infty$ and obtain

$$\frac{I_c(\phi)}{I_{c0}} \simeq \frac{\pi^{3/2}\left(1+x^2\right)^{3/2}}{8x^2\left[x+\left(1+x^2\right)\arctan x\right]}\left(\frac{\pi\phi}{2x}\right)^{3/2}\exp\left(-\frac{\pi\phi}{2x}\right). \tag{3.24}$$

The evaluation of the integrals in Supplementary Equation (3.18) with a transmission probability of $T_0 = 1/2$ in the whole range of magnetic fields yields the curve for the normalised critical current shown in Fig. 3.5(b) of the main text. Interestingly, the result for $T_0 = 1/2$ is almost indistinguishable from the analytical result for $T_0 \ll 1$. The width of the analytical curve was fitted to the experimental one thus accounting for the actual geometry and those factors (*e.g.*, the finite width of the barriers and the finite magnetic penetration depth) that were neglected in the simplified model.

3.4.8. SUPPLEMENTARY NOTE 9: EFFECT OF THE EDGE CURRENTS ON THE MAGNETO-INTERFEROMETRIC PATTERN

In our experiments, the opening of a band gap by using electrostatic gating is crucial to confine the charge carriers. However, mainly two mechanisms may prevent the confinement [27, 52–55, 82–84]. First, stacking defaults which may appear in bilayer graphene and induce topological currents at the boundaries between two domains [52, 84] (*i.e.* between AB and BA stacking domains, along the domain walls). Second, the edge states, which have been predicted to appear in gapped single and bilayer graphene [55, 82], may occur near the charge neutrality point [27, 53, 54]. Here we show that if extra current contributes to the total current, *i.e.* other than the current flowing through the constriction, one should be able to detect it via magneto-interferometry.

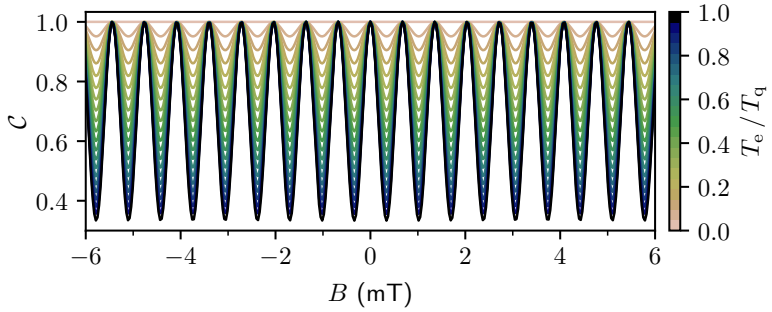

Figure 3.18: **Edge current simulations. a.** Correction factor $\mathscr{C}$ versus magnetic field B for different values of the transmission coefficient ratio T_e/T_q.

Following the analytical model presented in Supplementary Note 3.4.7, we have extended our calculations by including the possibilities for additional current to flow via the edge of the device as displayed in Fig. 3.8(a) of the main text. We use the evaluated

integrals within the limit conditions of small transmission $T_0 \ll 1$ and small values of ϕ (Supplementary Equation 3.22) and $\phi \to \infty$ (Supplementary Equation (3.24)) times a correction factor $\mathscr{C}$ which reads as follows:

$$\mathscr{C} = \frac{|T_q + T_e \cos(\pi\phi)/2|}{(T_q + T_e/2)}, \tag{3.25}$$

where T_q corresponds to the transmission coefficient of the QPC, T_e is the transmission coefficient of the edge channel, and ϕ is the dimensionless flux (flux in units of Φ_0).

Supplementary Figure 3.18 shows the variation of the correction factor $\mathscr{C}$ as a function of B for various values of the transmission coefficient ratio T_e/T_q. We note that $\mathscr{C}$ develops a significant amplitude modulation as $T_e/T_q \to 1$. So the more the edge states are prominent, the larger the variation of $\mathscr{C}$. As T_e raises, the modulation of $\mathscr{C}$ increases and $\mathscr{C}$ reaches zero at $T_e/2 \sim T_q$. When $T_e \gg T_q$, the correction factor $\mathscr{C}$ displays a pattern resembling to the one of a SQUID as expected. We have applied the correction factor to our model and estimated the effect of the presence of edge contact on the magneto-interference pattern as shown in Fig. 3.8 of the main text.

REFERENCES

[1] B. D. Josephson, *Possible new effects in superconductive tunnelling,* Physics Letters **1**, 251 (1962).

[2] P. W. Anderson and J. M. Rowell, *Probable observation of the josephson superconducting tunneling effect,* Phys. Rev. Lett. **10**, 230 (1963).

[3] M. Tinkham, *Introduction to Superconductivity* (Courier Dover, 2012).

[4] K. K. Likharev, *Superconducting weak links,* Rev. Mod. Phys. **51**, 101 (1979).

[5] A. Barone and G. Paterno, *Physics and Applications of the Josephson Effect* (Wiley, John, 1982).

[6] J. J. A. Baselmans, A. F. Morpurgo, B. J. van Wees, and T. M. Klapwijk, *Reversing the direction of the supercurrent in a controllable josephson junction,* Nature **397**, 43 (1999).

[7] T. Schäpers, *Superconductor/Semiconductor Junctions* (Springer, 2003).

[8] H. B. Heersche, P. Jarillo-Herrero, J. B. Oostinga, L. M. K. Vandersypen, and A. F. Morpurgo, *Bipolar supercurrent in graphene,* Nature **446**, 56 (2007).

[9] D. Zhang, J. Wang, A. M. DaSilva, J. S. Lee, H. R. Gutierrez, M. H. W. Chan, J. Jain, and N. Samarth, *Superconducting proximity effect and possible evidence for pearl vortices in a candidate topological insulator,* Phys. Rev. B **84**, 165120 (2011).

[10] B. Sacépé, J. B. Oostinga, J. Li, A. Ubaldini, N. J. G. Couto, E. Giannini, and A. F. Morpurgo, *Gate-tuned normal and superconducting transport at the surface of a topological insulator,* Nature Communications **2**, 575 (2011).

[11] M. Veldhorst, M. Snelder, M. Hoek, T. Gang, V. K. Guduru, X. L. Wang, U. Zeitler, W. G. van der Wiel, A. A. Golubov, H. Hilgenkamp, and A. Brinkman, *Josephson supercurrent through a topological insulator surface state,* Nature Materials **11**, 417 (2012).

[12] J. B. Oostinga, L. Maier, P. Schüffelgen, D. Knott, C. Ames, C. Brüne, G. Tkachov, H. Buhmann, and L. W. Molenkamp, *Josephson supercurrent through the topological surface states of strained bulk HgTe,* Phys. Rev. X **3**, 021007 (2013).

[13] S. Hart, H. Ren, T. Wagner, P. Leubner, M. Mühlbauer, C. Brüne, H. Buhmann, L. W. Molenkamp, and A. Yacoby, *Induced superconductivity in the quantum spin hall edge,* Nature Physics **10**, 638 (2014).

[14] E. Bocquillon, R. S. Deacon, J. Wiedenmann, P. Leubner, T. M. Klapwijk, C. Brüne, K. Ishibashi, H. Buhmann, and L. W. Molenkamp, *Gapless andreev bound states in the quantum spin hall insulator HgTe,* Nature Nanotechnology **12**, 137 (2017).

[15] S. De Franceschi, L. Kouwenhoven, C. Schönenberger, and W. Wernsdorfer, *Hybrid superconductor–quantum dot devices,* Nature Nanotechnology **5**, 703 (2010).

[16] M. F. Goffman, R. Cron, A. Levy Yeyati, P. Joyez, M. H. Devoret, D. Esteve, and C. Urbina, *Supercurrent in atomic point contacts and andreev states,* Phys. Rev. Lett. **85**, 170 (2000).

[17] X. Du, I. Skachko, and E. Y. Andrei, *Josephson current and multiple andreev reflections in graphene SNS junctions,* Phys. Rev. B **77**, 184507 (2008).

[18] F. Miao, W. Bao, H. Zhang, and C. N. Lau, *Premature switching in graphene josephson transistors,* Solid State Communications **149**, 1046 (2009).

[19] P. Rickhaus, M. Weiss, L. Marot, and C. Schönenberger, *Quantum hall effect in graphene with superconducting electrodes,* Nano Lett. **12**, 1942 (2012).

[20] U. C. Coskun, M. Brenner, T. Hymel, V. Vakaryuk, A. Levchenko, and A. Bezryadin, *Distribution of supercurrent switching in graphene under the proximity effect,* Phys. Rev. Lett. **108**, 097003 (2012).

[21] K. Komatsu, C. Li, S. Autier-Laurent, H. Bouchiat, and S. Guéron, *Superconducting proximity effect in long superconductor/graphene/superconductor junctions: From specular andreev reflection at zero field to the quantum hall regime,* Phys. Rev. B **86**, 115412 (2012).

[22] N. Mizuno, B. Nielsen, and X. Du, *Ballistic-like supercurrent in suspended graphene josephson weak links,* Nature Communications **4**, 2716 (2013).

[23] J.-H. Choi, G.-H. Lee, S. Park, D. Jeong, J.-O. Lee, H.-S. Sim, Y.-J. Doh, and H.-J. Lee, *Complete gate control of supercurrent in graphene p–n junctions,* Nature Communications **4**, 2525 (2013).

[24] L. Wang, I. Meric, P. Y. Huang, Q. Gao, Y. Gao, H. Tran, T. Taniguchi, K. Watanabe, L. M. Campos, D. A. Muller, J. Guo, P. Kim, J. Hone, K. L. Shepard, and C. R. Dean, *One-dimensional electrical contact to a two-dimensional material,* Science **342**, 614 (2013).

[25] V. E. Calado, S. Goswami, G. Nanda, M. Diez, A. R. Akhmerov, K. Watanabe, T. Taniguchi, T. M. Klapwijk, and L. M. K. Vandersypen, *Ballistic josephson junctions in edge-contacted graphene,* Nature Nanotechnology **10**, 761 (2015).

[26] M. Ben Shalom, M. J. Zhu, V. I. Fal'ko, A. Mishchenko, A. V. Kretinin, K. S. Novoselov, C. R. Woods, K. Watanabe, T. Taniguchi, A. K. Geim, and J. R. Prance, *Quantum oscillations of the critical current and high-field superconducting proximity in ballistic graphene,* Nature Physics **12**, 318 (2016).

[27] M. T. Allen, O. Shtanko, I. C. Fulga, A. R. Akhmerov, K. Watanabe, T. Taniguchi, P. Jarillo-Herrero, L. S. Levitov, and A. Yacoby, *Spatially resolved edge currents and guided-wave electronic states in graphene,* Nature Physics **12**, 128 (2016).

[28] F. Amet, C. T. Ke, I. V. Borzenets, J. Wang, K. Watanabe, T. Taniguchi, R. S. Deacon, M. Yamamoto, Y. Bomze, S. Tarucha, and G. Finkelstein, *Supercurrent in the quantum hall regime,* Science **352**, 966 (2016).

[29] I. Borzenets, F. Amet, C. Ke, A. Draelos, M. Wei, A. Seredinski, K. Watanabe, T. Taniguchi, Y. Bomze, M. Yamamoto, S. Tarucha, and G. Finkelstein, *Ballistic graphene josephson junctions from the short to the long junction regimes,* Phys. Rev. Lett. **117**, 237002 (2016).

[30] M. I. Katsnelson, *Graphene. Carbon in Two Dimensions* (Cambridge University Press, 2012).

[31] E. McCann, *Asymmetry gap in the electronic band structure of bilayer graphene,* Phys. Rev. B **74**, 161403 (2006).

[32] E. McCann and M. Koshino, *The electronic properties of bilayer graphene,* Rep. Prog. Phys. **76**, 056503 (2013).

[33] J. B. Oostinga, H. B. Heersche, X. Liu, A. F. Morpurgo, and L. M. K. Vandersypen, *Gate-induced insulating state in bilayer graphene devices,* Nature Materials **7**, 151 (2008).

[34] T. Taychatanapat and P. Jarillo-Herrero, *Electronic transport in dual-gated bilayer graphene at large displacement fields,* Phys. Rev. Lett. **105**, 166601 (2010).

[35] A. Varlet, M.-H. Liu, V. Krueckl, D. Bischoff, P. Simonet, K. Watanabe, T. Taniguchi, K. Richter, K. Ensslin, and T. Ihn, *Fabry-Pérot interference in gapped bilayer graphene with broken anti-Klein tunneling,* Phys. Rev. Lett. **113**, 116601 (2014).

[36] Y. Zhang, T.-T. Tang, C. Girit, Z. Hao, M. C. Martin, A. Zettl, M. F. Crommie, Y. R. Shen, and F. Wang, *Direct observation of a widely tunable bandgap in bilayer graphene,* Nature **459**, 820 (2009).

[37] H. I. Jørgensen, K. Grove-Rasmussen, T. Novotný, K. Flensberg, and P. E. Lindelof, *Electron transport in single-wall carbon nanotube weak links in the Fabry-Perot regime,* Phys. Rev. Lett. **96**, 207003 (2006).

[38] A. Furusaki, H. Takayanagi, and M. Tsukada, *Theory of quantum conduction of supercurrent through a constriction,* Phys. Rev. Lett. **67**, 132 (1991).

[39] A. Furusaki, H. Takayanagi, and M. Tsukada, *Josephson effect of the superconducting quantum point contact,* Phys. Rev. B **45**, 10563 (1992).

[40] H. Takayanagi, T. Akazaki, and J. Nitta, *Observation of maximum supercurrent quantization in a superconducting quantum point contact,* Phys. Rev. Lett. **75**, 3533 (1995).

[41] J. M. Rowell, *Magnetic field dependence of the josephson tunnel current,* Phys. Rev. Lett. **11**, 200 (1963).

[42] R. C. Dynes and T. A. Fulton, *Supercurrent density distribution in josephson junctions,* Phys. Rev. B **3**, 3015 (1971).

[43] H. H. Zappe, *Determination of the current density distribution in josephson tunnel junctions,* Phys. Rev. B **11**, 2535 (1975).

[44] V. Barzykin and A. M. Zagoskin, *Coherent transport and nonlocality in mesoscopic SNS junctions: anomalous magnetic interference patterns,* Superlattices and Microstructures **25**, 797 (1999).

[45] K. Kikuchi, H. Myoren, T. Iizuka, and S. Takada, *Normal-distribution-function-shaped josephson tunnel junctions,* Appl. Phys. Lett. **77**, 3660 (2000).

[46] L. Angers, F. Chiodi, G. Montambaux, M. Ferrier, S. Guéron, H. Bouchiat, and J. C. Cuevas, *Proximity dc squids in the long-junction limit,* Phys. Rev. B **77**, 165408 (2008).

[47] F. Chiodi, M. Ferrier, S. Guéron, J. C. Cuevas, G. Montambaux, F. Fortuna, A. Kasumov, and H. Bouchiat, *Geometry-related magnetic interference patterns in long SNS josephson junctions,* Phys. Rev. B **86**, 064510 (2012).

[48] M. Amado, A. Fornieri, F. Carillo, G. Biasiol, L. Sorba, V. Pellegrini, and F. Giazotto, *Electrostatic tailoring of magnetic interference in quantum point contact ballistic josephson junctions,* Phys. Rev. B **87**, 134506 (2013).

[49] D. E. Sheehy and A. M. Zagoskin, *Theory of anomalous magnetic interference pattern in mesoscopic superconducting/normal/superconducting josephson junctions,* Phys. Rev. B **68**, 144514 (2003).

[50] H. Meier, V. I. Fal'ko, and L. I. Glazman, *Edge effects in the magnetic interference pattern of a ballistic SNS junction,* Phys. Rev. B **93**, 184506 (2016).

[51] C. W. Groth, M. Wimmer, A. R. Akhmerov, and X. Waintal, *Kwant: a software package for quantum transport,* New J. Phys. **16**, 063065 (2014).

[52] L. Ju, Z. Shi, N. Nair, Y. Lv, C. Jin, J. Velasco Jr, C. Ojeda-Aristizabal, H. A. Bechtel, M. C. Martin, A. Zettl, J. Analytis, and F. Wang, *Topological valley transport at bilayer graphene domain walls,* Nature **520**, 650 (2015).

[53] M. J. Zhu, A. V. Kretinin, M. D. Thompson, D. A. Bandurin, S. Hu, G. L. Yu, J. Birkbeck, A. Mishchenko, I. J. Vera-Marun, K. Watanabe, T. Taniguchi, M. Polini, J. R. Prance, K. S. Novoselov, A. K. Geim, and M. Ben Shalom, *Edge currents shunt the insulating bulk in gapped graphene,* Nature Communications **8**, 14552 (2017).

[54] Z. Dou, S. Morikawa, A. Cresti, S.-W. Wang, C. G. Smith, C. Melios, O. Kazakova, K. Watanabe, T. Taniguchi, S. Masubuchi, T. Machida, and M. R. Connolly, *Imaging bulk and edge transport near the dirac point in graphene moiré superlattices,* Nano Lett. **18**, 2530 (2018).

[55] J. Li, I. Martin, M. Büttiker, and A. F. Morpurgo, *Topological origin of subgap conductance in insulating bilayer graphene,* Nature Physics **7**, 38 (2011).

[56] P. Blake, E. W. Hill, A. H. Castro Neto, K. S. Novoselov, D. Jiang, R. Yang, T. J. Booth, and A. K. Geim, *Making graphene visible,* Appl. Phys. Lett. **91**, 063124 (2007).

[57] A. C. Ferrari, J. C. Meyer, V. Scardaci, C. Casiraghi, M. Lazzeri, F. Mauri, S. Piscanec, D. Jiang, K. S. Novoselov, S. Roth, and A. K. Geim, *Raman spectrum of graphene and graphene layers,* Phys. Rev. Lett. **97**, 187401 (2006).

[58] C. Benz, M. Thürmer, F. Wu, Z. Ben Aziza, J. Mohrmann, H. v. Löhneysen, K. Watanabe, T. Taniguchi, and R. Danneau, *Graphene on boron nitride microwave transistors driven by graphene nanoribbon back-gates,* Appl. Phys. Lett. **102**, 033505 (2013).

[59] E. Pallecchi, C. Benz, A. C. Betz, H. v. Löhneysen, B. Plaçais, and R. Danneau, *Graphene microwave transistors on sapphire substrates,* Appl. Phys. Lett. **99**, 113502 (2011).

[60] K. Steinberg, M. Scheffler, and M. Dressel, *Quasiparticle response of superconducting aluminum to electromagnetic radiation,* Phys. Rev. B **77**, 214517 (2008).

[61] D. A. Abanin and L. S. Levitov, *Conformal invariance and shape-dependent conductance of graphene samples,* Phys. Rev. B **78**, 035416 (2008).

[62] J. R. Williams, D. A. Abanin, L. DiCarlo, L. S. Levitov, and C. M. Marcus, *Quantum hall conductance of two-terminal graphene devices,* Phys. Rev. B **80**, 045408 (2009).

[63] X. Du, I. Skachko, F. Duerr, A. Luican, and E. Y. Andrei, *Fractional quantum hall effect and insulating phase of dirac electrons in graphene,* Nature **462**, 192 (2009).

[64] K. I. Bolotin, F. Ghahari, M. D. Shulman, H. L. Stormer, and P. Kim, *Observation of the fractional quantum hall effect in graphene,* Nature **462**, 196 (2009).

[65] Skachko I., Du X., Duerr F., Luican A., Abanin D. A., Levitov L. S., and Andrei E. Y., *Fractional quantum hall effect in suspended graphene probed with two-terminal measurements,* Philosophical Transactions of the Royal Society A: Mathematical, Physical and Engineering Sciences **368**, 5403 (2010).

[66] A. V. Shytov, M. S. Rudner, and L. S. Levitov, *Klein backscattering and Fabry-Pérot interference in graphene heterojunctions,* Phys. Rev. Lett. **101**, 156804 (2008).

[67] A. F. Young and P. Kim, *Quantum interference and Klein tunnelling in graphene heterojunctions,* Nature Physics **5**, 222 (2009).

[68] P. Rickhaus, R. Maurand, M.-H. Liu, M. Weiss, K. Richter, and C. Schönenberger, *Ballistic interferences in suspended graphene,* Nature Communications **4**, 2342 (2013).

[69] B. J. van Wees, H. van Houten, C. W. J. Beenakker, J. G. Williamson, L. P. Kouwenhoven, D. van der Marel, and C. T. Foxon, *Quantized conductance of point contacts in a two-dimensional electron gas,* Phys. Rev. Lett. **60**, 848 (1988).

[70] D. A. Wharam, T. J. Thornton, R. Newbury, M. Pepper, H. Ahmed, J. E. F. Frost, D. G. Hasko, D. C. Peacock, D. A. Ritchie, and G. A. C. Jones, *One-dimensional transport and the quantisation of the ballistic resistance,* J. Phys. C: Solid State Phys. **21**, L209 (1988).

[71] S. Datta, *Electronic Transport in Mesoscopic Systems* (Cambridge University Press, 1995).

[72] Y.-M. Lin, V. Perebeinos, Z. Chen, and P. Avouris, *Electrical observation of subband formation in graphene nanoribbons,* Phys. Rev. B **78**, 161409 (2008).

[73] C. Lian, K. Tahy, T. Fang, G. Li, H. G. Xing, and D. Jena, *Quantum transport in graphene nanoribbons patterned by metal masks,* Appl. Phys. Lett. **96**, 103109 (2010).

[74] N. Tombros, A. Veligura, J. Junesch, M. H. D. Guimarães, I. J. Vera-Marun, H. T. Jonkman, and B. J. van Wees, *Quantized conductance of a suspended graphene nanoconstriction,* Nature Physics **7**, 697 (2011).

[75] M. T. Allen, J. Martin, and A. Yacoby, *Gate-defined quantum confinement in suspended bilayer graphene,* Nature Communications **3**, 934 (2012).

[76] A. S. M. Goossens, S. C. M. Driessen, T. A. Baart, K. Watanabe, T. Taniguchi, and L. M. K. Vandersypen, *Gate-defined confinement in bilayer graphene-hexagonal boron nitride hybrid devices,* Nano Lett. **12**, 4656 (2012).

[77] S. Dröscher, C. Barraud, K. Watanabe, T. Taniguchi, T. Ihn, and K. Ensslin, *Electron flow in split-gated bilayer graphene,* New J. Phys. **14**, 103007 (2012).

[78] B. Terrés, L. A. Chizhova, F. Libisch, J. Peiro, D. Jörger, S. Engels, A. Girschik, K. Watanabe, T. Taniguchi, S. V. Rotkin, J. Burgdörfer, and C. Stampfer, *Size quantization of dirac fermions in graphene constrictions,* Nature Communications **7**, 11528 (2016).

[79] J. Li, K. Wang, K. J. McFaul, Z. Zern, Y. Ren, K. Watanabe, T. Taniguchi, Z. Qiao, and J. Zhu, *Gate-controlled topological conducting channels in bilayer graphene,* Nature Nanotechnology **11**, 1060 (2016).

[80] S. Somanchi, B. Terrés, J. Peiro, M. Staggenborg, K. Watanabe, T. Taniguchi, B. Beschoten, and C. Stampfer, *From diffusive to ballistic transport in etched graphene constrictions and nanoribbons,* Annalen der Physik **529**, 1700082 (2017).

[81] H. Overweg, H. Eggimann, X. Chen, S. Slizovskiy, M. Eich, R. Pisoni, Y. Lee, P. Rickhaus, K. Watanabe, T. Taniguchi, V. Fal'ko, T. Ihn, and K. Ensslin, *Electrostatically induced quantum point contacts in bilayer graphene,* Nano Lett. **18**, 553 (2018).

[82] W. Yao, S. A. Yang, and Q. Niu, *Edge states in graphene: From gapped flat-band to gapless chiral modes,* Phys. Rev. Lett. **102**, 096801 (2009).

[83] F. Zhang, A. H. MacDonald, and E. J. Mele, *Valley chern numbers and boundary modes in gapped bilayer graphene,* PNAS **110**, 10546 (2013).

[84] J. S. Alden, A. W. Tsen, P. Y. Huang, R. Hovden, L. Brown, J. Park, D. A. Muller, and P. L. McEuen, *Strain solitons and topological defects in bilayer graphene,* PNAS **110**, 11256 (2013).

4

HYBRID KERNEL POLYNOMIAL METHOD

This chapter has been previously published as M. Irfan, S. R. Kuppuswamy, D. Varjas, P. M. Perez-Piskunow, M. Wimmer, and A. R. Akhmerov, *Hybrid kernel polynomial method*, arXiv:1909.09649 (2019).
My contribution to this work is the implementation of the hybrid expectation value calculation and applying it to the Josephson junction example.

4.1. INTRODUCTION

The behavior of the Fermi sea is governed by both the few partially occupied states near the Fermi level, and the overall effect of the large number of fully occupied states. Therefore, in order to accurately capture the relevant physics, one needs to combine high resolution information about the former with integrated contribution of the latter. A similar need to combine integrated information with high resolution arises when constructing effective models using Löwdin partitioning or Schrieffer-Wolff transformation [1–4]. In a computational context, simultaneously satisfying these two requirements is only possible with the full knowledge of the spectrum. Therefore analyzing a system with size N Hilbert space requires the full cost of $\mathcal{O}(N^3)$ operations of dense linear algebra, prohibiting the exploitation of the sparsity of the Hamiltonian.

Applying a sparse Hamiltonian to a state is cheap. Iterative diagonalization algorithms efficiently utilize this to obtain a small set of eigenenergies and eigenvectors at a low cost [5]. For example, the algorithms implemented in ARPACK [6] combined with a sparse direct linear solver (such as MUMPS [7, 8]) allow to compute several eigenvectors around any interior point of the spectrum. The kernel polynomial method (KPM) [9] also utilizes the sparsity structure, but to obtain limited energy resolution information about the full spectrum. This is possible due to recursive computation of the Chebyshev decomposition of the Hamiltonian action on a vector.

In this work we propose a family of algorithms which we call "hybrid KPM" that combine the integral information of KPM with the high precision of diagonalization. The building block of these methods is the amended KPM expansion, where we subtract the contribution of the known part of the spectrum. Hybrid KPM algorithms apply both to the computation of thermodynamic properties at low temperatures, and the construction of effective Hamiltonians restricted to a small subspace. We demonstrate on a set of physical problems that hybrid KPM achieves increased precision at the same computational cost.

We apply and benchmark hybrid KPM by computing supercurrent and Josephson inductance of a long Josephson junction [10–12], where both the contribution of discrete subgap states and the continuum are of the same order. Turning to the effective models, we consider two model systems: tunneling Hamiltonian of two coupled quantum dots [13], and band structure of a semiconductor nanowire [14–17]. In both cases we start from a microscopic Hamiltonian and obtain an accurate effective model, which requires using up to 3rd order perturbation theory.

4.2. KERNEL POLYNOMIAL METHOD

To compute thermodynamic properties and effective models, one needs to evaluate the action of the Fermi function or Green's function of the Hamiltonian on a state. The kernel polynomial method (KPM) [9] enables an efficient approximation of such functions of operators. We start by rescaling a Hamiltonian $\hat{H}$ such that its spectrum $\{E_k\}$ is bounded to the interval $(-1, 1)$. In general, a function $f(\hat{H}, \lambda)$ of a Hermitian operator $\hat{H}$ and a set of parameters λ can be calculated using the eigendecomposition $\hat{H} = \sum_k E_k |\psi_k\rangle\langle\psi_k|$ as

$$f(\hat{H}, \lambda) \equiv \sum_k f(E_k, \lambda) |\psi_k\rangle\langle\psi_k| , \tag{4.1}$$

where $f(E,\lambda)$ is a scalar function. The expansion in eigenfunctions is computationally expensive since it requires the full diagonalization of $\hat{H}$. This process scales as $\mathcal{O}(N^3)$ with the N size of the Hilbert space.

An alternative approach—KPM—utilizes the expansion of the scalar function $f(E,\lambda)$ in terms of Chebyshev polynomials T_m

$$f(E,\lambda) = \sum_{m=0}^{\infty} \alpha_m(\lambda) T_m(E), \tag{4.2}$$

to build the operator function $f(\hat{H},\lambda)$ (see Appendix 4.7.1 for expansions of commonly used functions). The Chebyshev polynomials $T_m(x) = \cos(m \arccos x)$ form a complete basis in the interval $(-1,1)$. They are orthogonal under the inner product

$$\langle f \cdot g \rangle = \int_{-1}^{1} \frac{f(x)g(x)}{\pi\sqrt{1-x^2}} dx, \tag{4.3}$$

and satisfy the recursion relation $T_{m+1}(x) = 2xT_m(x) - T_{m-1}(x)$. The Chebyshev coefficients α_m are calculated using the inner product from Eq. (4.3) with variable E

$$\alpha_m(\lambda) = \langle f(E,\lambda) \cdot T_m(E) \rangle, \tag{4.4}$$

and the same coefficients apply to the polynomial expansion of the operator function

$$f(\hat{H},\lambda) = \sum_{m=0}^{\infty} \alpha_m(\lambda) T_m(\hat{H}). \tag{4.5}$$

We are interested in the action of $f(\hat{H},\lambda)$ on a set of vectors. In such situations, the expensive part of the computation is to calculate $T_m(\hat{H})|v\rangle$, and once we have done that, the coefficients can be readily computed (in most cases analytically) for any value of the parameters λ.

In practice, the magnitude of the coefficients α_m decays with m and we truncate the series to a finite order M. To stabilize the convergence and avoid Gibbs oscillations, while ensuring positivity, we use either the Jackson or Lorentz kernel [9], which is a set of prefactors $g_{m,M}$ that modify the coefficients to $\tilde{\alpha}_m(\lambda) = g_{m,M}\alpha_m(\lambda)$. The recently developed Chebyshev polynomial Green's function method [18] avoids the need for introducing the kernel by approximating a smoothened Green's function. Because we aim to resolve individual states, we do not expect this technique to be useful in the hybrid setting.

The error of the KPM approximation comes from the function f being replaced by its finite order Chebyshev polynomial approximation:

$$f(\hat{H},\lambda) \overset{\text{KPM}}{\approx} \tilde{f}(\hat{H},\lambda) \equiv \sum_k \tilde{f}(E_k,\lambda)\,|\psi_k\rangle\langle\psi_k|, \tag{4.6}$$

with

$$\tilde{f}(E,\lambda) = \sum_{m=0}^{M} \tilde{\alpha}_m(\lambda) T_m(E). \tag{4.7}$$

This error is small if the function is smooth, or there are no eigenvalues of $\hat{H}$ in regions where it changes fast. The order of the approximation M, together with the choice of the kernel, sets the energy resolution of the approximation, which for the Jackson kernel is inversely proportional to M. The Chebyshev expansion of order M captures features larger than W/M, where W is the full bandwidth of $\hat{H}$ [9].

Hamiltonians and other observables that appear in physical problems are typically sparse matrices where the number of nonzero entries is proportional to the system size N. This allows calculating a sparse matrix–vector product in $\mathcal{O}(N)$ time, much faster than the $\mathcal{O}(N^2)$ scaling of dense matrix–vector products. The recursion relation for Chebyshev polynomials can then be rewritten for the operator function acting on a vector as

$$|v_{m+1}\rangle = 2\hat{H}|v_m\rangle - |v_{m-1}\rangle\,, \tag{4.8}$$

where $|v_m\rangle = T_m(\hat{H})|v\rangle$. Hence, the Chebyshev expanded action $f(\hat{H},\lambda)|v\rangle$ up to order M can be computed in $\mathcal{O}(NM)$ time. The computational effort of KPM scales as $\mathcal{O}(NW/\Delta)$ where Δ is the required energy resolution. KPM is most efficient when the desired energy resolution is much coarser than the typical level spacing, that is when $\Delta \gg W/N$, and $M = W/\Delta \ll N$.

The key idea behind hybrid KPM is using a more accurate approximation of $f(\hat{H},\lambda)$:

$$\begin{aligned} f(\hat{H},\lambda) \overset{\text{hybrid}}{\approx} \tilde{f}(\hat{H},\lambda) &- \sum_{k\in A} \tilde{f}(E_k,\lambda)\,|\psi_k\rangle\langle\psi_k| \\ &+ \sum_{k\in A} f(E_k,\lambda)\,|\psi_k\rangle\langle\psi_k|\,. \end{aligned} \tag{4.9}$$

Here we combine the KPM approximation of the complete spectrum with the exact contribution of a few states in a small subspace A. To avoid double-counting we subtract the KPM contribution of the exactly known states and add back their exact contribution. Approximation (4.6) has a large error due to states in the energy range where f changes rapidly. Our approach fixes this problem by using a sparse eigensolver to find these states and taking their contribution into account exactly, while keeping the energy resolution of KPM low.

4.3. LÖWDIN PERTURBATION THEORY

Quantum systems often have many degrees of freedom, while only a few states (for example the lowest energy ones) are of interest for physical understanding. Perturbative effective models describe such a situation well by constructing a Hamiltonian of the small "interesting" subspace, and integrating out the remaining states. After the integration, the effective model includes both a shift in the energy of the eigenstates and additional coupling terms mixing various eigenstates.

We use the Löwdin partitioning approach [1, 3, 4, 19] (also known as Schrieffer–Wolff transformation [2]) to calculate the effective Hamiltonian. If applied directly, this approach requires full diagonalization of the unperturbed Hamiltonian, making it unfeasible in large systems. We find, however, that it is sufficient to only exactly know the states in the interesting subspace, and use hybrid KPM to integrate out the remaining states. This allows us to compute effective models in systems with millions of degrees of freedom, as long as the interesting subspace is small.

4.3.1. LÖWDIN PARTITIONING

We start by separating initial Hamiltonian into unperturbed part H_0 and perturbation with λ_α as small parameters:

$$H = H_0 + \sum_\alpha \lambda_\alpha H'_\alpha. \tag{4.10}$$

Assuming that the eigenstates and energies of H_0 are known

$$H_0 |\psi_n\rangle = E_n |\psi_n\rangle, \tag{4.11}$$

we split states $|\psi_n\rangle$ into two groups, A and B. We are interested in states from group A whereas the effect of states B we include via perturbation theory. We assume that these two groups of states are separated in energy, but states within A or B may be degenerate. The goal is to find a unitary basis transformation with skew-Hermitian S as

$$\tilde{H} = e^{-S} H e^{S}, \tag{4.12}$$

such that the transformed Hamiltonian $\tilde{H}$ does not couple the A and B subspaces, and the block in the A subspace is the effective Hamiltonian, $H_{\text{eff}} = \tilde{H}_{AA}$. We find S and H_{eff} order-by-order in the small parameters (for details see Appendix 4.7.2):

$$H_{\text{eff}} = \tilde{H}^{(0)} + \sum_\alpha \lambda_\alpha \tilde{H}^{(1,\alpha)} + \sum_{\alpha\beta} \lambda_\alpha \lambda_\beta \tilde{H}^{(2,\alpha\beta)} + \ldots. \tag{4.13}$$

When the A subspace corresponds to a single eigenvalue, that is possibly degenerate, the Löwdin perturbation theory reproduces the conventional perturbation theory.

4.3.2. THE KPM APPROXIMATION OF EFFECTIVE HAMILTONIAN

To provide a concrete example, we consider the second order effective Hamiltonian with one small parameter,

$$H_{\text{eff}} = \tilde{H}^{(0)} + \lambda \tilde{H}^{(1)} + \lambda^2 \tilde{H}^{(2)}, \tag{4.14a}$$

with the explicit terms

$$\tilde{H}^{(0)}_{mn} = E_m \delta_{m,n}, \tag{4.14b}$$

$$\tilde{H}^{(1)}_{mn} = \langle \psi_m | H' | \psi_n \rangle, \tag{4.14c}$$

$$\tilde{H}^{(2)}_{mn} = \frac{1}{2} \sum_{l \in B} \left(\frac{\langle \psi_m | H' | \psi_l \rangle \langle \psi_l | H' | \psi_n \rangle}{E_m - E_l} + \frac{\langle \psi_m | H' | \psi_l \rangle \langle \psi_l | H' | \psi_n \rangle}{E_n - E_l} \right), \tag{4.14d}$$

where m and n index states of the A subspace and l indexes states of the B subspace.

We rewrite the first term in the second order contribution as

$$\begin{aligned} &\sum_{l \in B} \frac{\langle \psi_m | H' | \psi_l \rangle \langle \psi_l | H' | \psi_n \rangle}{E_m - E_l} \\ &= \langle \psi_m | H' \left(\sum_{l \in B} \frac{|\psi_l\rangle \langle \psi_l|}{E_m - E_l} \right) H' | \psi_n \rangle \\ &= \langle \psi_m | H' P_B G_0(E_m) P_B H' | \psi_n \rangle, \end{aligned} \tag{4.15}$$

where G_0 is the unperturbed Green's function

$$G_0(E) = \frac{1}{E - H_0} = \sum_i \frac{|\psi_i\rangle\langle\psi_i|}{E - E_i}, \tag{4.16}$$

and P_B is the projector onto the B subspace.

This formulation is well suited for approximate evaluation using the KPM expanded Green's function. The Green's function only acts on a small set of vectors, $|\phi_n\rangle = P_B H' |\psi_n\rangle$ for $n \in A$. We obtain the exact eigenstates of the A subspace using sparse diagonalization of H_0, and compute P_B using $P_B = \mathbb{1} - P_A$. The states $|\phi_n\rangle$ are purely in the B subspace, and we evaluate the Green's function at the energy of a state in the A subspace. The energy separation between the two sets of states removes all divergences, so that the action of G_0 is well approximated using KPM with a low energy resolution. After these substitutions, the second order contribution simplifies to

$$\tilde{H}^{(2)}_{mn} = \frac{1}{2}\langle\phi_m|\left[G_0(E_m) + G_0(E_n)\right]|\phi_n\rangle\,. \tag{4.17}$$

Similar simplification in terms of G_0 is also possible for all higher orders, for details see Appendix 4.7.3.

4.3.3. EFFECTIVE HAMILTONIAN WITH HYBRID KPM

In order to accurately approximate the action of G_0 on B states closest to the A subspace in energy, we need to choose the number of Chebyshev moments of the order of W/Δ, where W is the full bandwidth of H_0 and Δ is the gap between A and B states. Hence, for small Δ accurate calculation using KPM becomes computationally expensive. Alternatively, knowing all the B eigenstates would allow exact evaluation of the Green's function, at even higher computational cost.

To solve this problem, we propose the hybrid KPM approach, where only a subset B_e of the B eigenstates is known explicitly. These we choose to be the eigenstates with closest energy to the A states, and are obtained using sparse diagonalization. We split the Green's function of the B subspace to two terms:

$$G_0(E)P_B = \sum_{l\in B_e} \frac{|\psi_l\rangle\langle\psi_l|}{E - E_l} + G_0^{\mathrm{KPM}}(E)(P_B - P_{B_e}), \tag{4.18}$$

where P_B and P_{B_e} are projectors to the B and B_e subspaces, and G_0^{KPM} is the KPM approximated Green's function.

4.4. COMPUTATION OF THERMODYNAMIC QUANTITIES

4.4.1. EVALUATION OF OPERATOR EXPECTATION VALUES

Physical observables in a non-interacting fermionic system are thermal expectation values of a Hermitian operator $\hat{A}$:

$$\langle\hat{A}\rangle_{E_F} = \sum_k f(E_k, E_F)\langle\psi_k|\hat{A}|\psi_k\rangle\,, \tag{4.19}$$

where the sum runs over all eigenstates of the Hamiltonian $|\psi_k\rangle$ with eigenenergies E_k. The occupation of the states is given by the Fermi function

$$f(E, E_F) = \frac{1}{e^{\beta(E-E_F)}+1} \tag{4.20}$$

with $\beta = (k_B T)^{-1}$ and E_F the Fermi energy. Converting the sum to an integral over energy by inserting a delta function, we introduce the spectral density of the operator $A(E) \equiv \mathrm{Tr}\,\hat{A}\,\delta(E-\hat{H})$, yielding

$$\langle \hat{A} \rangle_{E_F} = \int dE\, f(E, E_F) A(E). \tag{4.21}$$

This can be rewritten as a trace using the operator function formalism, and readily evaluated using KPM:

$$\langle \hat{A} \rangle_{E_F} = \mathrm{Tr}\,\hat{A}\, f(\hat{H}, E_F) = \sum_m \tilde{\alpha}_m(E_F)\mu_m, \tag{4.22}$$

where the KPM moments are

$$\mu_m = \mathrm{Tr}\,\hat{A}\, T_m(\hat{H}). \tag{4.23}$$

The Fermi function changes rapidly in the interval $1/\beta$ around the Fermi level. Our strategy is to compute the states near the Fermi level exactly and approximate the rest of the states using low order KPM. Following the hybrid KPM approximation, we substitute Eq. (4.9) into Eq. (4.22):

$$\begin{aligned}\langle \hat{A} \rangle_{E_F} \approx &\sum_m \tilde{\alpha}_m(E_F)\left(\mu_m - \mu_m^A\right) \\ &+ \sum_{i\in A} f(E_i, E_F)\,\langle \psi_i|\,\hat{A}\,|\psi_i\rangle\,,\end{aligned} \tag{4.24}$$

where the KPM moments restricted to the A subspace are

$$\mu_m^A = \sum_{i\in A} T_m(E_i)\,\langle \psi_i|\,\hat{A}\,|\psi_i\rangle\,. \tag{4.25}$$

The trace in the full contribution is efficiently approximated using the stochastic trace approximation [9]. The exact evaluation of the trace is also feasible if the operator $\hat{A}$ has low rank and the basis of its image space is explicitly known:

$$\mu_m = \sum_{|\psi\rangle\in \mathrm{Im}\,\hat{A}} \langle \psi|\,\hat{A}\,T_m(\hat{H})\,|\psi\rangle\,. \tag{4.26}$$

4.4.2. PERTURBATIVE KPM

We now generalize KPM to allow order-by-order expansion of thermodynamic expectation values. We consider a generic function g and perturbed Hamiltonian $\hat{H} = \hat{H}_0 + \lambda\hat{H}_1$ where λ is a small parameter. Our goal is to evaluate $\mathrm{Tr}\,g(\hat{H})$ order-by-order in the small parameter. For example, the expectation value of the energy of a filled Fermi sea is $\langle E \rangle = \mathrm{Tr}\,g(\hat{H})$ with $g(E) = Ef(E, E_F)$. Our method also applies to expressions of the form $\mathrm{Tr}\,\hat{A}g(\hat{H})$, but we restrict to the $\hat{A} = \mathbb{1}$ case for brevity.

Our idea is to keep track of parameter dependence when computing the Chebyshev recursion relation (4.8), allowing $\hat{H}$ and $|v_m\rangle$ to be polynomials of λ. Since we are only interested in the result up to λ^n order, we discard all higher order terms at every step of the iteration, resulting in KPM moments μ_m and expectation value $\operatorname{Tr} g(\hat{H})$ that is also an n'th order polynomial of λ. At a finite number of moments M this method reproduces the series expansion of $\operatorname{Tr} \tilde{g}(\hat{H})$ in λ, where $\tilde{g}$ is the Chebyshev approximation of g. The resulting increase in computational cost scales as $\mathcal{O}(n^2)$, making this method feasible at low expansion orders.

Rearranging the terms in the perturbation expansion allows us to efficiently calculate the trace when the image space of the perturbation H_1 is small. After a cyclic permutation inside the trace, the λ-linear term in the expansion becomes

$$\frac{d}{d\lambda} \operatorname{Tr} g(\hat{H})_{\lambda=0} = \operatorname{Tr} g'(\hat{H}_0)\hat{H}_1, \tag{4.27}$$

where g' is the derivative of g. Because $\hat{H}_1$ is the rightmost operator, the trace reduces to a sum over a basis of the image space of $\hat{H}_1$. Applying this to the energy expectation value in the zero temperature limit where f is a step function [using that $x\delta(x) = 0$] we get

$$\begin{aligned} \frac{d}{d\lambda}\langle E\rangle_{\lambda=0} &= \frac{d}{d\lambda} \operatorname{Tr} \hat{H} f(\hat{H})_{\lambda=0} \\ &= \operatorname{Tr} f(\hat{H}_0)\hat{H}_1 = \langle \hat{H}_1\rangle_{\lambda=0} \end{aligned} \tag{4.28}$$

which is the same as the ground state expectation value of H_1, and was already discussed in the previous section. Similar simplifications apply to all higher orders; here we present the second order case in detail. For a generic function g and Hamiltonian $\hat{H} = \hat{H}_0 + \lambda\hat{H}_1 + \lambda^2\hat{H}_2$, by expanding and permuting terms proportional to λ^2 we find

$$\begin{aligned} &\frac{1}{2}\frac{d^2}{d\lambda^2} \operatorname{Tr} g(\hat{H})_{\lambda=0} \\ &= \operatorname{Tr} g'(\hat{H}_0)\hat{H}_2 + \frac{1}{2}\frac{d}{d\lambda} \operatorname{Tr} g'(\hat{H})\hat{H}_1{}_{\lambda=0} \end{aligned} \tag{4.29}$$

To evaluate the traces we sum over the basis of the image spaces of $\hat{H}_2$ and $\hat{H}_1$ respectively in the two terms. To obtain the second term we use the KPM expansion to first order in λ.

To apply the hybrid KPM approach to the perturbative KPM, we utilize the hybrid KPM Löwdin perturbation theory developed in Sec. 4.3, obtaining the perturbation series of the A subspace eigenenergies. We treat a single eigenpair $\left(E_k, |\psi_k\rangle\right)$ of $\hat{H}_0$ as the A subspace for the purposes of Löwdin perturbation theory, and use the rest of the exactly known states as the B_e subspace in the hybrid evaluation of the Green's function. Repeating this for every A eigenstate produces the power series expansions of the perturbed E_k up to the desired order. Combining the perturbative KPM result for the full spectrum and substituting the Löwdin expansion of the A subspace we obtain

$$\operatorname{Tr} g(\hat{H}) \overset{\text{hybrid}}{\approx} \operatorname{Tr} \tilde{g}(\hat{H}) - \sum_{k\in A} \tilde{g}(E_k) + \sum_{k\in A} g(E_k). \tag{4.30}$$

We compute the series expansion of the last two terms in λ using the Taylor series of g and $\tilde{g}$. The hybrid Löwdin approximation has the highest accuracy for states in the

middle of the A subspace energy range, which we choose to coincide with the fastest-changing region of g'. For states close to the edge of the A subspace energy range the approximation is less accurate, but, at the same time, the difference between g and $\tilde{g}$ is also small, resulting in a small overall error.

4.5. APPLICATIONS

4.5.1. SUPERCURRENT AND JOSEPHSON INDUCTANCE

As an illustration we apply the hybrid KPM method to calculate supercurrent in a Josephson junction [10]. When the Thouless energy is smaller than the superconducting gap Δ—the so-called long-junction regime [11, 12]—the continuum spectrum at $|E| > \Delta$ also responds to the superconducting phase difference and contributes to the total supercurrent [20]. In the hybrid KPM approach we calculate the subgap states using exact diagonalization, and estimate the contribution of continuum states using KPM.

We consider a Josephson junction with a normal region of length L_N, superconducting leads of length L_S and width W as shown in the inset of Fig. 4.1. For simplicity, we consider a spinless Bogoliubov-de Gennes (BdG) Hamiltonian without magnetic field:

$$H_{BdG} = \begin{pmatrix} \frac{\mathbf{p}^2}{2m} - \mu & \Delta(x) \\ \Delta^*(x) & \mu - \frac{\mathbf{p}^2}{2m} \end{pmatrix}, \tag{4.31}$$

with $\mathbf{p}$ the momentum operator, m the effective electron mass, and μ the chemical potential. The superconducting order parameter $\Delta(x)$ is zero in the normal region and Δ in the superconducting leads. We discretize this Hamiltonian on a square lattice with lattice constant a and a nearest neighbour hopping $t = \hbar^2/(2ma^2)$. We introduce the superconducting phase difference ϕ through a Peierls substitution

$$H_{ij} \to \begin{cases} H_{ij} \exp(i\phi\tau_z/2) & \text{if } i \in L \text{ and } j \in R \\ \exp(-i\phi\tau_z/2) H_{ij} & \text{if } i \in R \text{ and } j \in L\,, \\ H_{ij} & \text{otherwise} \end{cases} \tag{4.32}$$

with H_{ij} the hopping Hamiltonian between site i and j in the BdG formalism, τ_z the Pauli matrix in particle-hole space. Finally, L and R correspond to the left and right sides of a cut in the normal region parallel to the normal-metal–superconductor interface (see the inset of Fig. 4.1). The current operator across the cut is the derivative of the Hamiltonian with respect to the flux:

$$\hat{I} = \frac{2e}{\hbar} \frac{d\hat{H}}{d\phi}. \tag{4.33}$$

In order to calculate the KPM contribution to the trace

$$\langle \hat{I} \rangle = \mathrm{Tr}\, \hat{I} f(\hat{H}), \tag{4.34}$$

we use the basis of the sites next to the cut. All other states are annihilated by the current operator and do not contribute to the current.

Here and in the rest of the manuscript we use the Kwant software package [21] to construct tight-binding Hamiltonians. We consider a Josephson junction of length

$L_N = L_S = 50a$ and width $W = 15a$ and set the parameters $\mu = 0.2t$ and $\Delta = 0.15t$. As explained in sec. 4.4, we calculate the subgap Andreev bound states exactly using sparse diagonalization and treat them as the A subspace. We show the spectral density of the current operator $I(E)$ in Fig. 4.1, where we plot the contributions of subgap and continuum states separately. The KPM spectrum of the current operator vanishes at this resolution with $M = 500$ moments. The contribution of only the continuum states calculated with hybrid KPM is, however, non-vanishing, and the exactly known subgap states contribute Dirac delta peaks.

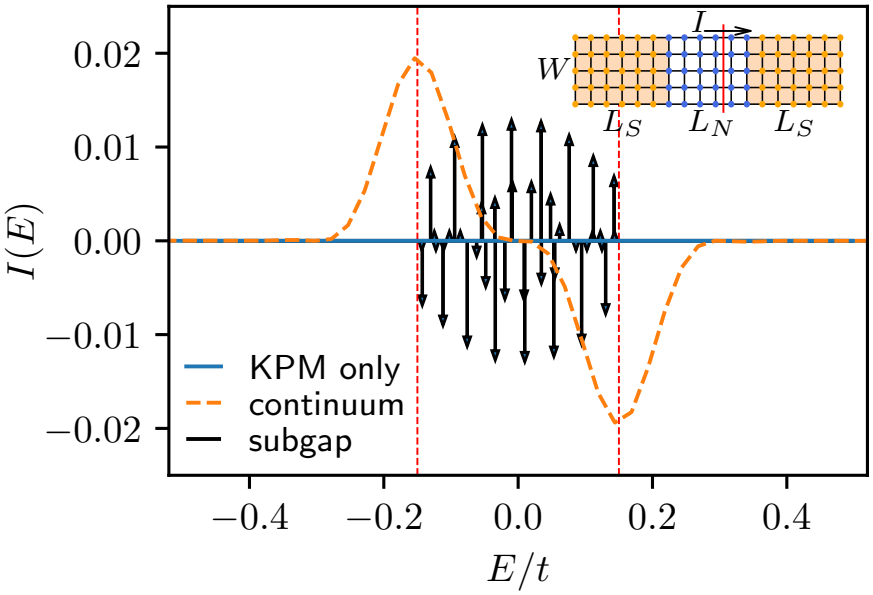

Figure 4.1: Current operator spectrum as a function of energy with fixed relative superconducting phase of $\pi/2$. The solid blue line represents the KPM only spectrum of the current operator; the arrows represent the Dirac delta contributions of subgap states; the dashed orange line shows the contribution of the continuum states. Inset: Sketch of the system. The shaded regions are superconducting with a normal region in the middle. The red line represents the cut for which we calculate the supercurrent.

We compute the contributions of the Andreev states and of the continuum states to the current-phase relation, with the result shown in Fig. 4.2. The contributions of both the subgap and the continuum states are significant, while their sum agrees with the exact result to a high precision.

To demonstrate hybrid KPM in higher order perturbation theory, we turn to the Josephson inductance. The inverse of the junction inductance is equal to the derivative of the current expectation value with respect to the flux:

$$L_J^{-1} = \frac{(2e)^2}{\hbar^2} \frac{d^2}{d\phi^2} \langle \hat{H} \rangle . \tag{4.35}$$

We evaluate this expression using the hybrid method discussed in Sec. 4.4.2 taking into account the second derivative of the Hamiltonian, with the result shown in Fig. 4.3. The

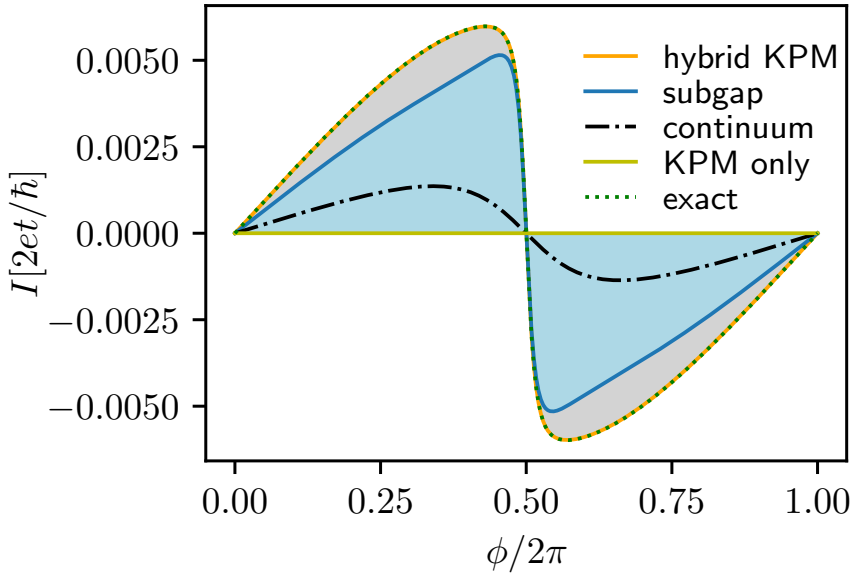

Figure 4.2: Supercurrent as a function of the superconducting phase difference. The orange line is the total supercurrent through a Josephson junction calculated with hybrid KPM, whereas the blue and black lines are the contributions from subgap and continuum states respectively. The hybrid KPM result agrees with full diagonalization, while the pure KPM estimate vanishes.

sharp peak in L_J^{-1} at $\phi = \pi$ is accurately captured by the direct evaluation of the second derivative using our method, while accurate calculation using a discrete derivative of the current expectation value requires a much higher resolution in ϕ. As we observed in Sec. 4.4.2, the hybrid Löwdin perturbation theory estimates the energies of the states near the edge of the A subspace with a low precision. This is why the contribution of the bound states to L_J^{-1} disagrees with the derivative of the bound state contribution to the current shown in Fig. 4.2. Nevertheless, because this error cancels with the B subspace contribution, the precision of the full result remains the same.

The zero temperature limit is the most computationally expensive both to pure KPM and imaginary energy integration [22, 23]. Computing the finite temperature results within hybrid KPM, however, amounts to replacing f with the Fermi function at the correct temperature. Because the computational cost of hybrid KPM is dominated by the computation of the KPM moments and the perturbation expansion of low-lying states, the extra computational cost of a temperature sweep is negligible.

4.5.2. EFFECTIVE DOUBLE QUANTUM DOT HAMILTONIAN

Turning to the hybrid Löwdin perturbation theory, we apply hybrid KPM to calculate an effective Hamiltonian of several low energy states in a double quantum dot system. In order to use the basis of individual quantum dot states, we start with a system with decoupled dots and include hoppings between the dots perturbatively. When the tunnel barrier between the dots is low, the eigenstates become strongly hybridized, so that

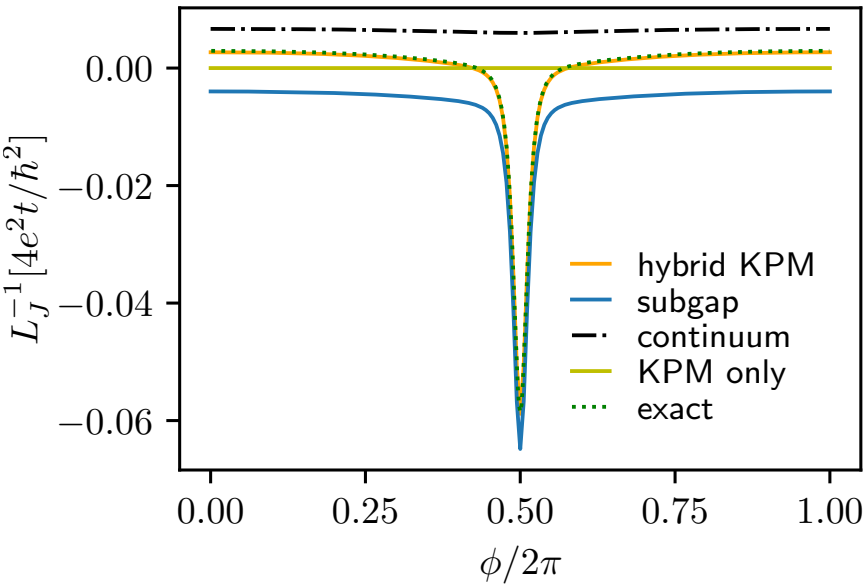

Figure 4.3: Inverse Josephson inductance as a function of the superconducting phase difference. The orange line represents L_J^{-1} calculated with hybrid KPM, whereas the blue and black lines show the corresponding contributions from subgap and continuum states respectively. The hybrid KPM result agrees with the exact result using full diagonalization, while the pure KPM result vanishes.

the perturbation theory requires a sufficiently high order in the inter-dot coupling. We address this need by including the eigenfunctions and eigenenergies of the lowest few bound states exactly and treating the remaining part of the energy spectrum up to third order in the Löwdin perturbation theory using hybrid KPM approach.

We consider two gate-defined quantum dots formed in a quantum well with the interdot tunnel coupling and dot chemical potential controlled by the gate electrodes. In the continuum approximation the quantum well Hamiltonian is

$$H_{2D} = \frac{\hbar^2}{2m_e}(k_x^2 + k_y^2) + V(x, y), \tag{4.36}$$

where m_e is the effective electron mass, k_x and k_y are the components of the electron wave vector, and $V(x, y)$ is the electrostatic potential. We discretize the continuum Hamiltonian H_{2D} using the finite difference approximation on a square lattice with a lattice constant of 5 nm and the effective mass of GaAs. We consider the gate geometry of Ref. [13], with the gate electrodes 60 nm above the quantum well. Plunger gates control the dot chemical potential, while the tunnel barrier height between the dots is controlled by the barrier gate in the middle, as shown in Fig. 4.4. We calculate the electrostatic potential induced in the quantum well using the approximation of Ref. [24]. In the initial configuration the gate potentials form two tunnel-coupled quantum dots, as shown in Fig. 4.4.

We separate the Hamiltonian into a sum of unperturbed H_0 term and two perturbation

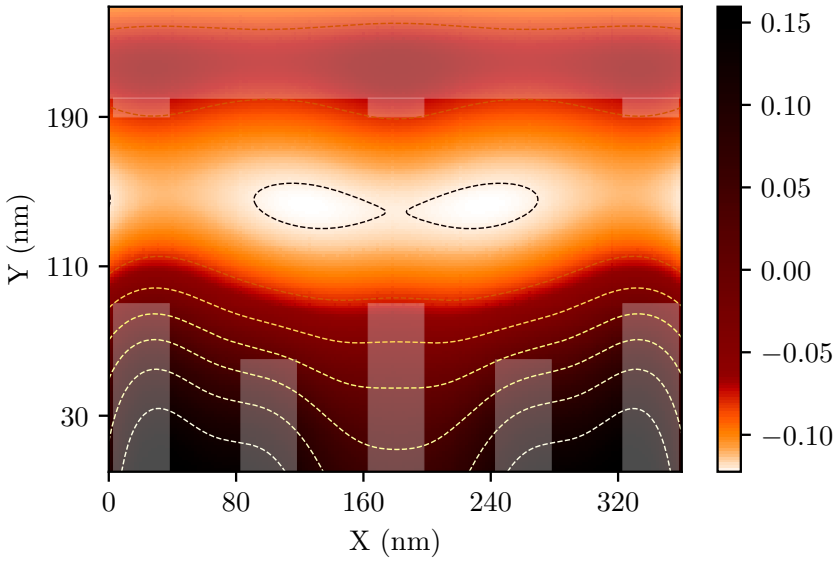

Figure 4.4: The 2DEG electrostatic potential superimposed with gate electrodes deposited on top of the GaAs heterostructure. We use the gate design and heterostructure from [13]. Plunger and barrier gates are shown at the bottom and screening gates at the top. By applying negative voltage to the gate electrodes, we locally deplete the 2DEG to form two quantum dots as represented by the equipotential lines.

terms:

$$H = H_0 + \lambda_g \Delta H_g + \lambda_c H_c. \tag{4.37}$$

Here H_0 is the initial Hamiltonian with the hoppings between the left and the right halves of the system removed, ΔH_g is the deviation of the gate potential from the initial setting, and H_c is the hoppings connecting the left and right halves. We split the spectrum of the Hamiltonian into two subspaces: A contains the two lowest bound states in each quantum dot, and B the rest of the energy spectrum. We obtain the states in A and a few states in $B_e \subset B$ with the lowest energies using sparse diagonalization. Setting $\lambda_c = 1$ reproduces the original Hamiltonian without the cut between the dots. We select the perturbation ΔH_g as the potential resulting from an antisymmetric detuning of the plunger gates by $\pm\Delta V/2$. In Fig. 4.5, we compare the eigenenergies calculated from the effective model using first and third order perturbation theory with the sparse diagonalization results. The first order perturbation does not require hybrid KPM and coincides with conventional first order perturbation theory. It cannot, however, accurately estimate the spectrum, while third order Löwdin perturbation theory using hybrid KPM shows a good agreement with the exact result.

4.5.3. EFFECTIVE BAND STRUCTURES

Semiconductor nanowires, besides many potential applications [14], are of interest as a platform to realize Majorana states when proximitized with a superconductor [15–17]. The necessary ingredients for the creation of Majorana states are spin-orbit interaction

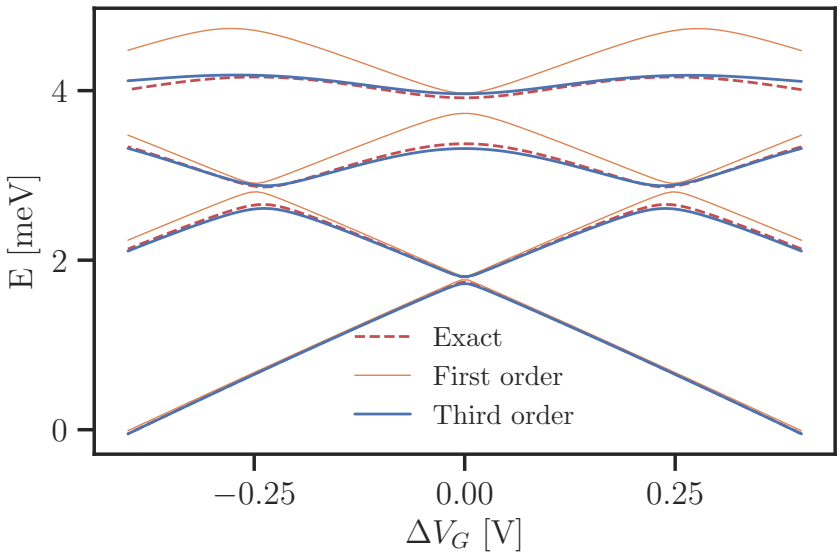

Figure 4.5: Energy spectrum as a function of gate voltage difference between the two dots. Eigenenergies calculated from the first and third order effective models are compared against the exact energies.

and external magnetic field, which remove spin degeneracy in the lowest subband of the wire, resulting in effective p-wave superconducting pairing. In an external electric field normal to the wire the bulk spin-orbit coupling of the semiconductor results in Rashba spin-orbit interaction. The minimal model describing the relevent phenomena, with the exception of superconductivity, is the 2-band effective model:

$$H = \frac{\hbar^2}{2m^*} k_z^2 + \mu + \alpha k_z \left(\sigma_y E_x + \sigma_x E_y\right) + \mu_B \mathbf{B} g \boldsymbol{\sigma}, \tag{4.38}$$

where m^* is the effective mass of the lowest subband, k_z is the momentum along the wire, μ is the chemical potential, E_x and E_y are components of the electric field, $\boldsymbol{\sigma}$ are the Pauli matrices and α is the strength of the Rashba spin-orbit interaction. The external magnetic field is $\mathbf{B}$, μ_B is the Bohr-magneton and g is the effective g-factor tensor in the lowest subband. While this simple model is easy to solve, extracting the parameters of realistic setups starting from a microscopic model is computationally hard. We solve this task using hybrid KPM.

We start from the 8-band $\mathbf{k}\cdot\mathbf{p}$ model of bulk zinc-blende materials, in particular InAs [4, 19, 25, 26]. This continuum model accurately captures the s-type conduction and p-type valence bands near the Fermi level at small momenta, up to second order in k. We consider an infinite wire oriented along the z-axis with approximately circular cross-section in the xy plane with radius R. We discretize the $\mathbf{k}\cdot\mathbf{p}$ Hamiltonian in the xy-plane by replacing momenta k_x and k_y (but not k_z) with discrete spatial derivatives. We include the Zeeman term with the bulk g-factor $g^* = -15$ of InAs [4, 27]. We introduce the orbital magnetic field using Peierls substitution, as well as the electrostatic potential

$V = -E_x x - E_y y$. For this example we use radius $R = 25\,\text{nm}$ with discretization grid lattice constant $a = 1\,\text{nm}$. This results in a tight-binding model with 31056 degrees of freedom, outside of the practical limits of full diagonalization on a single computer.

We use the Löwdin algorithm treating the tight binding Hamiltonian with vanishing external fields and $k_z = 0$ as the unperturbed Hamiltonian, and include perturbations up to second order in k_z and the electric field, and up to linear order in the magnetic field. Using second order perturbation theory, we obtain the effective model of the form (4.38) with $m^* = 0.023 m_0$, $\alpha = 2.67\,\text{nm}^2$, $\mu = 0.43\,\text{eV}$, $g_{xx} = g_{yy} = -15.4$ and $g_{zz} = -15.5$, with m_0 the free electron mass and all other terms approximately vanishing. This perturbative treatment, only accurate at small parameter values, does not capture the overall energy shift of the subbands resulting from the electrostatic field at field strengths relevant to experiments. Hence, we also construct the effective model using $E_{x0} = 10\,\text{meV/nm}$ as the unperturbed Hamiltonian. The resulting spectrum at finite k_z and B_z agrees with the exact eigenenergies of the full model as illustrated in Fig. 4.6.

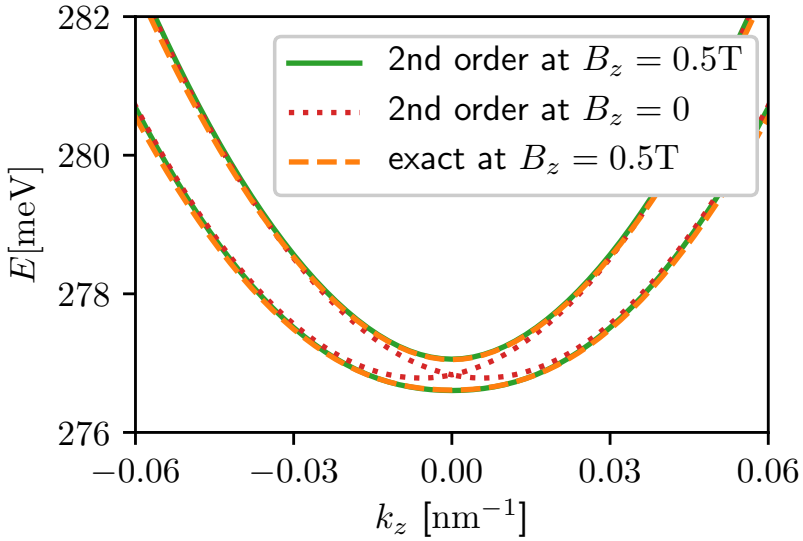

Figure 4.6: Energy spectrum of the lowest subband of an InAs nanowire of radius 5 nm. The plot shows the exact result from sparse diagonalization with $B_z = 0.5\,\text{T}$ and $E_x = 10\,\text{meV/nm}$, and the perturbation theory result around $E_{x0} = 10\,\text{meV/nm}$ at 2nd order at $B_z = 0$ and $B_z = 0.5\,\text{T}$.

4.6. CONCLUSIONS

We developed the hybrid kernel polynomial method, where we combine the strengths of KPM in treating many states at a low energy resolution and of sparse diagonalization in treating few states with high accuracy. We applied this method to the problems of accurate calculation of expectation values, perturbation theory of thermodynamic quantities and construction of perturbative effective models. The source code of these general and

reusable algorithms is available at [28], together with the source code and data of the examples showcased in the manuscript.

We applied our method to several active research topics in condensed matter and mesoscopic physics: calculation of supercurrent and inductance in a Josephson junction, design of spin qubits defined in a two dimensional electron gas, and the calculation of the effective band structure in a realistic model of a semiconductor nanowire. Our examples illustrate how the combination of low and high resolutions enables the investigation of response functions and effective models in systems whose size would make this prohibitively expensive using other approaches.

We did not yet address the following relevant questions:

- What is the optimal way to choose the number of the exactly calculated states and the number of moments in hybrid KPM to minimize the computational effort required for given precision?
- How quickly does the stochastic trace approximation converge in the perturbative KPM scheme?
- What is the general form of rearranged equations similar to (4.29) for higher orders and multiple perturbation parameters?
- How does the efficiency of our method compare to other recursive numerical approaches to perturbation theory, such as Ref. [29]?

These we leave to future work.

Because our method allows treatment of Hilbert spaces up to millions of degrees of freedom, we expect it to be useful in treating interacting quantum mechanical problems. We conjecture that the hybrid approach will also improve KPM-assisted self-consistent mean-field [30] and density matrix renormalization group [31, 32] calculations. Accurate simulation of nanoelectronic devices with truncated few-electron Hilbert spaces is also a promising future direction of research using this methodology.

4.7. APPENDIX

4.7.1. CHEBYSHEV POLYNOMIAL EXPANSION OF SELECTED FUNCTIONS

We explicitly give the expansion of a few common functions used in condensed-matter physics and this manuscript: Dirac delta function (used in spectral densities):

$$\delta\left(E-\hat{H}\right)=\frac{1}{\pi\sqrt{1-E^2}}\sum_m\frac{2}{1+\delta_{m,0}}T_m(E)\,T_m(\hat{H}). \tag{4.39}$$

The Green's functions:

$$G^{\pm}(E,\hat{H})=\lim_{\eta\to 0^+}\frac{1}{E-\hat{H}\pm\eta i}=\mp\frac{2\,i}{\sqrt{1-E^2}}\sum_m\frac{1}{1+\delta_{m,0}}\exp\left(\pm i\,m\arccos(E)\right)T_m(\hat{H}). \tag{4.40}$$

4.7.2. DETAILS OF LÖWDIN EXPANSION

We adapt this section from Refs. [19] and [33], that closely follows the derivation of arbitrary order quasi-degenerate perturbation theory in Ref. [4]. The goal is to find a unitary basis transformation (Schrieffer–Wolff transformation) with skew-Hermitian matrix S ($S^\dagger = -S$) as

$$\tilde{H} = e^{-S} H e^{S}, \tag{4.41}$$

such that the transformed Hamiltonian $\tilde{H}$ does not couple the A and B subspaces. The transformation should be the identity when the perturbation vanishes and we expand S as a series in successive orders of the perturbation

$$S = \sum_{j=1}^{\infty} \lambda^j S^{(j)}. \tag{4.42}$$

The transformed Hamiltonian (using the Baker-Campbell-Hausdorff formula) is

$$\tilde{H} = \sum_{j=0}^{\infty} \frac{1}{j!} [H, S]^{(j)} = \sum_{j=0}^{\infty} \frac{1}{j!} [H_0 + \lambda H'_d, S]^{(j)} + \sum_{j=0}^{\infty} \frac{1}{j!} [\lambda H'_n, S]^{(j)}, \tag{4.43}$$

where the nested commutator $[A, B]^{(j)}$ is defined as

$$[A, B]^{(j)} = [\ldots[[A, \underbrace{B], B], \ldots, B}_{j \text{ times}}], \tag{4.44}$$

with commutator $[A, B] = AB - BA$ and we split the perturbation into block-diagonal and block off-diagonal parts as $H' = H'_d + H'_n$ with with $\left(H'_d\right)_{AB} = \left(H'_d\right)_{BA} = \left(H'_n\right)_{AA} = \left(H'_n\right)_{BB} = 0$ (X_{AB} denotes the restriction of operator X to the AB block). The requirement on the S we seek is $\tilde{H}_{AB} = \tilde{H}_{BA} = 0$ and we call $\tilde{H}_{AA}$ the effective Hamiltonian. We choose S to be block off-diagonal such that $S_{AA} = S_{BB} = 0$, this removes arbitrary unitary transformations within the A and B subspaces from the result.

To do n'th order perturbation theory we demand the equations to be satisfied for all terms up to λ^n. Separating terms that contribute to diagonal and off-diagonal terms ($\tilde{H} = \tilde{H}_d + \tilde{H}_n$ with $\left(\tilde{H}_d\right)_{AB} = \left(\tilde{H}_d\right)_{BA} = \left(\tilde{H}_n\right)_{AA} = \left(\tilde{H}_n\right)_{BB} = 0$) we find:

$$\tilde{H}_d = \sum_{j=0}^{\infty} \frac{1}{(2j)!} [H_0 + \lambda H'_d, S]^{(2j)} + \sum_{j=0}^{\infty} \frac{1}{(2j+1)!} [\lambda H'_n, S]^{(2j+1)}, \tag{4.45a}$$

$$\tilde{H}_n = \sum_{j=0}^{\infty} \frac{1}{(2j+1)!} [H_0 + \lambda H'_d, S]^{(2j+1)} + \sum_{j=0}^{\infty} \frac{1}{(2j)!} [\lambda H'_n, S]^{(2j)}. \tag{4.45b}$$

Our goal is to recursively find $S^{(n)}$ form the lower orders $S^{(j)}$ for $j \in [1 \ldots n-1]$. We solve $\tilde{H}_n = 0$ up to n'th order by inserting the expansion $S = \sum_{j=1}^{n} \lambda^j S^{(j)}$ into (4.45b) and letting the sums in j run to $\lfloor (n-1)/2 \rfloor$, this produces all terms up to n'th order. We observe that at n'th order $S^{(n)}$ only appears in a single commutator, allowing to rearrange the n'th order terms in the equation $\tilde{H}_n = 0$ as

$$[H_0, S^{(n)}] = Y^{(n)} \tag{4.46}$$

where $Y^{(n)}$ only depends on lower orders of S. We generate the Y's using symbolic computer algebra. The first few terms are:

$$[H_0, S^{(1)}] = Y^{(1)} = -H'_n, \tag{4.47a}$$

$$[H_0, S^{(2)}] = Y^{(2)} = -[H'_d, S^{(1)}], \tag{4.47b}$$

$$[H_0, S^{(3)}] = Y^{(3)} = -[H'_d, S^{(2)}] - \frac{1}{3}[[H'_n, S^{(1)}], S^{(1)}]. \tag{4.47c}$$

As the Y's are purely off-diagonal Hermitian, it is possible to write only $Y^{(n)}_{AB}$ in terms of S_{AB}, S_{BA} and the restricted components of H.

The equations (4.47) can be iteratively solved as

$$S^{(j)}_{ml} = \frac{Y^{(j)}_{ml}}{E_m - E_l} \tag{4.48}$$

where indices m and l correspond to states in the A and B subspace respectively. With the $n-1$ order expansion of S at hand, we substitute it into (4.45a) with the sum over j running to $\lfloor n/2 \rfloor$, or directly into (4.43) with the sum over j running to n, to produce $\tilde{H}_d$ up to n'th order.

The same algorithm works in the case of multiple expansion parameters by replacing $\lambda H'$ with $\sum_\alpha \lambda_\alpha H'_\alpha$ and only keeping track of terms with total power j in the λ_α in $S^{(j)}$ and $Y^{(j)}$. Finally, we write the AA block of the transformed Hamiltonian as a sum of successive orders of the perturbation to obtain the effective Hamiltonian:

$$H_{\text{eff}} = \tilde{H}^{(0)} + \sum_\alpha \lambda_\alpha \tilde{H}^{(1,\alpha)} + \sum_{\alpha\beta} \lambda_\alpha \lambda_\beta \tilde{H}^{(2,\alpha\beta)} + \dots. \tag{4.49}$$

4.7.3. USING KPM IN HIGHER ORDER LÖWDIN EXPANSION

To use KPM efficiently, we want to avoid using an explicit basis for the B subspace. We observe that the expressions (4.47) for Y and (4.45a) for $\tilde{H}_{AA}$ can be expanded in terms of the restricted operators (i.e. H'_{AA}, H'_{AB}, etc.). Whenever two terms with A indices are adjacent, we may insert a projector onto the A states $P_A = \sum_m |m\rangle\langle m|$ with a full basis of A states $|m\rangle$. Whenever two terms with B indices are adjacent, we insert a projector onto the B subspace $P_B = \mathbb{1} - \sum_m |m\rangle\langle m|$. This allows to remove the restriction from one of the adjecent terms, for example

$$\langle m|S_{AB} H'_{BB} S_{BA}|m'\rangle = \langle m|P_A S P_B P_B H' P_B P_B S P_A|m'\rangle = \langle m|SH'S|m'\rangle = \sum_{ij} S_{mi} H'_{ij} S_{jm'} \tag{4.50}$$

where we used that S is only nonzero in the off-diagonal blocks. This allows to only store the mixed matrix elements $S_{mi} = \langle m|S|i\rangle$ where $|i\rangle$ is the original basis where the Hamiltonian is sparse with indices i, j running over the full Hilbert space, and $|m\rangle$ is the basis of the A subspace. In this basis $\sum_i S_{mi} (P_B)_{ij} = S_{mj}$, similarly for block off-diagonal matrices. It is possible to replace all H_{BB} terms with H because there is only one H in every product, all the other terms are S's. This is advantageous as H' acting on the full Hilbert space of size N can be represented as a sparse matrix of $\mathcal{O}(N)$ nonzero entries,

while S_{mi} and other off-diagonal components can be stored as small dense matrices with $\mathcal{O}(Na)$ entries where $a = \dim(A)$.

Now we rewrite (4.48) in terms of the Green's function:

$$S^{(n)}_{mi} = \sum_j Y^{(n)}_{mj} \left(\frac{1}{E_m - H_0} \right)_{ji} = \sum_j \left[G_0(E_m)_{ij} \left(Y^{(n)\dagger} \right)_{jm} \right]^\dagger \tag{4.51}$$

where we used that Y is block off-diagonal and $G_0(E)$ does not mix the A and B subspaces. For numerical stability reasons, we still apply P_B from the right in practice. Following the procedure outlined in Appendix 4.7.2 we successively generate all S terms and produce $\tilde{H}_{AA}$, the only difference is using the above basis convention.

The computational complexity of generating the n'th order effective Hamiltonian (in the case of a single small parameter) is $\mathcal{O}(n^2 aNM)$, where M is the number of KPM moments, practically chosen to be at the order of bandwidth/gap. We obtain this estimate by the following reasoning: A single evaluation of the KPM Green's function on a vector costs $\mathcal{O}(NM)$. To get $S^{(j)}$, we need to apply G to (aj) vectors on the right hand side, as $Y^{(j)}$ is a j'th order polynomial of the small parameter. We argue that the KPM step is the costliest part of the procedure, because evaluation of Y and $\tilde{H}$ only involves products of small or sparse matrices.

There is, however, a combinatorial factor in the number of terms involved in these expressions, which grows exponentially with j. At high orders $Y^{(n)}$ contains $\mathcal{O}(2^n)$ terms with a single small parameter. At high enough orders, it is more efficient to directly evaluate the commutator series giving $Y^{(n)}$ by substituting the $n-1$ order expansion of S with numerical coefficients. Truncating to terms of at most order n after every multiplication, this only takes $\mathcal{O}(n^3)$ time. Hence, this latter method becomes more efficient for high enough orders. Combinatorial factors are even larger if there are multiple small parameters in the expansion. We defer further analysis of the complexity and possible optimizations of high order expansions.

REFERENCES

[1] P.-O. Löwdin, *A note on the quantum-mechanical perturbation theory,* J. Chem. Phys. **19**, 1396 (1951).

[2] J. R. Schrieffer and P. A. Wolff, *Relation between the Anderson and Kondo Hamiltonians,* Phys. Rev. **149**, 491 (1966).

[3] J. M. Luttinger and W. Kohn, *Motion of electrons and holes in perturbed periodic fields,* Phys Rev **97**, 869–883 (1955).

[4] R. Winkler, *Spin-Orbit Coupling Effects in Two-Dimensional Electron and Hole Systems* (Springer, Berlin, Heidelberg, 2003).

[5] Y. Saad, *Iterative Methods for Sparse Linear Systems*, 2nd ed. (Society for Industrial and Applied Mathematics, Philadelphia, PA, USA, 2003).

[6] R. Lehoucq, D. Sorensen, and C. Yang, *ARPACK users' guide: Solution of large scale eigenvalue problems with implicitly restarted Arnoldi methods.* Software Environ. Tools **6** (1997).

[7] P. R. Amestoy, I. S. Duff, J. Koster, and J.-Y. L'Excellent, *A fully asynchronous multifrontal solver using distributed dynamic scheduling,* SIAM Journal on Matrix Analysis and Applications **23**, 15 (2001).

[8] P. R. Amestoy, A. Guermouche, J.-Y. L'Excellent, and S. Pralet, *Hybrid scheduling for the parallel solution of linear systems,* Parallel Computing **32**, 136 (2006).

[9] A. Weiße, G. Wellein, A. Alvermann, and H. Fehske, *The kernel polynomial method,* Reviews of Modern Physics **78**, 275 (2006).

[10] B. D. Josephson, *Possible new effects in superconductive tunnelling,* Physics Letters **1**, 251 (1962).

[11] K. K. Likharev, *Superconducting weak links,* Rev. Mod. Phys. **51**, 101 (1979).

[12] A. A. Golubov, M. Y. Kupriyanov, and E. Il'ichev, *The current-phase relation in Josephson junctions,* Rev. Mod. Phys. **76**, 411 (2004).

[13] P. Barthelemy and L. M. K. Vandersypen, *Quantum dot systems: a versatile platform for quantum simulations,* Annalen der Physik **525** (2013).

[14] P. Yang, R. Yan, and M. Fardy, *Semiconductor nanowire: What's next?* Nano Letters **10**, 1529 (2010).

[15] R. M. Lutchyn, J. D. Sau, and S. Das Sarma, *Majorana fermions and a topological phase transition in semiconductor-superconductor heterostructures,* Phys. Rev. Lett. **105**, 077001 (2010).

[16] Y. Oreg, G. Refael, and F. von Oppen, *Helical liquids and Majorana bound states in quantum wires,* Phys. Rev. Lett. **105**, 177002 (2010).

[17] V. Mourik, K. Zuo, S. M. Frolov, S. R. Plissard, E. P. A. M. Bakkers, and L. P. Kouwenhoven, *Signatures of Majorana fermions in hybrid superconductor-semiconductor nanowire devices,* Science **336**, 1003 (2012).

[18] A. Ferreira and E. R. Mucciolo, *Critical delocalization of chiral zero energy modes in graphene,* Phys. Rev. Lett. **115**, 106601 (2015).

[19] R. Skolasinski, D. I. Pikulin, J. Alicea, and M. Wimmer, *Robust helical edge transport in quantum spin Hall quantum wells,* Phys. Rev. B **98**, 201404 (2018).

[20] C. Ishii, *Josephson currents through junctions with normal metal barriers,* Prog Theor Phys **44**, 1525 (1970).

[21] C. W. Groth, M. Wimmer, A. R. Akhmerov, and X. Waintal, *Kwant: a software package for quantum transport,* New Journal of Physics **16**, 063065 (2014).

[22] V. P. Ostroukh, B. Baxevanis, A. R. Akhmerov, and C. W. J. Beenakker, *Two-dimensional Josephson vortex lattice and anomalously slow decay of the Fraunhofer oscillations in a ballistic SNS junction with a warped Fermi surface,* Phys. Rev. B **94**, 094514 (2016).

[23] K. Zuo, V. Mourik, D. B. Szombati, B. Nijholt, D. J. van Woerkom, A. Geresdi, J. Chen, V. P. Ostroukh, A. R. Akhmerov, S. R. Plissard, D. Car, E. P. A. M. Bakkers, D. I. Pikulin, L. P. Kouwenhoven, and S. M. Frolov, *Supercurrent interference in few-mode nanowire Josephson junctions,* Phys. Rev. Lett. **119**, 187704 (2017).

[24] J. H. Davies, I. A. Larkin, and E. V. Sukhorukov, *Modeling the patterned two-dimensional electron gas: Electrostatics,* Journal of Applied Physics **77**, 4504 (1995).

[25] E. Kane, *Band structure of indium antimonide,* Journal of Physics and Chemistry of Solids **1**, 249 (1957).

[26] B. A. Foreman, *Elimination of spurious solutions from eight-band* $\mathbf{k}\cdot\mathbf{p}$ *theory,* Phys. Rev. B **56**, R12748 (1997).

[27] C. R. Pidgeon, D. L. Mitchell, and R. N. Brown, *Interband magnetoabsorption in InAs and InSb,* Phys. Rev. **154**, 737 (1967).

[28] M. Irfan, S. R. Kuppuswamy, D. Varjas, P. M. Perez-Piskunow, M. Wimmer, and A. R. Akhmerov, *Hybrid kernel polynomial method,* zenodo.3450544 (2019).

[29] A. M. N. Niklasson and M. Challacombe, *Density matrix perturbation theory,* Phys. Rev. Lett. **92**, 193001 (2004).

[30] Y. Nagai, Y. Ota, and M. Machida, *Efficient numerical self-consistent mean-field approach for fermionic many-body systems by polynomial expansion on spectral density,* Journal of the Physical Society of Japan **81**, 024710 (2012).

[31] A. Holzner, A. Weichselbaum, I. P. McCulloch, U. Schollwöck, and J. von Delft, *Chebyshev matrix product state approach for spectral functions,* Phys. Rev. B **83**, 195115 (2011).

[32] A. Braun and P. Schmitteckert, *Numerical evaluation of Green's functions based on the Chebyshev expansion,* Phys. Rev. B **90**, 165112 (2014).

[33] R. J. Skolasinski, *Topology, Magnetism, and Spin-Orbit: A Band Structure Study of Semiconducting Nanodevices* (Casimir PhD Series, Delft-Leiden, 2018).

5

CRITICAL CURRENT PLATEAU OF GRAPHENE JOSEPHSON JUNCTIONS IN AN IN-PLANE MAGNETIC FIELD

5.1. INTRODUCTION

The reflection of electrons into holes and vice versa at the normal-metal–superconductor interface leads to the formation of Andreev bound states in superconductor–normal-metal–superconductor Josephson junctions [1]. Because these bound states are superpositions of particles with different charge, they carry supercurrent without particle current [2, 3]. Macroscopic coherence of superconductors makes the contributions of multiple Andreev states add, resulting in a large current compared to a persistent current of a mesoscopic ring [4, 5].

Breaking time-reversal symmetry by an external magnetic field, randomizes the contribution of individual states and strongly suppresses the supercurrent [3, 6]. The orbital effects of a perpendicular magnetic field in two-dimensional electron gas [7] or graphene Josephson [8] junction alone strongly suppress the critical current and produce the well know Fraunhofer pattern. Also, in a quasi-one-dimensional geometry, such as a nanowire Josephson junction, the critical current oscillates as a function of the Zeeman field [9], with the superconducting phase difference at which the ground state energy is minimal switching between 0 and π. Similarly, a combination of the Zeeman effect and the orbital effect of the magnetic field suppresses the critical current in a multimode nanowire Josephson junctions [10]. In superconductor–ferromagnet–superconductor graphene junction the suppression of the critical current is exponential, unless the triple pairing is enabled by the spin-orbit coupling [11].

We demonstrate that graphene Josephson junctions [8, 12, 13] are uniquely suitable to avoid all the mechanisms suppressing the critical current in magnetic field. Firstly, unlike many semiconductors, graphene has a negligible spin-orbit coupling [14, 15], and a g-factor of free electrons. Therefore a combination of graphene with a thin film of a superconductor with a negligible spin-orbit coupling—such as aluminum—allows to create Josephson junctions where the Zeeman field is homogeneous (due to the superconductor being fully penetrated by magnetic field), and spin-orbit coupling is absent. Because graphene is atomically flat, an in-plane magnetic field exerts no orbital effect. As a result, the only consequence of an in-plane magnetic field is a constant Zeeman splitting of all the Andreev states. A pair of spin-degenerate Andreev states at an energy $E(\chi)$ below the Fermi level with χ the superconducting phase difference carries a supercurrent $\frac{4e}{\hbar}\frac{dE}{d\chi}$ at zero temperature. Due to the g-factor being homogeneous, a Zeeman field E_Z splits these two states into $E(\chi) \pm E_Z$. As long as both spin-split levels stay below the Fermi level, they therefore carry the same critical current.

The critical value of the Zeeman energy up to which the critical current remains constant depends on junction details. We demonstrate that in short diffusive Josephson junctions, the critical current has a universal form as a function of the magnetic field. The bulk superconducting gap then becomes the only energy scale determining the suppression of the critical current. In long Josephson junctions, the junction Thouless energy, which is much smaller than the bulk superconducting gap, determines the size of the critical current plateau. We also analyze the mechanisms suppressing the supercurrent plateau. At a finite temperature, the contributions of low energy Andreev states to supercurrent become energy-dependent through their Fermi weight. Induced Rashba spin-orbit coupling in graphene [16–18] breaks the conservation of the quasiparticle spin, and therefore makes the energies of Andreev levels depend on the E_Z in a more complex

manner.

The organization of this chapter is as follows. First, we introduce the physical system and describe the method used to calculate supercurrent in Sec. 5.2. In Sec. 5.3, we present our results for the system in short and long Josephson junction regimes along with the effects of temperature and spin-orbit coupling. We present conclusions and a summary of our results in Sec. 5.4.

5.2. SYSTEM AND FORMALISM

We consider a planar superconductor–graphene–superconductor Josephson junction of width W, normal region length L_N, and superconducting contact length L_S as shown in Fig. (5.1). To calculate the Andreev spectrum and the supercurrent in this device, we use the tight-binding Hamiltonian

$$H = -t\sum_{i,j,s} a^{\dagger}_{is}a_{js} - \sum_{i,s}\mu_i a^{\dagger}_{is}a_{is} + E_Z\sum_{i,s,s'} a^{\dagger}_{is}\sigma_x a_{is'} \\ + i\alpha\sum_{i,j,s,s'} a^{\dagger}_{is}(\vec{\sigma}\times\vec{d}_{ij})_z a_{js'} + \sum_i \Delta_i a^{\dagger}_{i\uparrow}a^{\dagger}_{i\downarrow} + h.c., \tag{5.1}$$

where $a^{\dagger}_{is}$ and a_{is} are the electron creation and annihilation operators at site i with spin $s \in \{\uparrow,\downarrow\}$, t is the nearest-neighbour tight-binding constant, μ_i is the chemical potential at site i with values μ_N and μ_S in the normal and superconducting regions respectively, E_Z is the Zeeman energy, α is the strength of Rashba spin-orbit coupling which is non-zero only in the normal region, and $\vec{d}_{ij}$ is a unit vector pointing from site j to site i. The Pauli matrices $\vec{\sigma}$ act on spin degree of freedom. The indices (i,j) represent the nearest-neighbor sites and (s,s') represent spin orientations $(\uparrow,\downarrow)$. The superconducting pairing potential is Δ_i, which for simplification in calculations, we consider a double step function with the value zero in the normal region and values $\Delta e^{i\chi_L}$ and $\Delta e^{i\chi_R}$ in the left and right superconducting leads, respectively. The superconducting phases in the left and the right leads are χ_L and χ_R. Finally, $h.c.$ denotes the Hermitian conjugate.

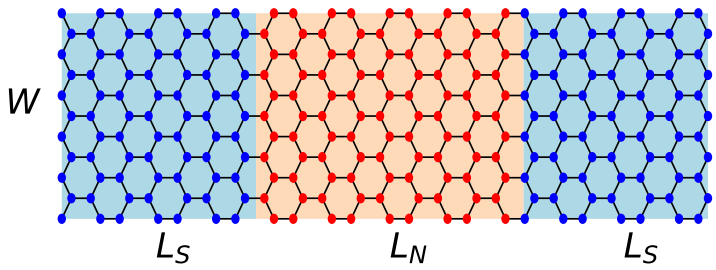

Figure 5.1: Schematic of a graphene Josephson junction of normal-region length L_N, width W, and superconducting contact length L_S.

In a Josephson junction, the supercurrent at zero temperature is given by the derivative of the negative energy Andreev states E_A with respect to the superconducting phase

difference $\chi = \chi_L - \chi_R$:

$$I = \frac{2e}{\hbar} \sum_{E_A<0} \frac{dE_A}{d\chi}, \tag{5.2}$$

with e the electron charge and $\hbar$ the reduced Planck's constant.

To calculate the supercurrent in the long junction regime, we use the hybrid kernel polynomial method [19], which combines a sparse diagonalization technique and the kernel polynomial method [20] to precisely calculate the thermodynamic properties of a mesoscopic system. We define the Hamiltonian (5.1) on a hexagonal lattice of lattice size a_{TB} using Kwant [21]. We calculate the subgap Andreev states using exact diagonalization and approximate the contribution of states above the gap using kernel polynomial method implemented in Kwant [21].

5.3. RESULTS

5.3.1. SHORT JUNCTION LIMIT

5

A Josephson junction is in the short-junction regime when the Thouless energy $E_{\text{Th}} = \hbar v_F / L_N$ (with v_F the Fermi velocity) is much larger than the superconducting gap Δ [2, 3]. In this regime, most of the Andreev bound state wave function weight lies in the superconducting region. This allows to treat the normal region as a point-like scatterer, and yields a universal Andreev state dispersion [22] as long as the time reversal symmetry is preserved:

$$E_A^{\pm} = \pm\Delta\sqrt{1 - T_i \sin^2(\chi/2)}, \tag{5.3}$$

with T_i eigenvalues of the transmission matrix of the normal region. The density of states above the superconducting gap does not vary with the superconducting phase difference, and therefore the subgap states are the only carrier of the supercurrent.

Here, we consider a single-mode Josephson junction such that $T_i = T$ in Eq. (5.3). At zero temperature, we only need Andreev state E_A^- below the Fermi level. An applied Zeeman field breaks the Kramers degeneracy [23] and moves the Andreev states by energy $\pm E_Z$:

$$E_{A,Z} = -(E_A^- \pm E_Z)\,\text{sgn}(E_A^- \pm E_Z). \tag{5.4}$$

The supercurrent (5.2) due to the Andreev states (5.3) at zero temperature equals

$$I_{\pm} = \frac{2e}{\hbar} \frac{\Delta^2 T \sin(\chi)}{2E_A^-} \left[(E_A^- \pm E_Z)\delta(E_Z \pm E_A^-) + \frac{1}{2}\,\text{sgn}(E_A^- \pm E_Z) \right], \tag{5.5}$$

with the total supercurrent $I = I_+ + I_-$. In Fig. 5.2(a), we show the Andreev bound state energies at zero and finite magnetic field for a transparent junction with $T \approx 1$ as well as the contribution of this pair of Andreev levels to the supercurrent. The supercurrent stays constant in the region where $E_A(\chi) > E_Z$, and therefore the critical current does not change until E_Z matches $E_A(\chi_{\max})$, with $\chi_{\max}$ the phase difference at which the supercurrent is critical $I = I_c$. When $T = 1$, $\chi_{\max} = \pi$, and $E_A(\chi_{\max}) = 0$, so that the critical

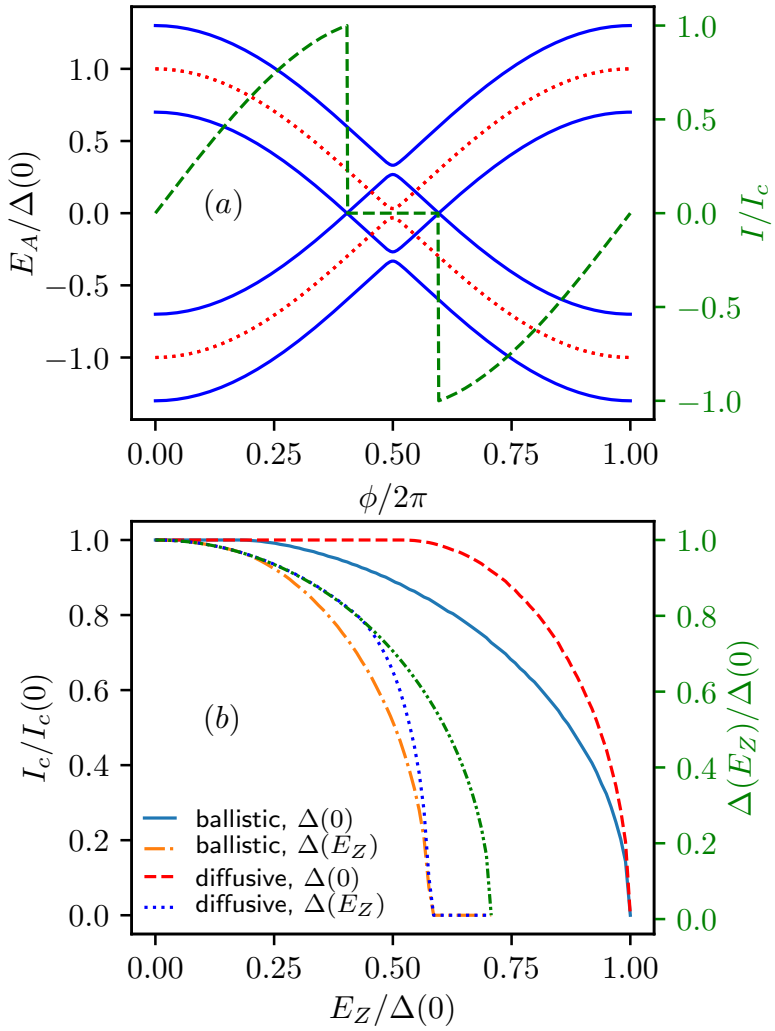

Figure 5.2: (a) Andreev bound state energies and current-phase relation in a short Josephson junction with transparency $T = 0.999$. In the absence of a Zeeman field, Andreev states are spin-degenerate (dotted curves), whereas a finite Zeeman field breaks the spin-degeneracy (solid curves) with the corresponding current-phase relation (broken curve). (b) Critical current and the superconducting gap as a function of the Zeeman energy in the short-junction regime. The solid-blue and broken-orange curves show the critical current for a ballistic device with the same transparency as in (a) using a constant and magnetic field dependent superconducting gap, respectively. The broken-red and dotted-blue curves show the critical current for a diffusive device using a constant and magnetic field dependent superconducting gap, respectively. The green line shows the magnetic field dependence of the superconducting gap.

current slowly drops with magnetic field [see Fig. 5.2(b)]. However, if the Josephson junction has lower transparency, then Andreev levels move higher in energy, in addition to $\chi_{\max}$ becomes smaller, so that a supercurrent plateau with a size $E_Z \lesssim \Delta$ appears.

In diffusive Josephson junctions, the transmission eigenvalues have the universal Kulik-Omelyanchuk distribution [3, 24]. To obtain the critical current in this regime, we integrate Eq. (5.3) over the probability distribution of transmission eigenvalues T:

$$E_A = -2\Delta \int_0^{\pi/2} \sqrt{1 - \sin^2(\chi/2)\sin^2 x}\, dx. \tag{5.6}$$

We show the critical current for a diffusive short-junction at zero temperature in Fig. 5.2(b), which shows a critical current plateau of size $E_Z \lesssim \Delta$ as discussed above.

Since the bulk superconducting gap determines the suppression of critical current in short Josephson junctions, we also consider its dependence on the magnetic field $\Delta = \Delta(0)\sqrt{1 - E_Z^2/E_{Z,c}^2}$. We show the field dependence of the gap for a critical Zeeman field [25] $E_{Z,c} = \Delta(0)/\sqrt{2}$ in Fig. 5.2(b). The critical current in a ballistic and diffusive Josephson junction with a field-dependent superconducting gap decreases faster with Zeeman energy but still requires magnetic field strength comparable to the critical magnetic field of the superconductor [see Fig. 5.2(b)].

5

5.3.2. LONG JUNCTION LIMIT

The physics of the Zeeman effect in graphene Josephson junctions becomes more varied in the long-junction limit [26, 27], where the energy of the lowest Andreev state is equal to the Thouless energy $E_{\mathrm{Th}} \ll \Delta$. Therefore, the Thouless energy of the junction determines the size of the critical current plateau. We first consider Josephson junctions of equal aspect ratio ($W/L_N = 1$) and show the critical current as a function of Zeeman energy in Fig. (5.3) for different values of the normal-region chemical potential μ_N. In such narrow Josephson junctions, the size of the critical current plateau weakly depends on the chemical potential because of the weak dependence of Thouless energy on chemical potential. We also observe subsequent critical current plateaus at higher values of the Zeeman field after the suppression of the first one. The current-phase relation undergoes a 0 to π transition when Andreev levels cross the Fermi level, which suppresses the critical current plateau. In a 0 to π current-phase transition, the critical current first decreases and then increases. Once it reaches the maximum value, it stays constant till the start of a π to 0 transition, which is again associated with Andreev level crossings at the Fermi level and depends on the complex Andreev band structure.

Next, we consider wide Josephson junctions ($W \gg L_N$) in the long-junction limit by imposing periodic boundary conditions in the y-direction. In such Josephson junctions, the lowest energy Andreev states correspond to trajectories traveling at grazing angles [28]. These trajectories determine the Thouless energy and the size of the critical current plateau. In Fig. (5.4), we show the critical current for a ballistic long and wide junction for different values of μ_N. Because the angle of the trajectories (which determines the lower bound of Thouless energy) depends on the chemical potential via the Fermi momentum and the velocity mismatch at the normal-metal–superconductor interface, the size of the plateau now depends on the chemical potential.

We have discussed the formation of the critical current plateau at zero temperature in response to an in-plane magnetic field. At finite temperature, the contributions of Andreev

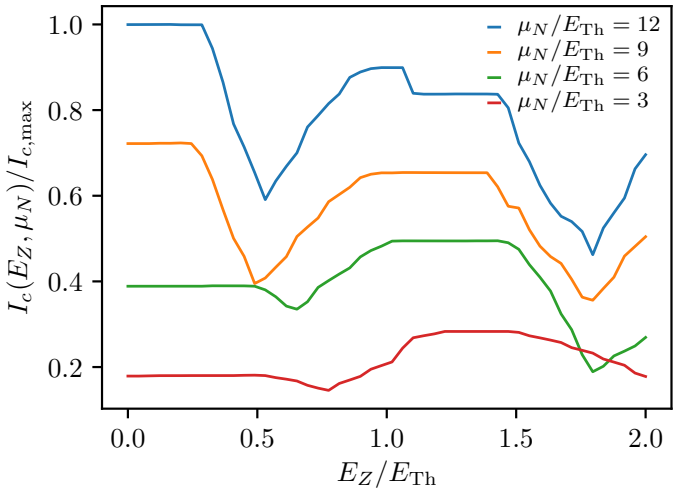

Figure 5.3: Critical current as a function of Zeeman energy for different values of the chemical potential in the normal region. We use a junction with an aspect ratio $W/L_N = 1$, the superconducting gap $\Delta \approx 6E_{\mathrm{Th}}$, and the chemical potential in the superconducting contacts $\mu_S \approx 40E_{\mathrm{Th}}$.

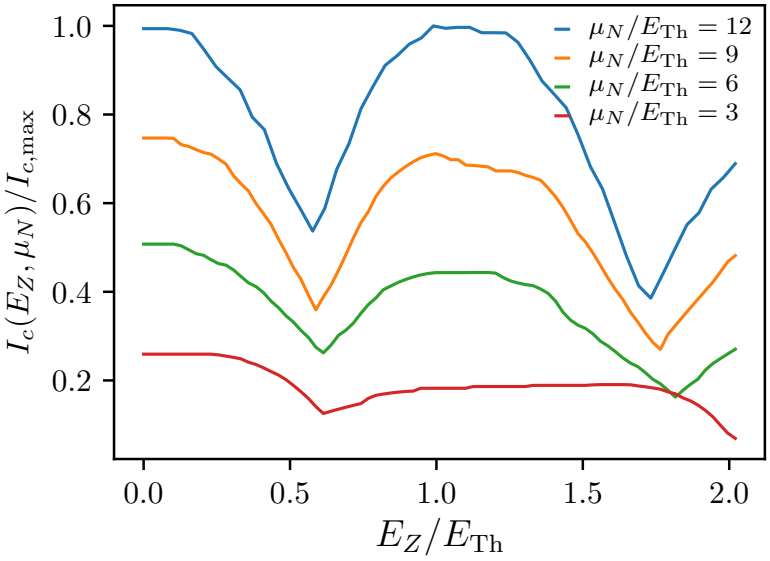

Figure 5.4: Critical current as a function of Zeeman energy for a wide Josephson junction. The rest of the parameters are the same as in Fig. 5.3.

states to supercurrent become energy-dependent through their Fermi weight (5.7):

$$f(E) = 1/\left(\exp(E/k_B T) + 1\right), \tag{5.7}$$

with k_B the Boltzmann constant and T the temperature. The supercurrent Eq. (5.2) takes

the form:

$$I = \frac{2e}{\hbar} \sum_A \frac{dE_A}{d\chi} f(E_A). \tag{5.8}$$

At zero temperature, the ground states are filled with unit occupation. This population

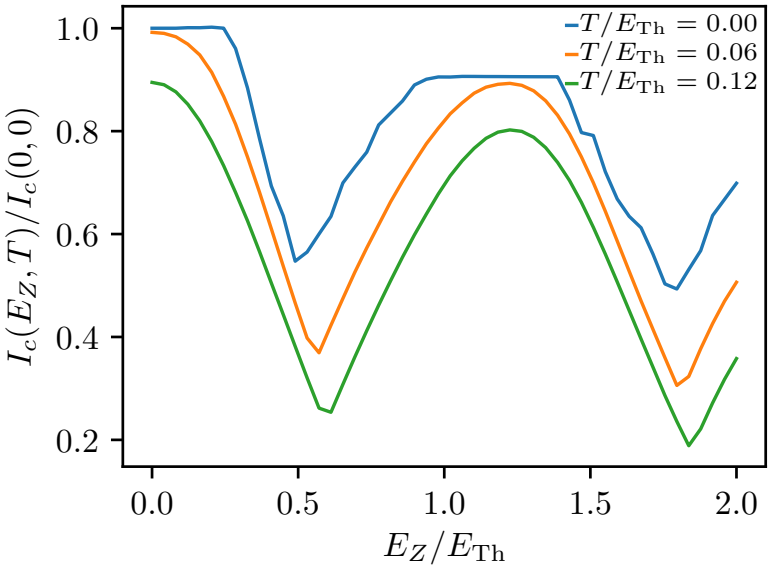

Figure 5.5: Critical current as a function of Zeeman energy for different values of temperature. The chemical potential in the normal region is $\mu_N = 9E_{\mathrm{Th}}$, while the rest of the parameters are the same as in Fig. 5.3.

changes at finite temperature with the occupation of states above the Fermi level. At finite temperature, the net supercurrent decreases because the direction of supercurrent due to Andreev states above the Fermi level is opposite to that of states below. At a given temperature, the Zeeman field further decreases the supercurrent, because it moves the Andreev levels in energy, which changes their occupation. With increasing magnetic field, the contributions of Andreev states to supercurrent due to states just above the Fermi level increases while decreasing the contribution of states just below. As a result, the critical current plateau is suppressed. In Fig. (5.5), we present the results of finite temperature showing the suppression of the critical current plateau. We argue that this kind of measurement allows to determine the contribution of low energy Andreev states to supercurrent. Here, we estimate how the lowest Andreev levels contribute to supercurrent at small magnetic field and low temperature. For a pair of Andreev states at finite Zeeman field below the Fermi level, the supercurrent is:

$$I_E(E_Z, T, \chi) = -\frac{I_E(0,0,\chi)}{2}\left[\tanh(\frac{E+E_Z}{2k_BT}) + \tanh(\frac{E-E_Z}{2k_BT})\right]. \tag{5.9}$$

The estimated change in critical current at low temperature is:

$$\delta I(E_Z, T, \chi) \approx I_c(0,0)\frac{I_E(E_Z, T, \chi)}{I_{E,c}(E_Z, T)}, \tag{5.10}$$

with $I_c(0,0)$ the critical current at zero temperature in the absence of magnetic field in Fig. (5.5). This formula is valid as far as the Andreev levels stay below the Fermi level and can be used to estimate how much critical current decreases as a function of the Zeeman field at finite temperature as compared to zero temperature critical current.

Finally, we analyze the effect of the Rashba spin-orbit coupling on the critical current plateau. Rashba spin-orbit coupling breaks the conservation of the quasiparticle spin. In Fig. 5.6, we show the critical current as a function of Zeeman energy for different values of the spin-orbit coupling parameter α. We show that if the size of the spin-orbit coupling energy is smaller than the plateau size and Zeeman energy is also lower, then the effect of spin-orbit coupling is negligible. However, when its strength is comparable to the Thouless energy, it suppresses the critical current plateau. This suppression of critical current plateau is a potential probing mechanism to quantify the strength of induced Rashba spin-orbit coupling in graphene-based Josephson junctions.

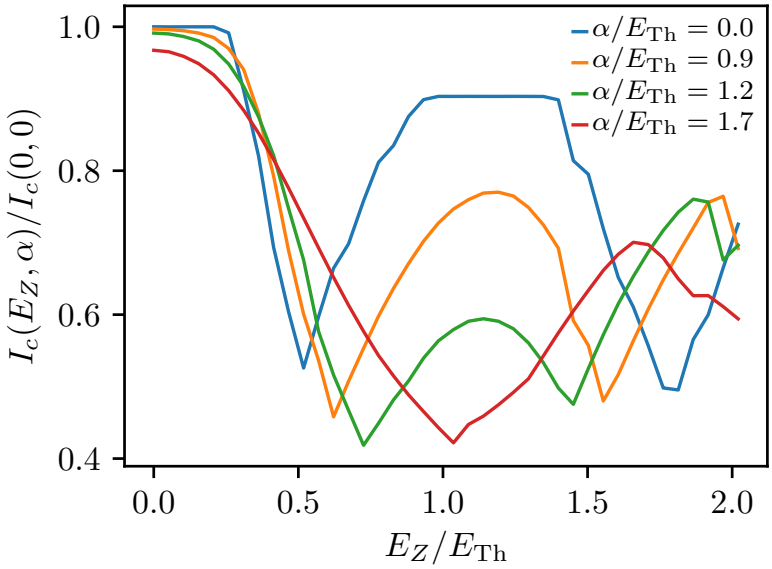

Figure 5.6: Critical current as a function of Zeeman energy at increasing values of the Rashba spin-orbit coupling. The chemical potential in the normal region is $\mu_N = 9E_{\mathrm{Th}}$, while the rest of the parameters are the same as in Fig. 5.3.

5.4. CONCLUSIONS

We have studied the effect of an in-plane magnetic field in planar graphene Josephson junctions. Because of the equal g-factor in graphene and thin-film superconducting contacts, negligible spin-orbit coupling, and absence of orbital effects of the magnetic field, graphene Josephson junctions avoid suppression of critical current to an in-plane magnetic field. As a result, a critical current plateau exists for a range of magnetic field determined by the junction detail. In the short-junction regime, the bulk superconducting gap determines the size of the plateau. We have shown that in short diffusive junctions, the

critical current has a universal form as a function of the magnetic field and the suppression of critical current requires a magnetic field comparable to the critical magnetic field of the superconductor. In the long-junction regime, the size of the critical current plateau is determined by the Thouless energy, which is much smaller than the bulk superconducting gap. Therefore, we need a much smaller magnetic field than the critical magnetic field of the superconductor to observe the effect. We have also discussed two mechanisms that destroy the critical current plateau, namely: finite temperature and Rashba spin-orbit coupling. We have shown that the suppression of the critical current plateau in the presence of finite temperature or Rashba spin-orbit coupling can be used to probe these two effects in graphene Josephson junctions.

REFERENCES

[1] A. F. Andreev, *The thermal conductivity of the intermediate state in superconductors,* Sov. Phys. JETP **19**, 1228 (1964).

[2] K. K. Likharev, *Superconducting weak links,* Rev. Mod. Phys. **51**, 101 (1979).

[3] A. A. Golubov, M. Y. Kupriyanov, and E. Il'ichev, *The current-phase relation in Josephson junctions,* Rev. Mod. Phys. **76**, 411 (2004).

[4] Y. Imry, *Introduction to Mesoscopic Physics* (Oxford University Press, Oxford, 1997).

[5] M. Büttiker, Y. Imry, and R. Landauer, *Josephson behavior in small normal one-dimensional rings,* Physics Letters A **96**, 365 .

[6] S.-K. Yip, *Magnetic-field effect on the supercurrent of an SNS junction,* Phys. Rev. B **62**, R6127 (2000).

[7] J. M. Rowell, *Magnetic Field Dependence of the Josephson Tunnel Current,* Phys. Rev. Lett. **11**, 200 (1963).

[8] H. B. Heersche, P. Jarillo-Herrero, J. B. Oostinga, L. M. K. Vandersypen, and A. F. Morpurgo, *Bipolar supercurrent in graphene,* Nature **446**, 56 (2007).

[9] T. Yokoyama, M. Eto, and Y. V. Nazarov, *Anomalous Josephson effect induced by spin-orbit interaction and Zeeman effect in semiconductor nanowires,* Phys. Rev. B **89**, 195407 (2014).

[10] K. Zuo, V. Mourik, D. B. Szombati, B. Nijholt, D. J. van Woerkom, A. Geresdi, J. Chen, V. P. Ostroukh, A. R. Akhmerov, S. R. Plissard, D. Car, E. P. A. M. Bakkers, D. I. Pikulin, L. P. Kouwenhoven, and S. M. Frolov, *Supercurrent Interference in Few-Mode Nanowire Josephson Junctions,* Phys. Rev. Lett. **119**, 187704 (2017).

[11] F. S. Bergeret, A. F. Volkov, and K. B. Efetov, *Odd triplet superconductivity and related phenomena in superconductor-ferromagnet structures,* Rev. Mod. Phys. **77**, 1321 (2005).

[12] M. Titov and C. W. J. Beenakker, *Josephson effect in ballistic graphene,* Phys. Rev. B **74**, 041401 (2006).

[13] A. G. Moghaddam and M. Zareyan, *Josephson effect in mesoscopic graphene strips with finite width,* Phys. Rev. B **74**, 241403 (2006).

[14] M. Gmitra, S. Konschuh, C. Ertler, C. Ambrosch-Draxl, and J. Fabian, *Band-structure topologies of graphene: Spin-orbit coupling effects from first principles,* Phys. Rev. B **80**, 235431 (2009).

[15] J. Sichau, M. Prada, T. Anlauf, T. J. Lyon, B. Bosnjak, L. Tiemann, and R. H. Blick, *Resonance Microwave Measurements of an Intrinsic Spin-Orbit Coupling Gap in Graphene: A Possible Indication of a Topological State,* Phys. Rev. Lett. **122**, 046403 (2019).

[16] Z. Wang, D.-K. Ki, H. Chen, H. Berger, A. H. MacDonald, and A. F. Morpurgo, *Strong interface-induced spin–orbit interaction in graphene on WS_2,* Nature Communications **6**, 8339 (2015).

[17] Z. Wang, D.-K. Ki, J. Y. Khoo, D. Mauro, H. Berger, L. S. Levitov, and A. F. Morpurgo, *Origin and Magnitude of 'Designer' Spin-Orbit Interaction in Graphene on Semiconducting Transition Metal Dichalcogenides,* Phys. Rev. X **6**, 041020 (2016).

[18] C. K. Safeer, J. Ingla-Aynés, F. Herling, J. H. Garcia, M. Vila, N. Ontoso, M. R. Calvo, S. Roche, L. E. Hueso, and F. Casanova, *Room-Temperature Spin Hall Effect in Graphene/MoS2 van der Waals Heterostructures,* Nano Lett. **19**, 1074 (2019).

[19] M. Irfan, S. R. Kuppuswamy, D. Varjas, P. M. Perez-Piskunow, R. Skolasinski, M. Wimmer, and A. R. Akhmerov, *Hybrid kernel polynomial method,* arXiv:1909.09649 [cond-mat] (2019).

[20] A. Weiße, G. Wellein, A. Alvermann, and H. Fehske, *The kernel polynomial method,* Rev. Mod. Phys. **78**, 275 (2006).

[21] C. W. Groth, M. Wimmer, A. R. Akhmerov, and X. Waintal, *Kwant: a software package for quantum transport,* New J. Phys. **16**, 063065 (2014).

[22] C. W. J. Beenakker, *Universal limit of critical-current fluctuations in mesoscopic Josephson junctions,* Phys. Rev. Lett. **67**, 3836 (1991).

[23] H. A. Kramers, Proc. Amsterdam Acad. **33**, 959 (1930).

[24] I. O. Kulik and A. N. Omel'yanchuk, *Contribution to the microscopic theory of the Josephson effect in superconducting bridges,* JETP Lett. **21**, 96 (1975).

[25] A. M. Clogston, *Upper Limit for the Critical Field in Hard Superconductors,* Phys. Rev. Lett. **9**, 266 (1962).

[26] C. Ishii, *Josephson Currents through Junctions with Normal Metal Barriers,* Prog Theor Phys **44**, 1525 (1970).

[27] J. Bardeen and J. L. Johnson, *Josephson Current Flow in Pure Superconducting-Normal-Superconducting Junctions,* Phys. Rev. B **5**, 72 (1972).

[28] P. G. de Gennes and D. Saint-James, *Elementary excitations in the vicinity of a normal metal-superconducting metal contact,* Physics Letters **4**, 151 (1963).

6

THE AC JOSEPHSON LASER

This chapter has been previously published as M. C. Cassidy, A. Bruno, S. Rubbert, M. Irfan, J. Kammhuber, R. N. Schouten, A. R. Akhmerov and L. P. Kouwenhoven, *Demonstration of an ac Josephson junction laser*, Science **355**, 939 (2017).
My contribution to this work is the modeling and simulation of the microwave resonator coupled with a dc voltage-biased Josephson junction jointly with S. Rubbert.

6.1. INTRODUCTION

Josephson junctions are natural voltage to frequency converters via the AC Josephson effect. For a Josephson junction without an applied DC voltage bias, Cooper pairs tunnel coherently from one superconducting condensate to the other, resulting in a supercurrent flowing without dissipation. However, for a nonzero DC voltage bias (V_b) less than the superconducting energy gap, transport is prohibited unless the excess energy ($hf = 2eV_b$, with Planck's constant h, frequency f, and the charge of the Cooper pair $2e$) can be dissipated into the environment. The analogy between a single Josephson junction and a two-level atom was first proposed theoretically in the 1970's [1]. The voltage difference across the junction provides the two energy levels for the Cooper pairs, and spontaneous emission as well as stimulated emission and absorption were predicted to occur [1, 2]. Emission from Josephson junctions into low-quality cavities (either constructed artificially or intrinsic to the junction's environment) in the so-called weak-coupling regime has been studied extensively [3–8]. However, because the total output power of these systems is low, coherent radiation has not been directly demonstrated. By using a tightly confined cavity mode coherent interaction of a single Josephson junction and the cavity can be achieved. Lasing results when the transfer rate of Cooper pairs across the junction, Γ_{CP}, exceeds the cavity decay rate, κ, of the microwave photons (Fig. 6.1(a)). Photon emission from alternative single emitters coupled to superconducting resonators has been the subject of several recent investigations [8–10].

We demonstrate lasing in the microwave frequency domain from a dc voltage-biased Josephson junction strongly coupled to a superconducting coplanar waveguide resonator. Our device obeys several properties present in conventional optical lasers, including injection locking, and frequency comb generation, with an injection locked linewidth of $\lesssim 1$Hz, which exceeds performance of other state of the art laser systems. The laser consists of a half-wave coplanar waveguide (CPW) resonator with resonant frequency $f_0 \approx 5.6$GHz made from thin (20nm) NbTiN (Fig. 6.1, (b) and (c)). A DC superconducting quantum interference device (SQUID), located at the electric field anti-node of the cavity, effectively acts as a single junction with Josephson energy tunable via the magnetic flux ϕ threading its loop: $E_J = E_{J0}|\cos(\pi\phi/\phi_0)|$, with $E_{J0} \sim 78$GHz, and $\phi_0 = h/2e$ the superconducting flux quantum. One side of the SQUID is tied to the central conductor of the CPW, with the other end attached directly to the ground plane to enhance the coupling to the cavity. An on-chip inductor positioned at the electric field node of the cavity allows for a stable DC voltage bias to be applied across the SQUID [11]. Coupling capacitors at each end of the cavity provide an input and output for microwave photons at a rate of κ_{in} and κ_{out}, respectively, as in standard circuit-QED experiments [12]. The device is mounted in a dilution refrigerator with base temperature $T = 15$mK, and the magnetic flux through the SQUID is tuned via a superconducting vector magnet.

6.2. DEVICE DESIGN

A 20nm NbTiN film was reactively sputtered on a cleaned 2" sapphire substrate. An SF_6/O_2 dry etch was then used to define the CPW resonator, coupling capacitors and spiral inductor. The junction sizes were $\sim 180\text{nm} \times 150\text{nm}$, and had a total normal state resistance of $R_D = 2.4\text{k}\Omega$, with an estimated junction capacitance $C_J = 2$fF per junction.

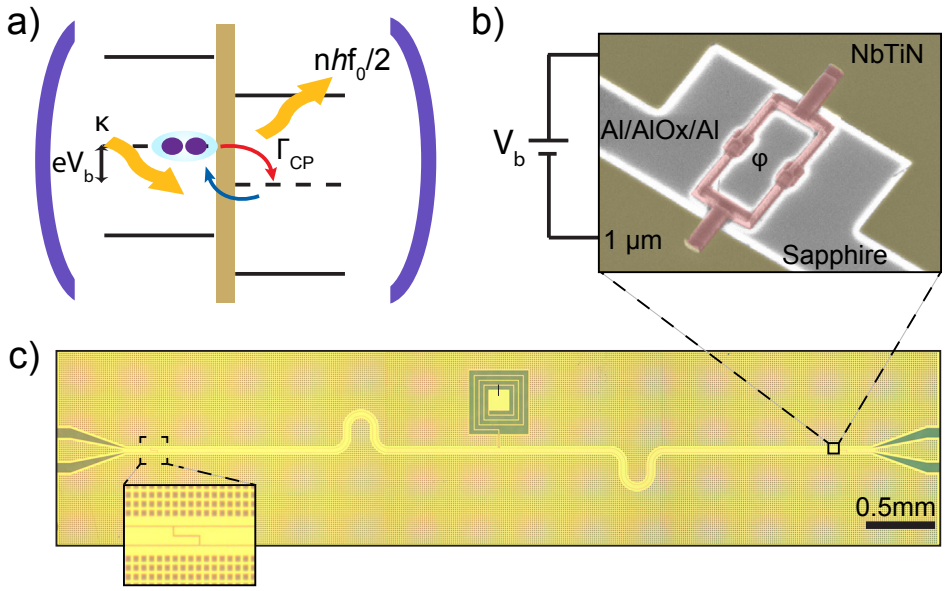

Figure 6.1: An ac Josephson laser. **(a)** Illustration of the operating principle of the device. A DC voltage bias V_b applied across the Josephson junction results in photon emission into the cavity when twice the bias voltage is equal to a multiple of the cavity frequency. If the emission rate Γ_{CP} into the cavity exceed the cavity lifetime κ, these photons can be reabsorbed and reemitted by the junction, a process akin to stimulated emission in atomic laser systems. Dashed lines depict the superconducting condensate; solid lines represent the superconducting gap, Δ. **(b)** Scanning electron microscope (false color) and **(c)** optical microscopy images of the device. A DC SQUID (red), acting as a tunable Josephson junction, is strongly coupled to the electric field antinode of a half-wave superconducting coplanar waveguide resonator (yellow).

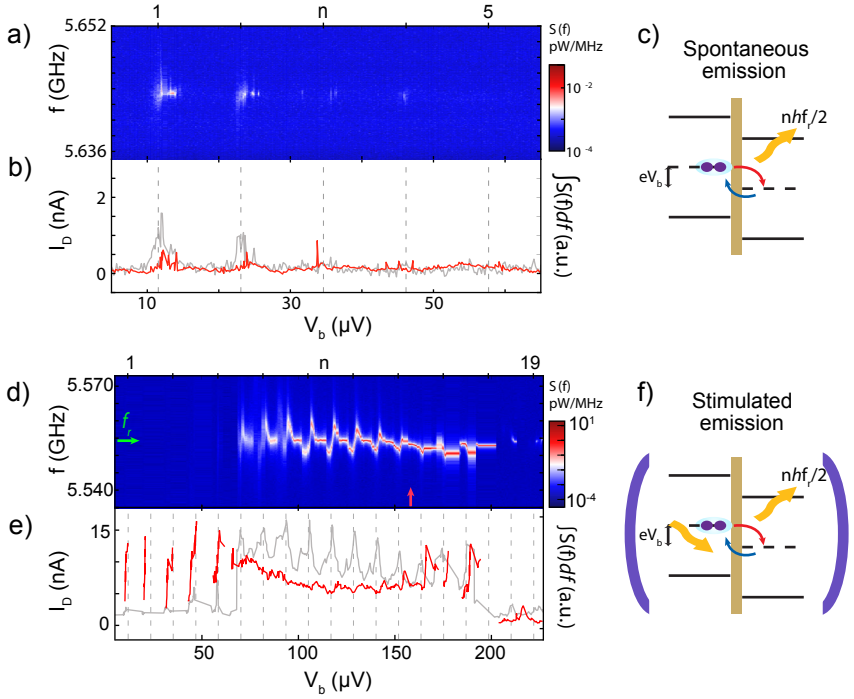

Figure 6.2: Microwave emission from the Josephson laser. **(a)** Power spectrum of the emitted radiation $S(f)$, **(b)** integrated emission (grey) and corresponding current flowing through the Josephson junction (red) as a function of V_b when the coupling strength $\lambda \ll 1$. **(c)** Cooper pair transport can occur at discrete voltage biases corresponding to multiples of the cavity resonance frequency f_0, resulting in spontaneous photon emission into the cavity. When $\lambda > 1$, the emission **(d)** and corresponding current flow **(e)** become continuous across a range of bias values, peaking at bias voltages corresponding to multiples of the cavity frequency. **(f)** Cooper pair transport is accompanied by the release of multiple photons into the cavity at the fundamental frequency, as well as emission of photons into the higher-order resonator modes, resulting in a cavity photon occupancy large enough for stimulated emission to occur.

The device is therefore in the strongly underdamped regime ($\beta_C = 2eI_cR_D^2C_J/\hbar \gg 1$).

The emission frequency of the laser is set by the resonant frequency of the bare cavity $\omega_0 = 2\pi f_0 = 1/\sqrt{LC}$, which is determined by its geometric design as well as the kinetic inductance of the thin NbTiN film ($L = L_g + L_k$). For our geometry, which consists of a 30μm wide central conductor of length $\lambda/2 = 5650\mu$m, with 1.5μm spacings to the ground plane, with $C \sim 1.4$pF and $L_g \sim 1.2$nH determined using elliptical integrals [13], while $L_k \sim 4.2$nH is determined experimentally for the film from characterization resonators. Based on this we calculate a kinetic inductance fraction $\alpha = 0.78$. The total impedance $Z(\omega)$ seen by the tunneling Cooper pairs consists of the combination of the impedance of the Josephson junction and that of the parallel LC resonance with finite Q factor. As the capacitance of the resonator is much greater than the junction ($C \gg C_J$), the impedance is dominated by that of the resonator. The capacitance of each of the coupling capacitors was simulated to be 11.1fF, which results in a calculated coupling quality factor of $Q_c \sim 10^4$, giving $\kappa_{in} = \kappa_{out} = 0.27$MHz. The intrinsic quality factor of the resonator without the SQUID was much higher. Bare resonators fabricated on the same film showed $Q_i > 10^5$. However, the presence of the SQUID provides an additional damping mechanism due to the finite resistance, reducing the loaded quality factor $Q_l^{-1} = Q_c^{-1} + Q_i^{-1} + Q_r^{-1} \sim 1200$, resulting in a total cavity decay rate $\kappa = 4.7$MHz.

6.3. MICROWAVE EMISSION AND LASING

We first examine the response of the device without applying any microwave power to the cavity input. At the output, we measure the power spectral density, $S(f)$, of the emitted microwave radiation as a function of voltage bias V_b. Simultaneously, we record the corresponding current flowing through the device, $I_D = 2e\Gamma_{CP}$. The coupling between a dc voltage-biased Josephson junction and a cavity $\lambda = E_J/\phi_0^2 L$ is set by the junction's Josephson energy, E_J, together with the cavity inductance, $L = 1/C\omega_0^2$, with the cavity capacitance C and $\omega_0 = 2\pi f_0$. When the device is configured in the weak Josephson coupling regime ($\lambda \ll 1$, Fig. 6.2(a)), by tuning the external flux close to $\phi = \phi_0$, a series of discrete microwave emission peaks are visible at bias voltages corresponding to n multiples of the bare cavity resonance V_r: $V_b = nV_r = nhf_0/2e \approx n \times 11.62\mu$V). At each of these emission bursts, we observe an increase in dc current (Fig. 6.2(b)), a measure of inelastic Cooper pair transport across the Josephson junction. In this weak coupling regime, both the current and microwave emission are dominated by linear effects, with the rate of photon emission determined by the environmental impedance [7, 14] (Fig. 6.2(c)).

We increase the microwave emission by increasing E_J via the applied flux, to the extent that the junction and cavity become strongly coupled and the system transitions to nonlinear behavior ($\lambda \gg 1$) [15]. In contrast to the discrete emission peaks seen at low Josephson energy, the emission now shifts to higher bias voltages, persisting continuously even when the voltage bias is detuned from resonance (Fig. 6.2(d)), and is accompanied by a constant flow of Cooper pairs tunneling across the junction (Fig. 6.2(e)). The emission peaks at voltages corresponding to multiples of the cavity resonance, exhibiting bifurcations common to nonlinear systems under strong driving. Between these points of instability, the emission linewidth narrows to $\sim$ 22kHz, well below the bare cavity linewidth of $\sim$ 5MHz, corresponding to a phase coherence time $\tau_c = 1/\pi\nabla f_0 = 15\mu$s.

The enhancement in emission originates from stimulated emission, as a larger photon number in the cavity increases the probability of reabsorption and coherent reemission by the junction. Notably, the emission power increases here by more than three orders of magnitude, while the average dc power input, $P_{\text{in}} = V_b I_D$, varies by only a factor of three. By comparing P_{in} with the integrated output power, we estimate a power conversion efficiency $P_{\text{out}}/P_{\text{in}} > 0.3$, several orders of magnitude greater than achieved for single junctions without coupling to a cavity [4] and comparable only to arrays containing several hundred synchronized junctions [5]. Similar power conversion efficiencies have been seen in other strongly coupled single emitter-cavity systems [8, 9]. Application of a larger perpendicular magnetic field adjusts the cavity frequency, directly tuning the laser emission frequency by more than 50MHz.

To directly confirm lasing, we measure the emission statistics in the high-Josephson coupling regime at $V_b = 192.5\mu$V. The emitted signal is mixed with an external local oscillator and the resulting quadrature components digitized with a fast acquisition card (Fig. 6.3(a)). A time series of the demodulated free-running laser emission over a period of 100μs (Fig. 6.3(b)) shows a clear sinusoidal behavior, never entering a sub-threshold state.

This is in contrast to recently demonstrated lasers made from quantum dots [10] or superconducting charge qubits [8, 9], which are strongly affected by charge noise. Instead, we note that the coherence of our system is disrupted by occasional phase slips (Fig. 6.3(b), inset). To quantify the effect of these phase slips, we plot the autocorrelation $g^{(1)}$ (Fig. 6.3(c)) and extract a phase coherence time of 14μs, in good agreement with the value extracted from the free running linewidth.

To confirm coherence over longer time scales, we plot the in-phase and quadrature components of the downconverted signal from 5×10^5 samples on a two-dimensional histogram (Fig. 6.3(d)). The donut shape of the histogram confirms lasing, with the radius $A = \sqrt{\bar{N}} = 172$ (with the average photon number $\bar{N}$) representing the average coherent amplitude of the system, whereas the finite width $\sigma_l = \sqrt{(2\delta A^2 + N_{noise})/2} = 6.89$ is a result of amplitude fluctuations in the cavity emission $\delta A = 2.66$ broadened by the thermal noise in the amplifier chain, N_{noise}. When the device is not lasing ($V_b = 18\mu$V in Fig. 6.2(a)), we record a Gaussian peak of width $\sigma_{th} = \sqrt{N_{noise}/2} = 6.36$, corresponding to thermal emission (Fig. 6.3(e)).

To extract the photon number distribution at the output of the cavity, the contribution of thermal fluctuations due to the amplifier chain in Fig. 6.3(e) is subtracted from the emission data in Fig. 6.3(d). The extracted distribution takes the form $p_n \propto \exp\left[-(n-\bar{N})^2/(2\bar{N}(1+4\delta A^2))\right]$ and is centered $\bar{N} \approx 2.96 \times 10^4$, (red curve in Fig. 6.3(f)). In contrast, a perfectly coherent source is expected to show a shot noise limited Poissonian distribution, which tends to a Gaussian distribution of the form $p_n \propto \exp\left[-(n-\bar{N})^2/2\bar{N}\right]$ in the limit of large $\bar{N}$ (blue curve in Fig. 6.3(f)). The residual fluctuations in the cavity amplitude are most probably due to E_J fluctuations which change the instantaneous photon emission rate into the cavity.

6.3.1. LINEWIDTH AND OUTPUT POWER MEASUREMENTS

Figure 6.4 shows the narrowing of the cavity transmission linewidth in the lasing regime as compared to the non-lasing regime in Fig. 6.2. We note more than two orders of

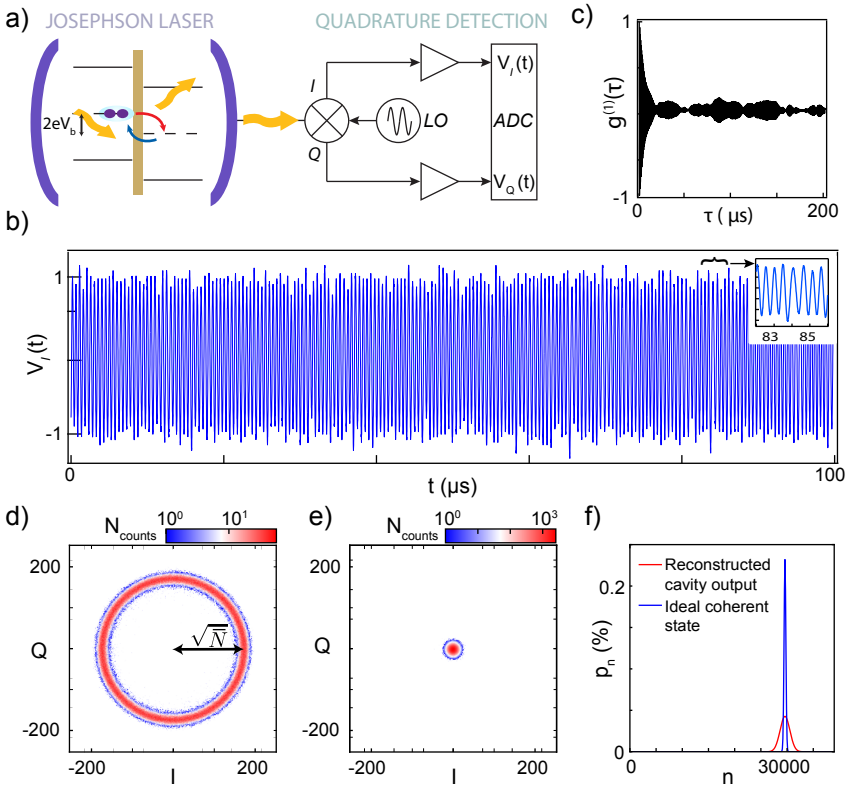

Figure 6.3: Coherence and emission statistics of the free running Josephson laser. **(a)** Real-time evaluation of the emission statistics of the free-running Josephson laser is performed with a heterodyne measurement setup. **(b)** Time series $V_I(t)$ of the emission over 100μs (Inset) Small phase slips in the emission result in loss of coherence, resulting in an artificially broadened emission line. **(c)** Autocorrelation $g^{(1)}(\tau)$ of the time series shows a phase coherence of $\sim 14\mu$s. **(d)** The IQ histogram acquired above the lasing threshold shows a clear donut shape, a characteristic of coherent emission. **(e)** The IQ histogram obtained when the device is not emitting shows a Gaussian peak centered at zero, corresponding to thermal emission. **(f)** The reconstructed photon number distribution p_n at the cavity output (red) is well fit by a single Gaussian peak centered around an average photon number $\bar{N} \approx 2.96 \times 10^4$, slightly broader than what expected for and ideal coherent source (blue).

magnitude narrowing without an injection locking signal.

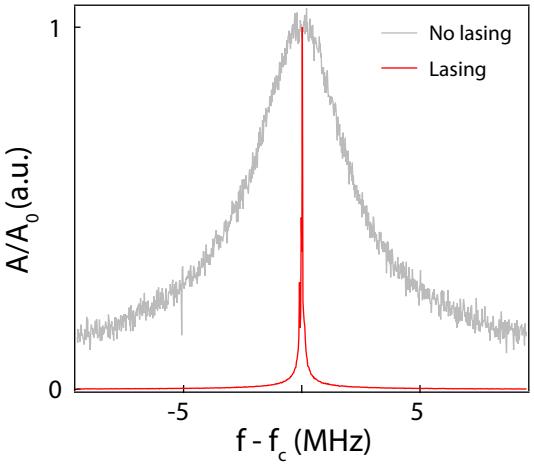

Figure 6.4: Linewidth narrowing under lasing. Normalized cavity transmission with the device lasing (red) and with the device off (grey). The device shows linewidth narrowing of more than two orders of magnitude when configured for lasing. The transmission when the laser was not lasing was measured at $V_b = 31\mu$V, between the second and third emission peaks in Fig. 6.2(a), while the trace when the laser was emitting was recorded at $V_b = 162\mu V$ in Fig. 6.2(d). For both measurements $P_{inj} = -140$dBm, below the single photon power in the cavity.

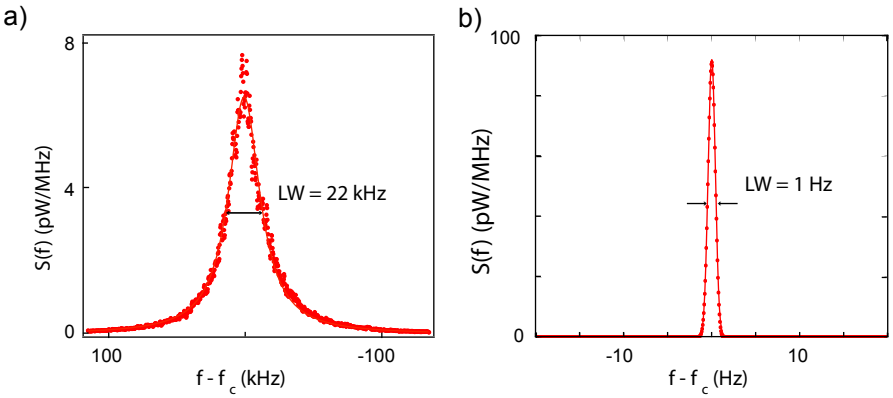

Figure 6.5: Emission linewidth of the Josephson laser. Power spectral density $S(f)$ of **(a)** the free running laser and **(b)** the injection locked laser, measured in the large Josephson coupling regime. In free running mode, the laser is well fit by a Lorentzian function from which we extract a full-width at half maximum linewidth $\sigma = 21.4$kHz. This corresponds to a laser coherence time $\tau_{coh} = 1/(\pi\sigma) = 15\mu$s and a coherence length $l_{coh} = \tau_{coh} c = 4.45$km. When injection locked, the injection locked linewidth of the laser is $\sim$ 1Hz, which is limited by the linewidth of the injected tone.

By integrating the emission data in Fig. 6.5(a), we estimate the output power $P_{out} =$

$\int S(f)df = 0.255$pW. The DC input power to the device is calculated as $P_{in} = I_D V_b = 0.81$pW, with $I_D = 5$nA and $V_b = 162\mu$V, which gives a power conversion efficiency $P_{out}/P_{in} > 0.3$.
The quantum limited laser linewidth is predicted by the Schawlow-Townes formula [16]:

$$\sigma_{ST} = hf_0 \frac{\gamma^2}{P_{out}}, \tag{6.1}$$

with, P_{out} the power at the cavity output and γ the linewidth of the atomic transition, and is valid in the limit where $\gamma \ll \kappa$, with κ the cavity linewidth. In the case where $\kappa \leq \gamma$, as is common for many semiconductor-based laser systems, this expression is modified by replacing γ with an effective linewidth $l_{ST}^{-1} = \gamma^{-1} + \kappa^{-1}$, which tends to $l_{ST} = \kappa$ for $\kappa \ll \gamma$ [17]. In our case, the atomic transition is the voltage bias on the Josephson junction V_b, and its linewidth is set by the residual voltage noise, which is of order 30 kHz, much less than κ. Using the output power calculated from by integrating the emission data in Fig. 6.5(a), we calculate the Schawlow-Townes linewidth to be ~ 14mHz.

6.3.2. FLUX TUNING OF THE JOSEPHSON COUPLING AND EMISSION FREQUENCY

We tune the Josephson coupling and emission frequency by tuning the flux through the SQUID, as demonstrated in Fig. 6.6(a)-(b). We show the power spectral density for increasing coupling strength between the SQUID and the cavity in Fig. 6.6(c)-(f) corresponding to arrows in Fig. 6.6(a).

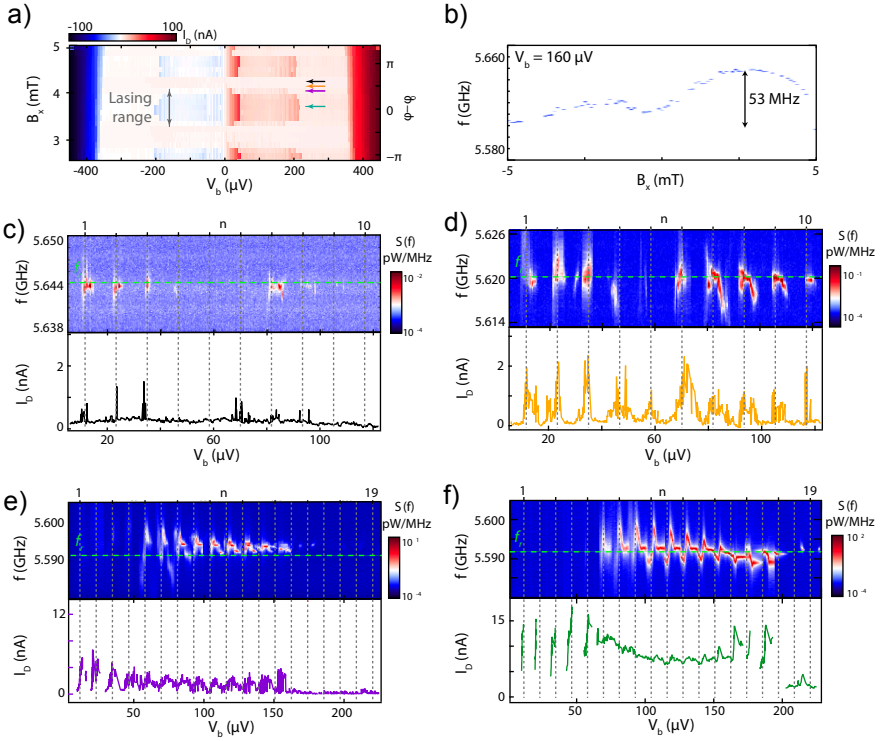

Figure 6.6: Flux tuning of the Josephson coupling and emission frequency. **(a)** The Josephson coupling strength is tuned by the application of a perpendicular magnetic field through the SQUID loop. The supercurrent and subgap emission features show a characteristic SQUID oscillation with periodicity ~ 1 mT, which is in good agreement for a SQUID of area ~ $1.5\mu m^2$. The arrows show the approximate values for the magnetic flux tuning for the data shown in (c) – (f). **(b)** Application of a larger perpendicular magnetic field shifts the resonant frequency of the cavity, tuning the laser emission over a frequency range of more than 50MHz. Shown is the power spectral density $S(f)$ as a function of perpendicular magnetic field B_x at fixed voltage bias $V_b = 160\mu V$. In (a) and (b), the applied external magnetic field has a small offset from the true magnetic field due to hysteresis in the superconducting magnet and residual magnetic fields in the setup. **(c) – (f)** Power spectral density $S(f)$ of the emission for increasing Josephson couplings corresponding to the location of arrows in (a). By tuning the applied magnetic flux, the device evolves from weak coupling between the SQUID and the cavity to being strongly coupling, where significant line narrowing takes place. The current spikes present at low bias voltages in (f) occur due to instabilities in the load circuit at low bias, and correspond to retrapping to the zero-voltage state, as is common for many measurements of voltage biased Josephson junctions. As these points are analogous to the case of a zero bias supercurrent flow, they are not accompanied by photon emission.

Our device operates in different regimes depending upon the value of applied voltage bias as compared to the superconducting gap. We illustrate this in Fig. 6.7.

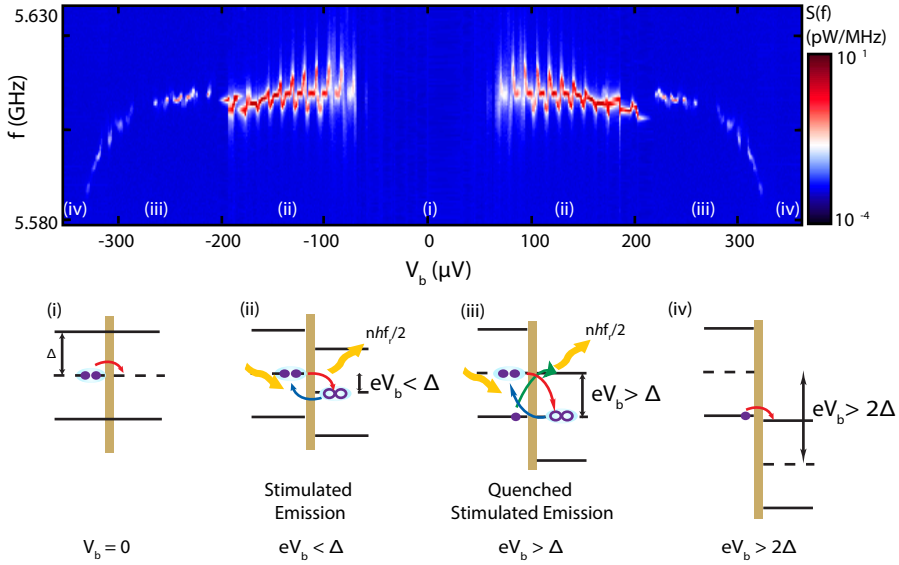

Figure 6.7: Operating regimes of the Josephson laser. Power spectral density $S(f)$ over a wider range of applied voltage bias at large Josephson coupling. (i) Dissipationless supercurrent. At $V_b = 0$, Cooper pairs can directly tunnel across the junction without additional energy being dissipated. (ii) Stimulated emission. At a large Josephson coupling and a voltage bias equal to a multiple of the cavity resonance, many photons are released into the cavity. The cavity photon population is large enough that the junction can reabsorb and re-emit some of these photons. (iii) Quenched stimulated emission. When the voltage bias exceeds the superconducting gap $eV_b > \Delta$, absorption of cavity photons can also allow quasiparticles to tunnel across the junction, damping the junction and quenching the emission (iv) Resistive transport. When the voltage bias exceeds twice the superconducting gap $eV_b > 2\Delta$, direct quasiparticle transport can take place without any accompanying photon emission.

6.3.3. TEMPERATURE DEPENDENCE OF LASING

The upper threshold bias voltage in the lasing regime depends on the temperature of the Sample (Fig. 6.8). For a temperature close to the critical temperature of the superconductor, the quasiparticle excitations bring the junction in the damped regime.

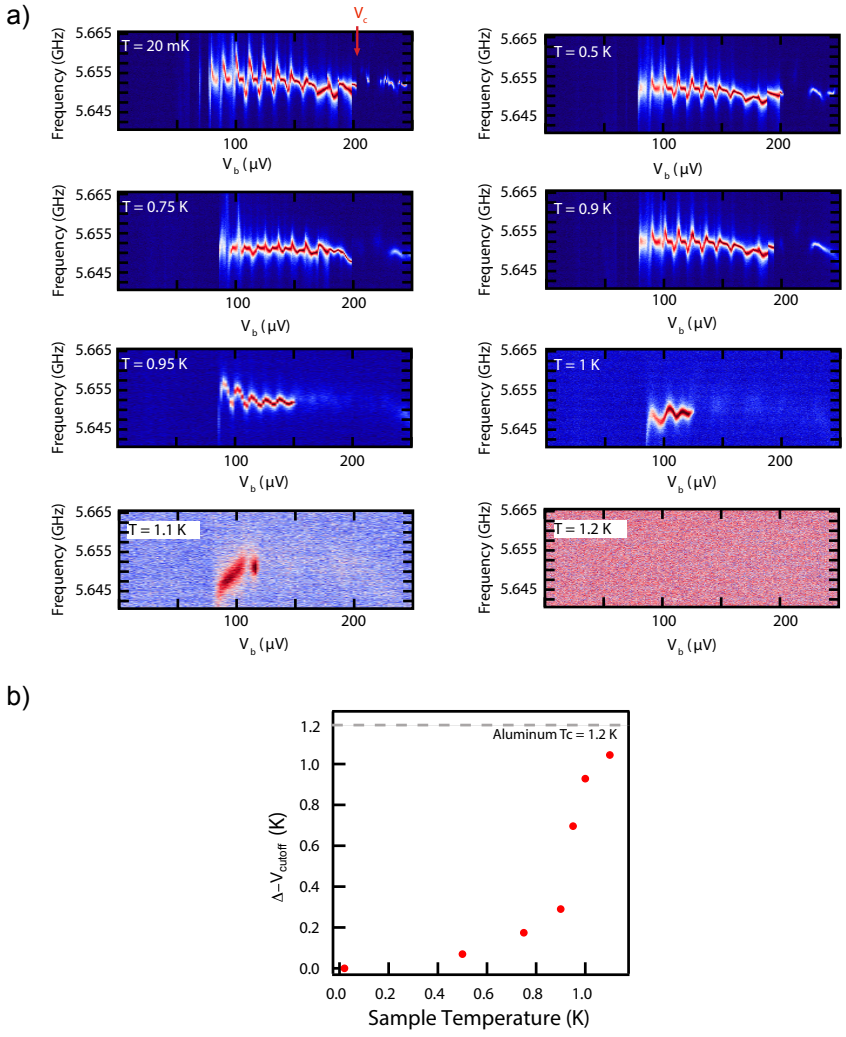

Figure 6.8: Temperature dependence of the emission. **(a)** Power spectral density $S(f)$ of the emission as a function of voltage bias for different sample temperatures. **(b)** The emission cutoff point V_c scales strongly with temperature close to the superconducting critical temperature of Aluminium, indicating that the upper cutoff of the emission V_c is set by excitation of quasiparticles that damp the junction.

6.4. INJECTION LOCKING

Emission linewidth is a key figure of merit for lasers. A narrow linewidth implies high frequency stability and resolution, which is important for a range of technologies including spectroscopy, imaging and sensing application. One technique commonly used for stabilizing lasers is injection locking [18, 19] (Fig. 6.9, (a) and (b)). The injection of a seed tone of frequency f_{inj} into the cavity generates stimulated emission in the Josephson junction at this injected frequency, narrowing the emission spectrum. Figure 6.9(c) shows *S(f)* as a function of input power P_{inj} for an injected signal with frequency $f_{\text{inj}} = 5.651$GHz, well within the emission bandwidth of the free running source [linecuts at $P_{\text{inj}} = -127$dBm and $P_{\text{inj}} = -90$dBm (Fig. 6.9(d))]. For very low input power, $P_{\text{inj}} < -140$dBm, the average photon occupation of the cavity is $\bar{N} < 1$, and the device remains unaffected by the input tone. Once the photon occupancy exceeds $\bar{N} \approx 1$, the injected microwave photons drive stimulated emission in the device, causing the emission linewidth to narrow with increasing power, reaching an ultimate (measurement-limited) linewidth of 1Hz (Fig. 6.9(d), inset), which is more than three orders of magnitude narrower than the free-running emission peak and approaches the Schawlow-Tones limit of $\sim$ 15 mHz. In this regime, our device acts as a quantum limited amplifier, similar to other Josephson junction based amplifiers [20, 21]; however, no additional microwave pump tone is required to provide amplification. Figure 6.9(e) shows the effect when the input tone is applied at a frequency $f_{\text{inj}} = 5.655$GHz, outside the cavity bandwidth. At low input powers the emission remains unaffected, similar to the on-resonant case shown earlier. When $P_{\text{inj}} > -130$dBm, distortion side-bands appear at both positive and negative frequencies, and the free running emission peak is pulled towards the input tone, eventually being locked when $P_{\text{inj}} > -85$dBm [linecuts at $P_{\text{inj}} = -127$dBm and $P_{\text{inj}} = -90$dBm (Fig. 6.9(f)]. The positions and intensities of these emission sidebands are well described by the Adler theory for the synchronization of coupled oscillators [22], similar to what has been observed for both traditional and exotic laser systems [18, 19].

The frequency range over which the device can be injection locked is strongly dependent on the injected power. Figure 6.9(g) shows the *S(f)* as a function of f_{inj} at an input power $P_{\text{inj}} = -90$dBm, with an injection locking range Δf of almost 5MHz. Here, the distortion sidebands span more than 100MHz. Measurements of Δf as a function of P_{inj} are shown in the inset of Fig. 6.9(g). Adler's theory predicts that the injection locking range should fit a square-root relation $\Delta f = \alpha\sqrt{P_{\text{inj}}}$, with a measured prefactor $\alpha = 3.66 \pm 1.93\text{MHz}/\sqrt{\text{W}}$.

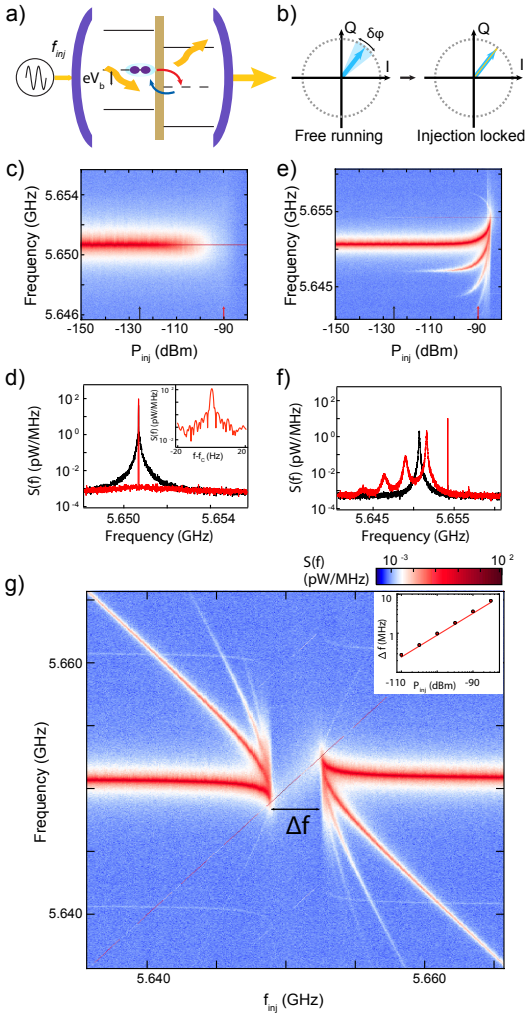

Figure 6.9: Injection locking of the Josephson laser. **(a)** Schematic illustration and (**b**), phasor diagram of the injection-locking process. Injection of a low-power input tone into the cavity drives stimulated emission of photons synchronous with the input tone, reducing the phase fluctuations $\delta\phi$ experienced in the free running mode. **(c)** *S(f)* as a function of input power (P_{inj}) for an on-resonance input tone. **(d)** Linecuts of (c) at $P_{\text{inj}} = -90$dBm (red) and -127dBm (black). (Inset) The linewidth of the injection-locked laser is $\lesssim 1$Hz **(e)** *S(f)* as a function of P_{inj} for an off-resonance input tone, demonstrating frequency pulling. **(f)** Linecuts of (e) at $P_{\text{inj}} = -90$dBm (red) and -127dBm (black). **(g)** *S(f)* at fixed input power $P_{\text{inj}} = -90$dBm as the frequency of the input tone f_{inj} is swept.For probe frequencies f_{inj} in the range Δf, the laser emission frequency locks to the frequency of the input signal. (Inset) The bandwidth of frequency locking Δf scales proportionally with the square root of the input power, in agreement with the Adler theory of coupled oscillators.

6.4.1. COMPARISON TO THEORY

We compare our injection locking data in Fig. 6.9 to the predictions of the Adler theory for coupled oscillators [22]. Following from [19, 23], for a given input power P_{inj}, the

frequency range Δf over which the input signal can be locked is given by

$$\Delta f = C_\kappa \kappa_t \sqrt{P_{inj}/P_{out}} = \alpha \sqrt{P_{inj}}. \tag{6.2}$$

Here the prefactor $C_\kappa = 2\sqrt{\kappa_{in}\kappa_{out}}/\kappa = 0.11$ accounts for internal cavity losses. This gives $\alpha = 1.07\text{MHz}/\sqrt{\text{W}}$, which is in reasonable agreement with the experimentally determined value of $\alpha = (3.66 \pm 1.93)\text{MHz}/\sqrt{\text{W}}$, as extracted from the fit to the data in Fig. 6.9. Outside the region of injection locking, the injection of an off-resonant tone at frequency f_{inj} results in generation of higher harmonics to the bare emission at frequency $f_0 = 5.65067\text{GHz}$. As the frequency of the injected signal approaches that of the bare emission, both the emitted signal and higher harmonics are pulled towards the injected tone until they are locked across the frequency range Δf. The positions of the pulled emission signal and the nth harmonics are given by

$$f_n = f_{inj} + (n+1) f_h, \tag{6.3}$$

with

$$f_h = (f_0 - f_{inj}) \sqrt{1 - \left(\frac{\Delta f/2}{f_0 - f_{inj}} \right)}. \tag{6.4}$$

Figure 6.10(a) shows the calculated positions of the pulled emission signal f_e (n = 0) and higher harmonics located at n=-2,1,2,3,4 overlaying the raw data for an input power P = −90dBm, which results in an injection locking frequency range of $\Delta f \approx 5\text{MHz}$. As seen from Eq. 6.3, the harmonic at $n = -1$ overlaps with the injected input tone, and so is not observed.

Adler's equation also predicts the relative powers of the sidebands when compared to the free emission power:

$$P_n/P_0 = |a_n/a_0|^2 = \left(\frac{(-f_0 + f_{inj} + f_h) + i\Delta f/2}{(f_0 - f_{inj} + f_h) - i\Delta f/2} \right)^{2n}. \tag{6.5}$$

Linecuts of the injection locking data in Fig. 6.10(a) are shown in Fig. 6.10(b)-(d). Fits to the experimental data are shown as black solid lines. Each emission peak is fit with a Lorentzian lineshape, with the input frequency fit with a Gaussian of width $\sigma = 10\text{kHz}$. Table 6.1 shows a comparison of the experimental and calculated harmonic frequencies f_n for each of the sidebands and the pulled emission, together with their relative emission power P_n/P_0 from solving Eq. 6.5. Frequencies are extracted by fitting the raw data with a multi-peaked Lorentzian function.

f_{in} (GHz)	5.6447		5.6481		5.6619	
	Calc.	Exp.	Calc.	Exp.	Calc.	Exp
f_e (GHz)	5.650	5.650	5.650	5.650	5.651	5.651
f_1 (GHz)	5.656	5.656	5.651	5.652	5.640	5.640
f_2 (GHz)	5.662	5.662	5.653	5.654	5.629	-
f_3 (GHz)	5.667	-	5.654	5.656	5.618	-
f_4 (GHz)	5.673	-	5.656	5.658	5.607	-
f_{-2} (GHz)	5.639	-	5.647	5.646	5.673	-
P_1/P_0	2.9×10^{-2}	1.1×10^{-2}	2.2×10^{-1}	1.2×10^{-1}	8.1×10^{-3}	3.5×10^{-3}
P_2/P_0	8.8×10^{-4}	3.2×10^{-4}	4.8×10^{-2}	1.0×10^{-2}	6.5×10^{-5}	-
P_3/P_0	2.6×10^{-5}	-	1.0×10^{-2}	1.6×10^{-3}	5.2×10^{-7}	-
P_4/P_0	7.7×10^{-7}	-	2.3×10^{-3}	9.3×10^{-4}	4.2×10^{-9}	-
P_{-2}/P_0	7.7×10^{-7}	-	2.3×10^{-3}	9.3×10^{-4}	4.2×10^{-9}	-

Table 6.1: Calculated and experimentally determined peak positions and relative intensities of sideband harmonics under injection locking.

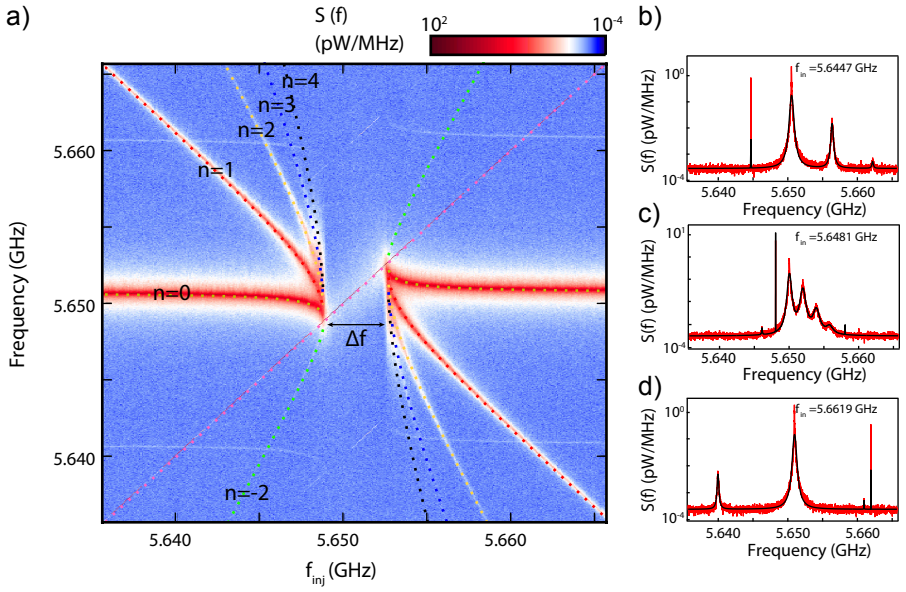

Figure 6.10: Injection locking - Comparison to theory. **(a)** Power spectral density *S(f)* as a function of frequency of the injected tone for an input power $P_{inj} = -90$dBm. The emission is injection locked for a frequency range $\Delta f \approx 5$MHz. Overlaying the data are the calculated positions of the pulled emission f_e and sidebands $f_{-2,1,2,3,4}$. Faint modulation sidebands can be seen at $f_e \pm 10$MHz due to noise on the input line to the cavity. **(b) – (d)** Linecuts of (a) corresponding to **(b)** $f_{inj} = 5.6447$GHz, **(c)** $f_{inj} = 5.6481$GHz and **(d)** $f_{inj} = 5.6619$GHz. The solid lines are fits to S(f).

6.4.2. FREQUENCY COMB GENERATION

Optical frequency combs have generated significant interest in recent years [24], making it possible to extend the accuracy of the atomic clocks from the radio to the optical frequency region, leading to breakthroughs in optical metrology, high precision spectroscopy and telecommunication technologies. Recently, microwave frequency combs have also been generated using four-wave mixing in superconducting resonators [25]. Here we demonstrate a similar frequency comb by applying a voltage modulation to the Josephson junction (Fig. 6.11(a)), as recently described theoretically in [26]. As an example, we configure the device in the on-resonance injection locked regime ($P_{inj} = -110$dBm in Fig. 6.9(c) and apply a small ac excitation of frequency $f_{\mathrm{mod}} = 111$Hz to the DC bias. This generates a comb around the central pump tone with frequency separation 111Hz, as seen in Fig. 6.11(b). The total width of the comb is set by the amplitude of the modulation (Inset, 6.11b), as well as the input power of the injection lock signal.

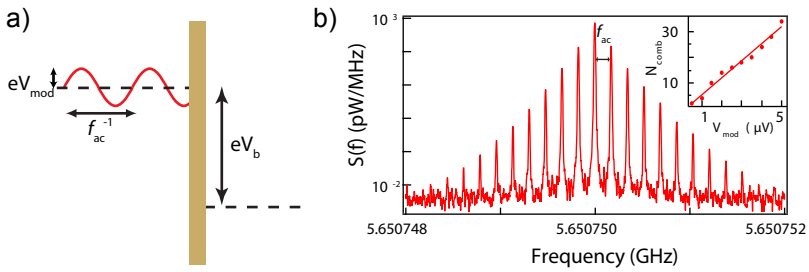

Figure 6.11: Frequency comb generation. **(a) – (b)** Low frequency ($f_{\mathrm{ac}} = 111$Hz) modulation of the voltage bias across the SQUID under injection locking conditions generates a frequency comb of phase coherent signals spaced f_{ac} in frequency around the center emission frequency. (Inset) The comb width, N_{comb}, is controlled by V_{mod}, the amplitude of the modulation on the voltage bias.

6.5. NUMERICAL MODEL

To understand the strong emission characteristics, we numerically simulate the time evolution of the coupled resonator-Josephson junction circuit for increasing E_J. We model the circuit as an LC resonator in series with a dc-SQUID with an applied voltage bias shown in Fig. 6.12. We begin our analysis with the single mode resonator approximation as studied in Ref.'s [15, 27, 28], with the equations of motion

$$C\ddot{\varphi} = L^{-1}\varphi - \gamma\dot{\varphi} + \phi_0^{-2} E_J \sin\left(2\pi f_J t + \varphi\right), \tag{6.6}$$

with f_J the Josephson frequency, φ the resonator phase variable, C and L the capacitance and inductance of the main resonator harmonic [$f_0 = 1/(2\pi\sqrt{LC})$], and γ the dissipation rate. The drive term is proportional to E_J and it is characterized by a dimensionless coupling strength $\lambda = E_J/\phi_0^2 C\omega_0^2$. Solving the time evolution numerically, we find that a strongly detuned drive $V_b/V_r = n \gg 1$ cannot produce a response that is only weakly dependent on f even for $\lambda \gtrsim 1$, contrary to the experimental observations (see left panels in Fig. 6.13).

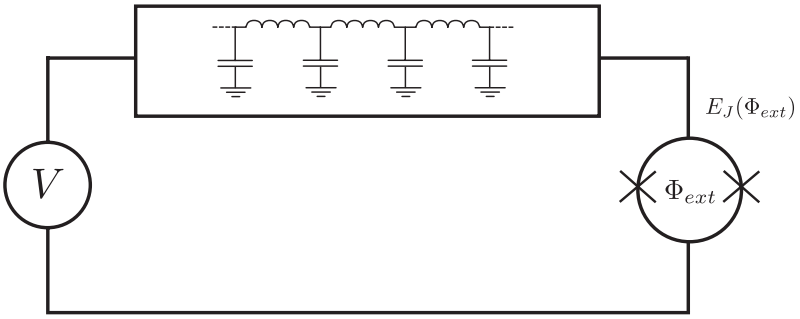

Figure 6.12: Circuit schematic. Circuit diagram of a voltage-biased Josephson junction in series with a resonator. The Josephson energy of the junction $E_J(\Phi_{ext})$ can be tuned by an external magnetic flux Φ_{ext}.

Going beyond the approximation of Ref. [15] we find that a necessary extension of the model allowing for efficient down-conversion from large n is the effect of the higher resonator modes leading us to:

$$C\ddot{\varphi}_i = i^2 L^{-1}\varphi_i - \gamma\dot{\varphi}_i + \phi_0^{-2} E_J \alpha_i \sin\left(2\pi f_J t + \sum_{i=1}^{M} \alpha_i \varphi_i\right), \tag{6.7}$$

with φ_i the phase variables of M resonator harmonics. Due to the strong nonlinearity of the equations of motion at small γ and large E_J, including the higher harmonics modes is a necessary extension of Eq. (6.6). We also verify that including Kerr nonlinearity or including the load circuit in the single mode dynamics (6.6) are not alone sufficient to reproduce the lasing behavior. The variation of the coupling strengths α_i of different modes to the Josephson junction is geometry-dependent, however we verify that the specific ratios of α_i do not influence our conclusions. For simplicity we present the results for $\alpha_i = 1$. A precise simulation of the coupling to the transmission line is beyond the scope of Eq. 6.7. In order to estimate the emitted power we therefore assume that all of the dissipation happens due to emission into the transmission line. This is supported by comparing the intrinsic resonator quality factor $Q \approx 10^5$ with the quality factor of the resonator coupled to the transmission line $Q \approx 2 \cdot 10^4$. This allows us to estimate the emitted power spectrum using $S(f) = \gamma f^2 \varphi_f^2$, with φ_f the Fourier component of φ at frequency f. Our numerical results are summarized in Fig. 6.13. The mode mixing results in approximate equipartition of emission power between the different resonator modes, and the number of available resonator modes determines the higher cutoff for the efficient down-conversion of f_J into the main harmonic of the resonator. A low E_J produces a series of disconnected peaks, as shown in the top panels of Fig. 6.13.

Studying the response of the lowest resonator harmonic more closely (see Fig. 6.14), we observe several features similar to the experimental observations. Specifically, the linewidth exhibits periodic modulation, becoming broader on resonance. The emission amplitude is continuous until a certain upper threshold, above which it separates into disconnected intervals.

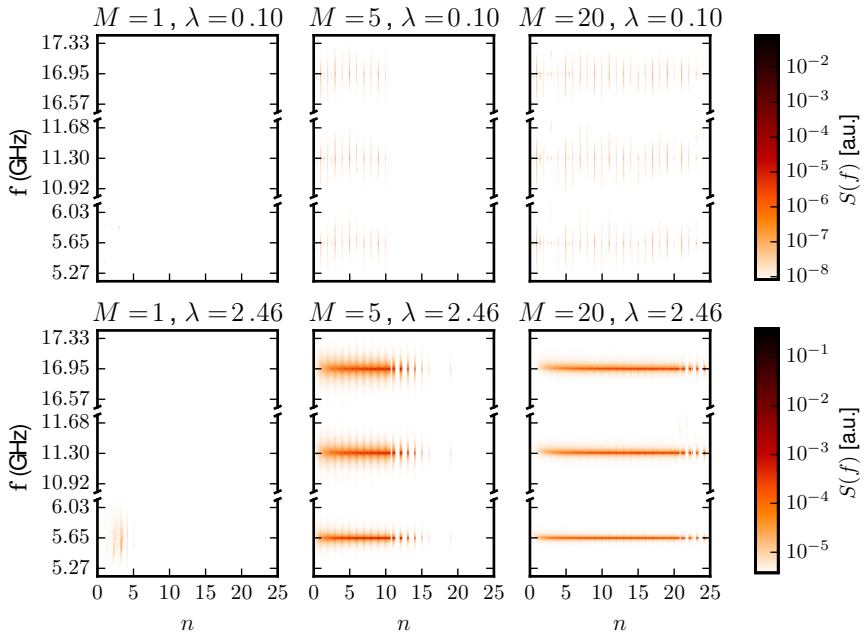

Figure 6.13: Dependence of the numerical emission spectra for different coupling strength and numbers of modes of the lowest three resonator modes.

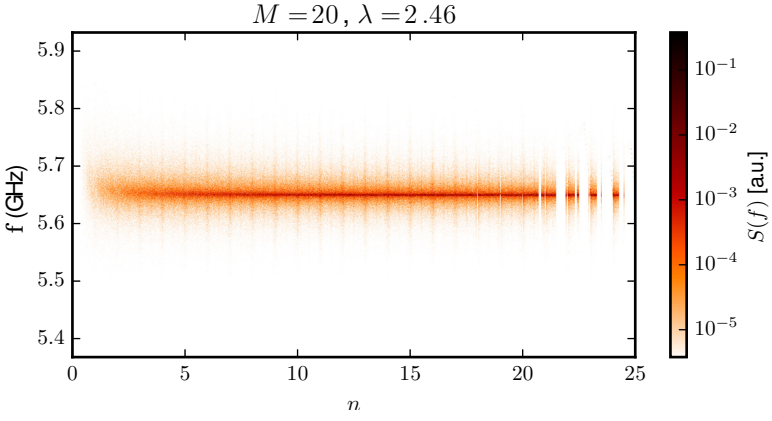

Figure 6.14: The emission spectrum of the lowest resonator mode for large coupling and in presence of multiple resonator modes.

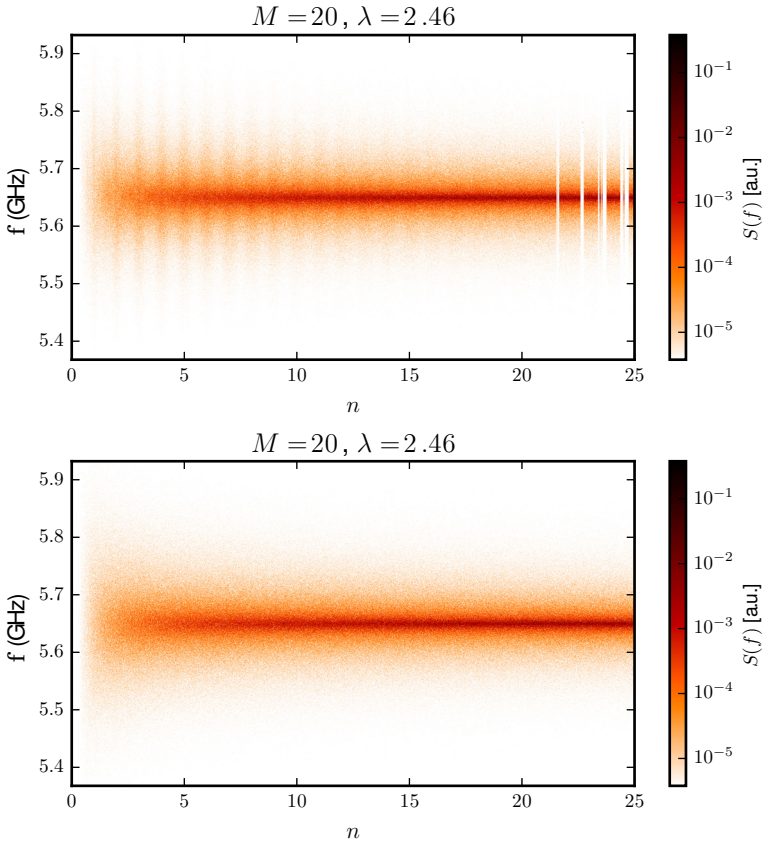

Figure 6.15: Emission spectrum of the lowest mode with **(a)** 10% detuning, or **(b)** 30% detuning

Finally, we relax the assumption of equal mode spacing, unexpected in a realistic line resonator. To study the effect of incommensurate mode frequencies, we consider the detuning of mode frequencies by a small random amount: $\omega_i = (i + r_i)\omega_0$ for $i > 1$. We choose detuning r_i to be a uniformly distributed random variable in the interval $[-0.1, 0.1]$ or $[-0.3, 0.3]$. Our results are shown in Fig. 6.15. We observe that the detuning of the higher harmonics does not change the overall spectral shape of the emitted signal, except for washing out the resonant peaks corresponding to the frequencies of the higher modes.

6.6. DISCUSSION

Our results conclusively demonstrate lasing from a dc-biased Josephson junction in the strong coupling regime. Analysis of the output emission statistics shows 15μs of phase coherence, with no sub-threshold behavior. The Josephson junction laser does not suffer from charge-noise-induced linewidth broadening inherent to semiconductor gain media, and thus reaches an injection locked linewidth of < 1Hz. The device produces frequency

tunability over 50MHz via direct tuning of the cavity frequency and over 100MHz through the generation of injection-locking sidebands. Additional frequency control may be achieved by using a broadband tunable resonator [29], and pulse control may be provided with a tunable coupler. The phase coherence is likely limited by fluctuations in E_J, either due to $1/f$-dependent flux noise from magnetic impurities [30], or due to defects within the Josephson junction, as well as thermal fluctuations in the biasing circuit that vary V_b. We anticipate that improvements to the magnetic shielding and passivating magnetic fluctuators, together with using a cryogenically generated voltage bias will further stabilize the emission. In this case the device would perform at the quantum limit, with a linewidth that would then only be limited by residual fluctuations in the photon number in the cavity. Along with the high efficiency, the possibility of engineering the electromagnetic environment and guiding the emitted microwaves on demand lends this system to a versatile cryogenic source for propagating microwave radiation.

REFERENCES

[1] D. R. Tilley, *Superradiance in arrays of superconducting weak links,* Physics Letters A **33**, 205 (1970).

[2] D. Rogovin and M. Scully, *Superconductivity and macroscopic quantum phenomena,* Physics Reports **25**, 175 (1976).

[3] N. F. Pedersen, O. H. Soerensen, J. Mygind, P. E. Lindelof, M. T. Levinsen, and T. D. Clark, *Direct detection of the Josephson radiation emitted from superconducting thinfilm microbridges,* Appl. Phys. Lett. **28**, 562 (1976).

[4] C. Varmazis, J. E. Lukens, and T. F. Finnegan, *Broadband generation of tunable Josephson radiation at microwave frequencies,* Appl. Phys. Lett. **30**, 660 (1977).

[5] P. Barbara, A. B. Cawthorne, S. V. Shitov, and C. J. Lobb, *Stimulated emission and amplification in Josephson junction arrays,* Phys. Rev. Lett. **82**, 1963 (1999).

[6] L. Ozyuzer, A. E. Koshelev, C. Kurter, N. Gopalsami, Q. Li, M. Tachiki, K. Kadowaki, T. Yamamoto, H. Minami, H. Yamaguchi, T. Tachiki, K. E. Gray, W.-K. Kwok, and U. Welp, *Emission of coherent THz radiation from superconductors,* Science **318**, 1291 (2007).

[7] M. Hofheinz, F. Portier, Q. Baudouin, P. Joyez, D. Vion, P. Bertet, P. Roche, and D. Esteve, *Bright side of the Coulomb blockade,* Phys. Rev. Lett. **106**, 217005 (2011).

[8] F. Chen, J. Li, A. D. Armour, E. Brahimi, J. Stettenheim, A. J. Sirois, R. W. Simmonds, M. P. Blencowe, and A. J. Rimberg, *Realization of a single-Cooper-pair Josephson laser,* Phys. Rev. B **90**, 20506 (2014).

[9] O. Astafiev, K. Inomata, A. O. Niskanen, T. Yamamoto, Y. A. Pashkin, Y. Nakamura, and J. S. Tsai, *Single artificial-atom lasing,* Nature **449**, 588 (2007).

[10] Y.-Y. Liu, J. Stehlik, C. Eichler, M. J. Gullans, J. M. Taylor, and J. R. Petta, *Semiconductor double quantum dot micromaser,* Science **347**, 285 (2015).

[11] F. Chen, A. J. Sirois, R. W. Simmonds, and A. J. Rimberg, *Introduction of a dc bias into a high-q superconducting microwave cavity,* Appl. Phys. Lett. **98**, 132509 (2011).

[12] A. Wallraff, D. I. Schuster, A. Blais, L. Frunzio, R.-S. Huang, J. Majer, S. Kumar, S. M. Girvin, and R. J. Schoelkopf, *Strong coupling of a single photon to a superconducting qubit using circuit quantum electrodynamics,* Nature **431**, 162 (2004).

[13] R. N. Simons, *Coplanar waveguide circuits, components, and systems*, Wiley Series in Microwave and Optical Engineering (Wiley, 2004).

[14] M. H. Devoret, D. Esteve, H. Grabert, G.-L. Ingold, H. Pothier, and C. Urbina, *Effect of the electromagnetic environment on the Coulomb blockade in ultrasmall tunnel junctions,* Phys. Rev. Lett. **64**, 1824 (1990).

[15] S. Meister, M. Mecklenburg, V. Gramich, J. T. Stockburger, J. Ankerhold, and B. Kubala, *Resonators coupled to voltage-biased Josephson junctions: From linear response to strongly driven nonlinear oscillations,* Phys. Rev. B **92**, 174532 (2015).

[16] A. L. Schawlow and C. H. Townes, *Infrared and optical masers,* Physical Review **112**, 1940 (1958).

[17] H. Wiseman, *Light amplification without stimulated emission: Beyond the standard quantum limit to the laser linewidth,* Phys. Rev. A **60**, 4083 (1999).

[18] H. L. Stover and W. H. Steier, *Locking of laser oscillators by light injection,* Appl. Phys. Lett. **8**, 91 (1966).

[19] Y.-Y. Liu, J. Stehlik, M. J. Gullans, J. M. Taylor, and J. R. Petta, *Injection locking of a semiconductor double-quantum-dot micromaser,* Phys. Rev. A **92**, 053802 (2015).

[20] B. Yurke, P. G. Kaminsky, R. E. Miller, E. A. Whittaker, A. D. Smith, A. H. Silver, and R. W. Simon, *Observation of 4.2-K equilibrium-noise squeezing via a Josephson-parametric amplifier,* Phys. Rev. Lett. **60**, 764 (1988).

[21] I. Siddiqi, R. Vijay, F. Pierre, C. M. Wilson, M. Metcalfe, C. Rigetti, L. Frunzio, and M. H. Devoret, *RF-driven Josephson bifurcation amplifier for quantum measurement,* Phys. Rev. Lett. **93**, 207002 (2004).

[22] R. Adler, *A Study of locking phenomena in oscillators,* Proceedings of the IRE **34**, 351 (1946).

[23] M. Armand, *On the output spectrum of unlocked driven oscillators,* Proceedings of the IEEE **57**, 798 (1969).

[24] S. T. Cundiff and J. Ye, *Colloquium: Femtosecond optical frequency combs,* Rev. Mod. Phys. **75**, 325 (2003).

[25] R. P. Erickson, M. R. Vissers, M. Sandberg, S. R. Jefferts, and D. P. Pappas, *Frequency comb generation in superconducting resonators,* Phys. Rev. Lett. **113**, 187002 (2014).

[26] P. Solinas, S. Gasparinetti, D. Golubev, and F. Giazotto, *A Josephson radiation comb generator,* Scientific Reports **1**, 12260 (2015).

[27] V. Gramich, B. Kubala, S. Rohrer, and J. Ankerhold, *From Coulomb-blockade to nonlinear quantum dynamics in a superconducting circuit with a resonator,* Phys. Rev. Lett. **111**, 247002 (2013).

[28] A. D. Armour, M. P. Blencowe, E. Brahimi, and A. J. Rimberg, *Universal quantum fluctuations of a cavity mode driven by a Josephson junction,* Phys. Rev. Lett. **111**, 1 (2013).

[29] Z. L. Wang, Y. P. Zhong, L. J. He, H. Wang, J. M. Martinis, A. N. Cleland, and Q. W. Xie, *Quantum state characterization of a fast tunable superconducting resonator,* Appl. Phys. Lett. **102**, 163503 (2013).

[30] F. C. Wellstood, C. Urbina, and J. Clarke, *Low frequency noise in dc superconducting quantum interference devices below 1 K,* Appl. Phys. Lett. **50**, 772 (1987).

CURRICULUM VITÆ

Muhammad IRFAN

12-02-1984 Born in Rawalpindi, Pakistan.

EDUCATION

2002–2005 B.Sc. in Physics, Chemistry, Mathematics
University of the Punjab, Lahore, Pakistan

2005–2007 M.Sc. in Physics
Quaid-e-Azam University, Islamabad, Pakistan

2007–2009 M.Phil. in Physics
Pakistan Institute of Engineering and Applied Sciences,
Islamabad, Pakistan

Thesis: Quantum Teleportation
Promotor: Prof. dr. Shahid. Qamar
Copromotor: Prof. dr. Sajid. Qamar

2015–2020 PhD. in Physics
Delft University of Technology, Delft, Netherlands

Thesis: Manipulation of supercurrent by the magnetic field
Promotor: Dr. Anton R. Akhmerov
Copromotor: Dr. Michael T. Wimmer

List of Publications

1. **Muhammad Irfan** and Anton R. Akhmerov, *Critical current plateau of graphene Josephson junctions in an in-plane magnetic field*, manuscript in preparation.

2. **M. Irfan**, S. R. Kuppuswamy, D. Varjas, P. M. Perez-Piskunow, M. Wimmer, and A. R. Akhmerov, *Hybrid kernel polynomial method*, arXiv:1909.09649 (2019).

3. **Muhammad Irfan** and Anton R. Akhmerov, *Geometric focusing of supercurrent in hourglass-shaped ballistic Josephson junctions*, arXiv:1810.04588 (2018).

4. R. Kraft, J. Mohrmann, R. Du, P. B. Selvasundaram, **M. Irfan**, U. N. Kanilmaz, F. Wu, D. Beckmann, H. von Löhneysen, R. Krupke, A. Akhmerov, I. Gornyi,and R. Danneau, *Tailoring supercurrent confinement in graphene bilayer weak links*, Nature Communications **9**, 1722 (2018).

5. F. Badshah, G-Q Ge, **M. Irfan**, S. Qamar, and S. Qamar, *On the tunneling time of ultracold atoms through a system of two mazer cavities*, Scientific Reports **8**, 1864 (2018).

6. M. C. Cassidy, A. Bruno, S. Rubbert, **M. Irfan**, J. Kammhuber, R. N. Schouten, A. R. Akhmerov, and L. P. Kouwenhoven, *Demonstration of an ac Josephson junction laser*, Science **355**, 939 (2017).

7. Fazal Badshah, **Muhammad Irfan**, Sajid Qamar, and Shahid Qamar, *Effects of mode profile on tunneling and traversal of ultracold atoms through vacuum-induced potentials*, Optics Communication **365**, 157 (2016).

8. Muhammad Waseem, **Muhammad Irfan**, and Shahid Qamar, *Realization of quantum gates with multiple control qubits or multiple target qubits in a cavity*, Quantum Information Processing **14**, 1869 (2015).

9. Fazal Badshah, **Muhammad Irfan**, Sajid Qamar, and Shahid Qamar, *Coherent control of tunneling and traversal of ultra-cold atoms through vacuum induced potentials*, Phys. Rev. A **88**, 044101 (2013).

10. Muhammad Waseem, Rizwan Ahmed, **Muhammad Irfan**, and Shahid Qamar, *Three-qubit Grovers algorithm using superconducting quantum interference devices in cavity-QED*, Quantum Information Processing **12**, 3649 (2013).

11. Fazal Badshah, **Muhammad Irfan**, Sajid Qamar, and Shahid Qamar, *Effects of detuning on tunneling and traversal of ultra-cold atoms through vacuum induced potentials*, Phys. Rev. A **87**, 012132 (2013).

12. Muhammad Waseem, **Muhammad Irfan**, and Shahid Qamar, *Multiqubit quantum phase gate using four-level superconducting quantum interference devices coupled to superconducting resonator*, Physica C **477**, 24 (2012).

13. Fazal Badshah, **Muhammad Irfan**, Sajid Qamar, and Shahid Qamar, *Tunneling and traversal of ultra-cold three-level atoms through vacuum-induced potentials*, Phys. Rev. A **84**, 032107 (2011).

14. **Muhammad Irfan**, Sajid Qamar, and Shahid Qamar, *Scheme for the teleportation of bipartite entangled state of the two cavity modes*, Optics Communication **284**, 675 (2011).